Downloaded from orbit.dtu.dk on: Dec 18, 2017

Technical University of Denmark

Hybrid Simulation of Composite Structures

Høgh, Jacob Herold; Berggreen, Christian; Branner, Kim; Schmidt, Jacob Wittrup; Stang, Henrik

Publication date:
2017

Document Version
Publisher's PDF, also known as Version of record

Link back to DTU Orbit

Citation (APA):
Høgh, J. H., Berggreen, C., Branner, K., Schmidt, J. W., & Stang, H. (2017). Hybrid Simulation of Composite Structures. Kgs. Lyngby: Technical University of Denmark (DTU). (DCAMM Special Report; No. S220).

DTU Library
Technical Information Center of Denmark

General rights
Copyright and moral rights for the publications made accessible in the public portal are retained by the authors and/or other copyright owners and it is a condition of accessing publications that users recognise and abide by the legal requirements associated with these rights.

- Users may download and print one copy of any publication from the public portal for the purpose of private study or research.
- You may not further distribute the material or use it for any profit-making activity or commercial gain
- You may freely distribute the URL identifying the publication in the public portal

If you believe that this document breaches copyright please contact us providing details, and we will remove access to the work immediately and investigate your claim.

Hybrid Simulation of Composite Structures

PhD Thesis

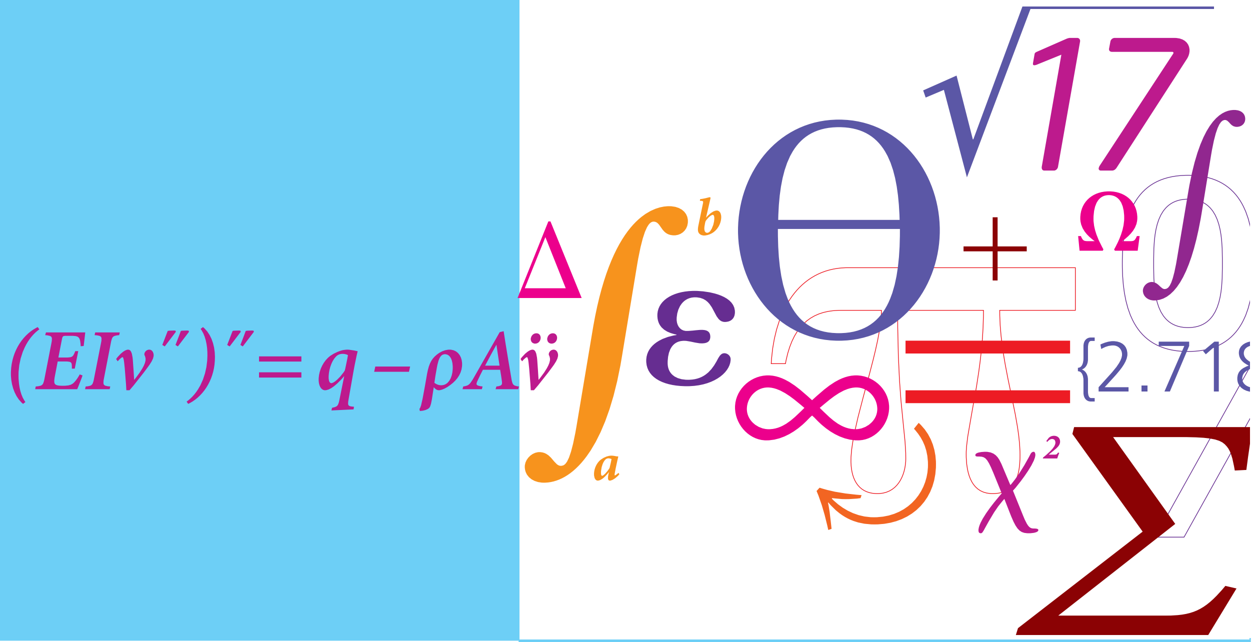

$(EIv'')'' = q - \rho A\ddot{v}$
Δ
$\int_a^b$
ε
Θ
$\sqrt{17}$
$+$
Ω
$\int$
∞
$=$
{2.718
χ^2
$\sum$

Jacob Herold Høgh
DCAMM Special Report No. S220
January 2016

DTU Mechanical Engineering
Department of Mechanical Engineering

Hybrid Simulation of Composite Structures

Jacob Herold Høgh

Kgs. Lyngby 2016

Preface

This thesis is submitted to fulfil the requirements for a Danish Ph.D. degree. The work presented was conducted at the Department of Mechanical Engineering, Technical University of Denmark and for a three months period at the Department of Civil- and Environmental Engineering, University of California, Berkeley. The project was supervised by main supervisor Associate Professor Christian Berggreen, Department of Mechanical Engineering and the co-supervisors: Professor Henrik Stang, Department of Civil Engineering, Associate Professor Jacob Wittrup-Schmidt, Department of Civil Engineering and Senior Scientist Kim Branner, Department of Wind Energy, all of which are associated with the Technical University of Denmark. At the external stay the project was supervised by Professor Khalid M. Mosalam, Civil and Environmental Engineering, University of California, Berkeley.

The project was funded partially by 2/3 by the Technical University of Denmark and 1/3 by Danish Centre for Composite Structures and Materials for Wind Turbines (DCCSM) funded by the Danish Council for Strategic Research within Sustainable Energy and Environment (Grant: 09-067212).

Kgs. Lyngby, December 2015

Abstract

Hybrid simulation is a substructural method combining a numerical simulation with a physical experiment. A structure is thereby simulated under the assumption that a substructure's response is well known and easily modelled while a given substructure is studied more accurately in a physical experiment. The technique has primarily been used within earthquake engineering but many other fields of engineering have utilized the method with benefit. However, these previous efforts have focused on structures with a simple boundary between the numerical and physical substructure i.e. few degrees of freedom. In this dissertation the main focus is to develop hybrid simulation for composite structures e.g. wind turbine blades where the boundary between the numerical model and the physical experiment is continues i.e. in principal infinite amount of degrees of freedom. This highly complicates the transfer system and the control and monitoring techniques in the shared boundary is therefore a key issue in this type of hybrid simulation. During the research, hybrid simulation platforms have been programmed capable of running on different time scales with advanced control and monitoring techniques at the shared boundary. The hybrid simulation programs have been tested on different simple composite structures and they have proven able to increase the accuracy in tests with a complex transfer system.

Resumé

Hybridtest er en substrukturel testmetode hvor en numerisk simulering bliver kombineret med en fysisk test. En konstruktion kan derved testes i det tilfælde hvor hoveddelen af konstruktionen er simpel at modellere numerisk imens en given subkonstruktion behøver et fysisk eksperiment pga. ukendte stivheds respons. Hybridtest er primært blevet anvendt inden for jordskælvstest af bygningskonstruktioner, men andre konstruktioner er også blevet testet med succes. De tidligere hybridtests har dog det til fælles, at de er udført på konstruktioner med en simpel rand i mellem den numeriske konstruktion og den fysiske test, dvs. få frihedsgrader. Denne afhandling fokuserer på anvendelsen af hybridtest på kompositkonstruktioner fx vindmøllevinger, hvor randen mellem den numeriske- og fysiske konstruktion er kontinuerlig med, i princippet, uendelig mange frihedsgrader. Dette øger kompleksiteten på overføringssystemet og avancerede styrings- og målemetoder er derfor nødvendige. I denne afhandling er forskellige hybridtestprogrammer blevet designet til at udføre hybridtest i forskellige tidsskalaer med avancerede styrings- og målemetoder til at håndtere den avancerede rand. Disse hybridtestprogrammer er blevet testet på forskellige kompositkonstruktioner og er blevet verificeret til at kunne øge nøjagtigheden af styringen af den fælles rand mellem den numeriske- og fysiske subkonstruktion.

List of Publications

Publications Included in Dissertation

J. P. Waldbjørn, J. H. Høgh, J. W.- Schmidt, M. W. Nielsen, K. Branner, H. Stang, C. Berggreen, *Strain and displacement controls by fibre Bragg grating and digital image correlation*, Strain, Vol. 50, No. 3, 2014, p. 262-273

J. P. Waldbjørn, J. H. Høgh, H. Stang, C. Berggreen, J. W.- Schmidt, K. Branner, *Hybrid Testing of Composite Structures with Single-Axis Control*, Proceedings of the 19th International Conference on Composite Materials, 2013

J. Høgh, J. P. Waldbjørn, J. W.- Schmidt, H. Stang, C. Berggreen, *Quasi-Static Single-Component Hybrid Simulation of a Composite Structure with Multi-Axis Control*, Strain, Vol. 51, 2015, p. 459-473

J. Høgh, S. Gunay, K. M. Mosalam, *Hybrid Simulation of D-string Stiffened Wind Turbine Blade*, to be submitted

J. Høgh, J. P. Waldbjørn, S. Andersen, C. Berggreen, *Compensation Methods in Real-Time Hybrid Simulation*, to be submitted

Other Publications

The following two journal papers was written with the contribution of undersigned during the PhD project, however, these publications are not included in the dissertation due to limited relevance:

M. W. Nielsen, J. W.-Schmidt, J. H. Høgh, J. P. Waldbjørn, J. H. Hattel, T. L. Andersen, C. M. Markussen, *Life cycle strain monitoring in glass fibre reinforced polymer laminates using embedded fibre Bragg grating sensors from manufacturing to failure*, Journal of Composite Materials, Vol. 48, No. 3, 2013, p. 365-381

J. Waldbjørn, S. Andersen, J. Høgh, Jacob W.-Schmidt, Christian Berggreen, Henrik Stang, *Single-component Multi-rate Real Time Hybrid Simulation pilot test on a composite structure*, to be submitted

Nomenclature

Latin

a	Acceleration
C	Damping matrix
D	Displacement vector
E	Young's modulus
e	Error between command and feedback signal
F	Force
f	Frequency
G	Shear modulus
h	Time step
I	Moment of inertia
i	Number of points in Lagrange polynomial
j	Analogue voltage signal
K	Stiffness matrix
k	Gauge factor for fibre Bragg grating fibres
L	Lagrange coefficient polynomial
M	Mass matrix
	Moment
m	Mass
	Subscript for x, y, z directions
N	Normal force
n	Time increment
P	Lagrange polynomial
R	Restoring/Reaction force
T	Temperature
t	Time
u	Displacement
V	Shear force
v	Velocity
x	Displacement vector
y	2nd axis in Cartesian coordinate system
z	3rd axis in Cartesian coordinate system

Greek

ε	Strain
λ	Wavelength
ν	Poisson's ratio
σ	Normal stress
τ	Torque
φ	Angle
ω	Angular frequency

Table of Content

INTRODUCTION 1

HYBRID SIMULATION CONCEPT 1
-*DENOMINATION – HYBRID SIMULATION* 2
MOTIVATION FOR HYBRID SIMULATION OF COMPOSITE STRUCTURES 2
OBJECTIVE OF THE RESEARCH 4

OVERVIEW OF PROGRESS IN HYBRID SIMULATION DURING RESEARCH 5

MULTI-COMPONENT VS. SINGLE-COMPONENT 7

TIMESCALES 9

TIME INTEGRATION 9
QUASI-STATIC 9
-*RAMP AND HOLD VS. CONTINUES LOADING* 10
PSEUDODYNAMIC 10
REAL-TIME 11

DELAY AND COMPENSATION 13

TIME DELAY 13
-*COMMUNICATION DELAY* 13
-*TRANSFER SYSTEM DELAY – ACTUATOR DYNAMICS* 13
COMPLIANCE AND INERTIA OF LOAD TRAIN 14
-*COMPLIANCE COMPENSATION* 14
-*INERTIA FORCE COMPENSATION* 14
INTERPOLATION AND EXTRAPOLATION METHODS 15
DATA ACQUISITION 16
-*DIGITAL IMAGE CORRELATION* 16
-*FIBRE BRAGG GRATING* 16

GENERIC THREE-AXIAL TEST SETUP 19

-*CONTROL AND DATA ACQUISITION* 19
CONTROL AND MEASUREMENT OF SHARED BOUNDARY 21
-*DISPLACEMENT CONTROL* 21
-*RESTORING FORCE MEASUREMENTS* 21
DYNAMIC VERIFICATION OF TEST SETUP 22

SUMMARY OF RESULTS 25

INTRODUCTION 25
STRAIN AND DISPLACEMENT CONTROLS BY FIBRE BRAGG GRATING AND DIGITAL IMAGE CORRELATION 26
-BACKGROUND AND OBJECTIVE 26
-FIBER BRAGG GRATING AND DIGITAL IMAGE CORRELATION TECHNOLOGY 26
-TEST SETUP AND COMPENSATION 26
-RESULTS 27
-CONCLUSION 28
HYBRID TESTING OF COMPOSITE STRUCTURES WITH SINGLE-AXIS CONTROL 29
-BACKGROUND AND OBJECTIVE 29
-EMULATED STRUCTURE AND PARTITIONING IN NUMERICAL AND EXPERIMENTAL SUBSTRUCTURE 29
-HYBRID SIMULATION PROGRAM 29
-RESULTS 30
-CONCLUSION 31
QUASI-STATIC SINGLE-COMPONENT HYBRID SIMULATION OF A COMPOSITE STRUCTURE WITH MULTI-AXIS CONTROL 32
-BACKGROUND AND OBJECTIVE 32
-EMULATED STRUCTURE 32
-HYBRID SIMULATION PROGRAM ARCHITECTURE 32
-RESULTS 33
-CONCLUSION 34
HYBRID SIMULATION OF D-STRING STIFFENED WIND TURBINE BLADE 35
-BACKGROUND AND OBJECTIVE 35
-EMULATED STRUCTURE AND PARTITIONING IN NUMERICAL AND EXPERIMENTAL SUBSTRUCTURE 35
-HYBRID SIMULATION SETUP 35
-RESULTS 35
-CONCLUSION 36
COMPENSATION METHODS IN REAL-TIME HYBRID SIMULATION 37
-BACKGROUND AND OBJECTIVE 37
-TEST SETUP 37
-COMPENSATION FOR LOAD TRAIN COMPLIANCE AND INERTIA 38
-RESULTS 39
-CONCLUSION 40

CONCLUSION 43

LIST OF FIGURES 45

REFERENCES 47

PUBLICATIONS 51

Introduction

Hybrid Simulation Concept

Hybrid simulation is a substructural testing method where a structure is emulated by a numerical model and a physical experiment. The numerical model represents the main part of the structure while the physical experiment represents a given substructure of special interest. When running the hybrid simulation the external load is applied the numerical model and the actions at the shared boundary between the model and the experiment is sent to the experiment. The actions from the experiment are then measured and fed back to the numerical model for the subsequent time step. The concept of the test is outlined by a classical test setup; cf. Fig. 1 where a steel frame structure is modelled numerically while a structural damper is tested in the experiment. In this example the steel frame is applied a ground acceleration due to earthquake, displacements, velocities and accelerations are determined at the shared boundary to the structural damper (part B) and these are applied the experiment to retrieve the restoring force of the damper. In the subsequent time step the force from the damper is applied the finite element model in order to account for the force of the damper. This procedure is continued in an iterative process to simulate the behaviour of the building structure for the entire loading history (Williams, 2007).

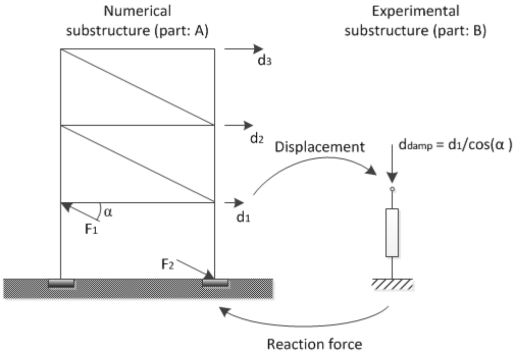
Numerical substructure (part: A)
Experimental substructure (part: B)
d_3
d_2
Displacement
$d_{damp} = d_1/\cos(\alpha)$
α
F_1
d_1
F_2
Reaction force

Fig. 1 Typical application of hybrid simulation for earthquake engineering

The benefit of the procedure is in the case where the response of the main part of a structure is well known and therefore easily modelled numerically while a given section of the structure has unknown response (Jacobsen, et al., 2010) and (Wu, et al., 2005). Furthermore the method is beneficial in such applications where it is not possible to test the entire structure but only a small substructure, i.e. wind turbine blades, high-rise buildings etc. for the real-life loading scenario. In these examples the sheer size of the structure makes a physical experiment too expensive or comprehensive to perform. The method furthermore has benefits compared to substructural testing in terms of the possibility of applying more accurate actions and studying the complex interaction between the shared boundary of the physical and numerical model.

Hybrid simulation was developed for application in earthquake engineering in the late 1960s (Takanashi & Nakashima, 1987) as an alternative to shaking table testing where the entire structure had to be included in full scale or scaled to appropriate size. Due to the initial application of earthquake engineering much efforts has been invested in real-time (Bonnet, et al., 2008) and pseudodynamic hybrid simulations (Shing, et al., 1996), Hybrid simulations is inherently a complicated procedure due to the noise from the physical experiment iteratively being fed into an numerical model/time integration which already has stability issues (Shing & Mahin, 1987), (Mercan & Ricles, 2008). Much effort has therefore been invested in developing implicit and explicit time integration schemes (Saouma & Sivaselvan, 2008) (primarily modifications of the Newmark time integration algorithm (Newmark, 1959)), compensation techniques (Ahmadizadeh, et al., 2008) and improvement of calculation speed

(Pan, et al., 2006). These methods will be described in further detail in the following. Due to the extensive studies within hybrid simulation it is a well proven technique and it has been applied to many different fields of engineering, among others; earthquake, automobile, aviation, robotics, aerospace etc. However, no efforts have been invested in performing hybrid simulations on composite structures which this research focusses on.

Denomination – Hybrid Simulation

In the literature several terms exists to describe the substructural testing approach used in this project e.g. hybrid simulation, hybrid testing (Bonnet, et al., 2007), hardware-in-the-loop (Facchinetti & Bruni, 2012), real-time substructuring (Verma & Rajasankar, 2012), on-line testing (Nakashima & Masaoka, 1999) and others. The most common in recent journal papers are probably "Hybrid simulation" which is used especially in Asian and north American publications, but the term "hybrid testing" is also commonly seen. This however, primarily accounts for simulations in earthquake engineering and other civil- and mechanical engineering applications, while in other fields, such as electronics, the term "Hardware-In-the-Loop" is more common. The title of this dissertation uses the "Hybrid simulation" denomination due to the more recent consensus among authors worldwide, however in the first conference proceedings by undersigned the term "hybrid testing" was used due to that being the initial title of the PhD project. However, all of these terms refer to the same substructural approach of a structure being partially simulated numerically and partially tested experimentally. The iterations in the hybrid simulation are in this dissertation referred to as "*time steps*".

Motivation for Hybrid Simulation of Composite Structures

The main motivation behind the project was to apply hybrid simulation to wind turbine blades and other large scale composite structures, cf. aeroplanes, ships, automobiles etc. The size of wind turbines are increasing rapidly the recent years due to the increasing focus on green energy as an alternative to fossil fuels and due to the recent advances in composite materials and structures making the construction possible. Wind turbine blades have reached length of > 80m and these blades are expensive and almost impossible to test in a laboratory due to the sheer size and complex aeroelastic loading from wind (Hansen, 2004), gravity, centripetal forces etc. (Jensen, et al., 2006), (Schubel & Crossley, 2012). The large blades are usually validated by full scale flapwise and edgewise bending tests using a limited amount of loading points and by material/coupon level testing (Jensen, 2008). However, if it is desired to study the behaviour of a given section of interest of the wind turbine blade under a real loading scenario the bending tests does not give the accurate loading conditions. In hybrid simulation it is possible to study the behaviour of a certain section of interest thoroughly in tests where the complex interaction between the numerical substructure and the physical test is present. Several studies have identified local fracture phenomena in wind turbine blades to be crucial to the load capacity of the wind turbine blade (Eder, et al., 2014). In all of these instances it might be beneficial to perform a hybrid simulation where the substructure experiencing failure could be studied in a physical experiment while the remaining structure is modelled numerically. In Fig. 2 examples of local fracture phenomena which might be beneficial to study in hybrid simulation.

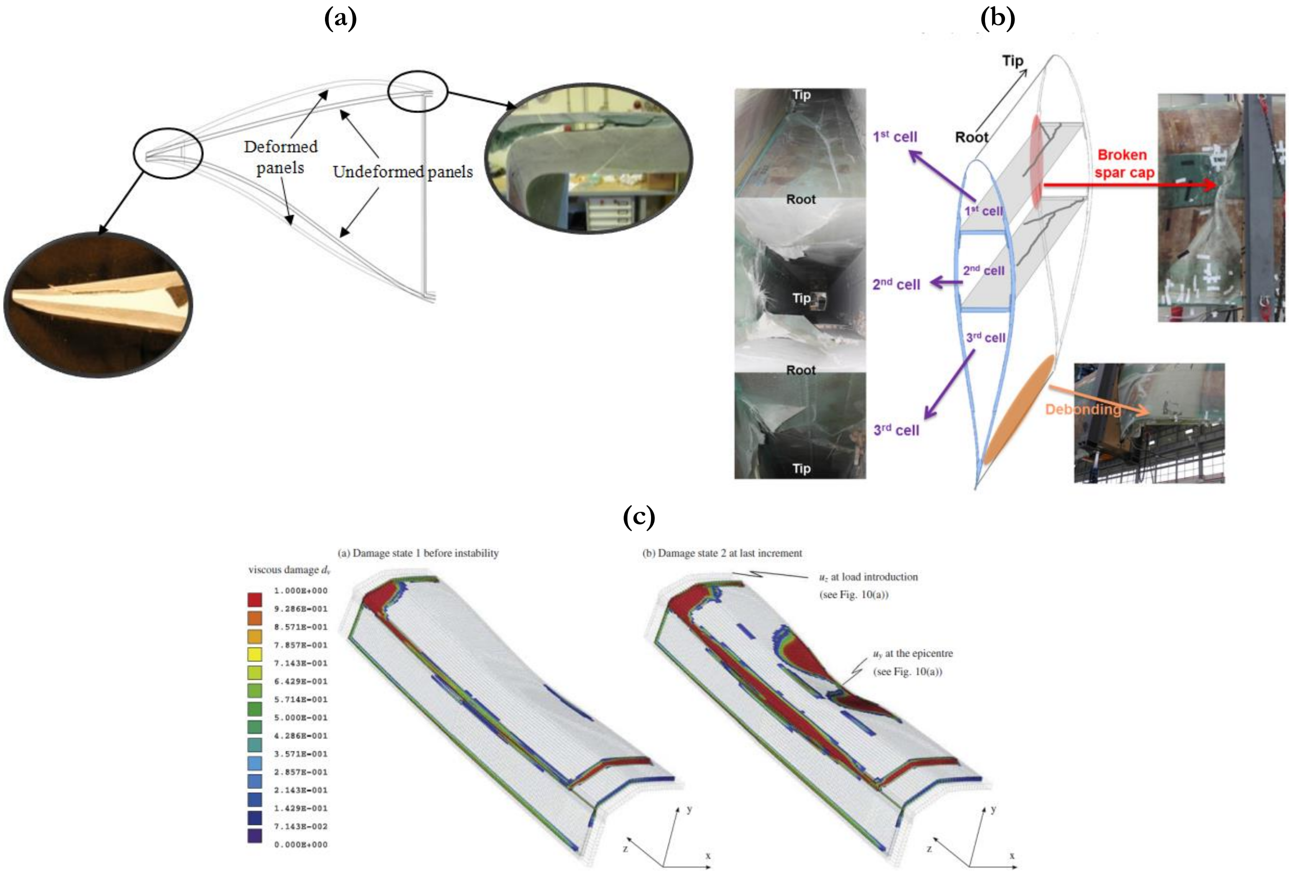
(a)
Deformed panels
Undeformed panels
(b)
Tip
Root
Tip
Root
Tip
Root
Tip
1st cell
2nd cell
3rd cell
1st cell
2nd cell
3rd cell
Broken spar cap
Debonding
(c)
(a) Damage state 1 before instability
(b) Damage state 2 at last increment
viscous damage d_v
1.000E+000
9.286E-001
8.571E-001
7.857E-001
7.143E-001
6.429E-001
5.714E-001
5.000E-001
4.286E-001
3.571E-001
2.857E-001
2.143E-001
1.429E-001
7.143E-002
0.000E+000
u_z at load introduction (see Fig. 10(a))
u_y at the epicentre (see Fig. 10(a))
x
y
z

Fig. 2 Local fractures in wind turbine blades (a) test by Bladena A/S (Bladena A/S, 2015) fracture in trailing edge and between shear web and spar cap (b) multiple local failure phenomena in trailing edge shear webs connections etc. (Lee & Park, 2016) (c) Local buckling phenomena in the compressive spar cap (Overgaard, et al., 2010)

Due to the fact that no hybrid simulation was performed at the Technical University of Denmark (DTU) before this research the focus was first and foremost to develop a platform capable of running a simple hybrid simulation. Hereafter the platform can be further developed to include the necessary components in order to perform the hybrid simulation on a more advanced structure i.e. a wind turbine blade.

The hybrid simulation is in general an interdisciplinary field of research due to the combination of a finite element analysis with an experiment. Hybrid simulation therefore includes theories such as: control theory, finite element analysis and programming. However, for composite structures the hybrid simulation complexity is increased due to the advanced boundary between the numerical model and the experimental substructure. The different fields of engineering and technologies concerning these are listed in the following. Each field of research are accompanied by a reference suggested in order to get a proper introduction of the main theory:

- Hybrid simulation and time integration (Saouma & Sivaselvan, 2008) and (Carrion & Spencer Jr., 2007)
- Programming in LabVIEW with special emphasize on parallel programming (Bitter, et al., 2007)
- Mechanics of Composite materials (Bunsell & Renard, 2005) and (Zenkert & Battley, 2006) and sandwich structures (Zenkert, 1995)
- Finite element analysis (Cook, 1995)
- Structural Dynamics (Inman, 2001)
- Control theory including: PID control, delay caused by actuator dynamics, compensation for compliance and other (Ellis, 2000) and (Saouma & Sivaselvan, 2008)

Fig. 3 Examples of generic three-rotor offshore wind turbines (Krenk, 2010) similar to the ones studied in (Bladena A/S, 2015), (Lee & Park, 2016), (Overgaard, et al., 2010)

Objective of the Research

The objective of the PhD thesis is to investigate the possibility of performing hybrid simulation on composite structures with special focus on wind turbine blades. This includes identifying the benefits and shortcomings of hybrid simulation of composite structures, handling of advanced boundary conditions in terms of monitoring and control, building a sound hybrid simulation platform capable of performing hybrid simulation at different timescales and finally testing these algorithms in hybrid simulations. The objectives of the research are listed in the following:

- Identify key differences in hybrid simulation of composite structures i.e. benefits and shortcomings compared to traditional applications
- Identify suitable application for hybrid simulation for composite structures, with special focus on wind turbine blades
- Develop versatile hybrid simulation program capable of running simulation in different timescales
- Implement known compensators needed in order to perform the hybrid simulations or develop new if necessary
- Design a versatile testing platform and load train capable of performing hybrid simulations of composite structures
- Identify valid verification methods for evaluation of the hybrid simulations

Overview of Progress in Hybrid Simulation during Research

The progression in the hybrid simulation performed is outlined in Fig. 4. The complexity of the hybrid simulation is evaluated for each publication in terms of four parameters: Time Scale, Compensation, FEM and Experiment. Time scale describes whether the simulation was quasi-static pseudo-dynamic or real-time and complexity/computational resources used for the time integration e.g. explicit vs. implicit. The Compensation parameter describes which compensators were used e.g. compliance, communication delay, inertia force etc. The FEM is evaluated in terms of number of elements, element formulation, linear vs. non-linear and dynamic vs static. The Experiment is evaluated in terms of linear vs. non-linear, geometry, boundary conditions, transition zone etc. The publications are listed based on when the research was performed not when published. In Fig. 4 it is seen that the general level of complexity is increasing over time and more effects are included in the hybrid simulations.

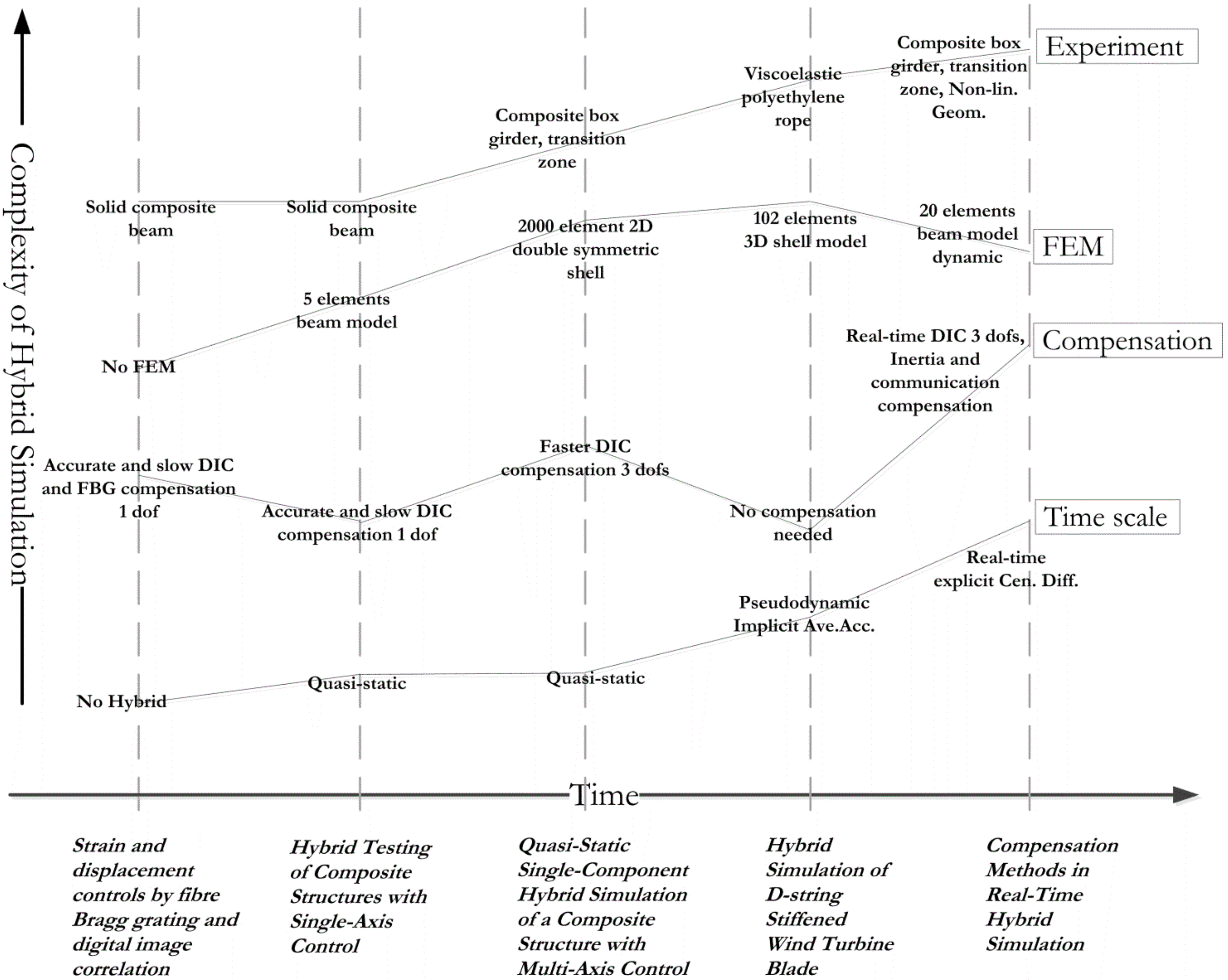
Complexity of Hybrid Simulation
Time
Experiment
FEM
Compensation
Time scale
Solid composite beam
Solid composite beam
Composite box girder, transition zone
Viscoelastic polyethylene rope
Composite box girder, transition zone, Non-lin. Geom.
No FEM
5 elements beam model
2000 element 2D double symmetric shell
102 elements 3D shell model
20 elements beam model dynamic
Accurate and slow DIC and FBG compensation 1 dof
Accurate and slow DIC compensation 1 dof
Faster DIC compensation 3 dofs
No compensation needed
Real-time DIC 3 dofs, Inertia and communication compensation
No Hybrid
Quasi-static
Quasi-static
Pseudodynamic Implicit Ave.Acc.
Real-time explicit Cen. Diff.
Strain and displacement controls by fibre Bragg grating and digital image correlation
Hybrid Testing of Composite Structures with Single-Axis Control
Quasi-Static Single-Component Hybrid Simulation of a Composite Structure with Multi-Axis Control
Hybrid Simulation of D-string Stiffened Wind Turbine Blade
Compensation Methods in Real-Time Hybrid Simulation

Fig. 4 The overall progress in the hybrid simulations performed during the research. The x-axis represents time/publications and the y-axis the complexity of each of the four evaluation parameters, being; Experiment, FEM, Compensation and Time Scale

Multi-component vs. Single-component

During the research within hybrid simulation, composite structures and wind turbine blades it was discovered that the shared boundary between the numerical and experimental substructure can be categorized into Mult-component or Single-component (Waldbjørn, et al., 2016). In Multi-component hybrid simulation the shared boundary is ideally a point, such as a hinge in an MR earthquake damper (Lin & Christenson, 2009). Depending on the construction of the given joint the amount of degrees of freedom will vary between 1-6 (3 translations and 3 rotations). In Single-component hybrid simulation the shared boundary is separating the finite element model and the physical experiment through a continues entity e.g. an edge, volume etc. The amount of degrees of freedom is infinite in principle. However, due to the physical nature of the given problem it might be adequate to simplify the shared boundary to few degrees of freedom as performed in (Waldbjørn, et al., 2016) and (Høgh, et al., 2016). In the case of Multi-component hybrid simulation it is in general simple to monitor and control the shared boundary since a point measurement e.g. linear variable differential transducer (LVDT), rotational variable differential transducer (RVDT), strain gauges, load cell etc. is adequate to fully determine the behaviour of the boundary. No assumptions are therefore needed to be made about the displacement, strain and stress distribution of an edge, continuum etc. In Single-component hybrid simulation, several measurements are needed to be made on the shared boundary in order to fully describe the actions acting on it. Furthermore, one will most likely need to make assumptions about how the edge, volume etc. behaves since actions can only be applied in an absolute amount of actuators. Another issue arising in Single-component hybrid simulation is stress concentrations. When applying loads to an edge by an actuator, stress concentrations will arise in this region close to the loading point. It is therefore necessary to make a transition zone on the specimen that cannot be considered part of the specimen since the stress, strains etc. are not correctly applied. The shared boundary on the specimen tested is therefore not in the edge of it but rather a certain distance from the loading insertion. The differences between Multi-component and Single-component hybrid simulation are outlined in Fig. 5 with sketches of two thought examples of each approach.

In Fig. 5a) a Multi-component hybrid simulation is outlined by a three-storey steel frame building with a viscous damper installed at the lower floor to damp earthquake vibrations. The steel frame is modelled numerically due to the linear elastic behaviour while the damper is tested in the physical experiment due to the non-linear behaviour and strain rate effects; cf. damping term is velocity dependant. The shared boundary is here a simple Charnier and only one action, being translations, are transferred between the substructures. The thought example of a Single-component hybrid simulation is a wind turbine blade where the entire blade is simulated except for a section of the shear web. The reason this might be interesting could be because of local buckling effects fracture, etc. The shared boundary in this case would be complicated and a transition zone could be introduced by including the spar caps for load applications.

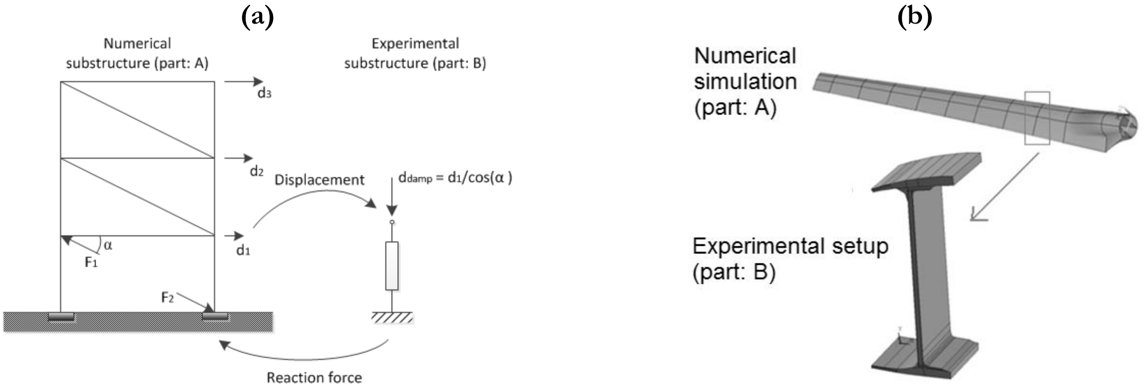
(a)
Numerical substructure (part: A)
Experimental substructure (part: B)
d3
d2
Displacement
ddamp = d1/cos(α)
d1
α
F1
F2
Reaction force
(b)
Numerical simulation (part: A)
Experimental setup (part: B)

Multi-Component Hybrid Simulation

- *Several components in emulated structure*
- *Simple connection between numerical model and experimental test*
- *Few degrees of freedom in boundary*
- *Simple to transfer actions between experimental structure and numerical model*

Single-Component Hybrid Simulation

- *One component in emulated structure*
- *Complex connection between numerical model and experimental test*
- *Infinite degrees of freedom in boundary*
- *Advanced monitoring techniques*
- *Residual stresses in structure due to fabrication*
- *Transition zone might be needed*

Fig. 5 The key properties of the shared boundary in (a) Multi-component and (b) Single-component hybrid simulation

In this dissertation, both Multi-component and Single-component hybrid simulation has been performed and it is noted that both are suited for wind turbine blades. The Multi-component hybrid simulation is relevant for hybrid simulation of retrofitted elements that are connected to the wind turbine blade in a simple shared boundary as is the case with D-string stiffeners inserted in order to limit the trailing edge opening (Høgh, et al., 2016). The Single-component hybrid simulation is appropriate when testing of larger plate panels or sections of the blade where there is no simple boundary between the numerical model and physical experiment. When cutting such a section out residual stresses as result of curing (Nielsen, et al., 2013) might also give rise to erroneous stresses at the boundary which also causes the need for a transition zone in the specimen. The state of the art is that no Single-component hybrid simulation has yet been performed on wind turbine blades. However, the research presented in this dissertation accommodates for some of the issues in such a simulation.

Timescales

Hybrid simulation started as a method for testing structures' response to earthquakes and the dynamic effects has therefore been included from the beginning even though the first tests only included dynamic effects in the finite element models and not in the experiment. In the following section the three different timescales in hybrid simulation, being; quasi-static, pseudo-dynamic and real-time are outlined. Furthermore, the benefits and shortcomings for each time scale are outlined and a few applications of each are referred.

Time integration

In dynamic simulation time integration is often used to solve the equation of motion of the structure, cf. eq. (1). In hybrid simulation most time integration schemes are based on the Newmark time integration scheme, (Newmark, 1959).

$$\boldsymbol{Ma} + \boldsymbol{Cv} + \boldsymbol{Kx} = \boldsymbol{F} \tag{1}$$

Time integration schemes can be divided into two categories: explicit and implicit. Explicit schemes calculates the state of a system to a future time $n+1$ based solely on the state of the system at time n. Implicit time integration schemes calculates the state of a system at a future time $n+1$ based on an equation involving the state of the system at time n and at time $n+1$. During this research two different time integration schemes have been applied: the explicit Central Difference method for real-time (Høgh, et al., 2016) and the implicit Average Acceleration (Høgh, et al., 2016) for pseudodynamic testing.

Quasi-static

The most simple hybrid simulation is quasi-static simulation. In this time scale no dynamics of the emulated structure are included and the equation of motion is therefore reduced to equilibrium between the external loading vector $\mathbf{F}$ to the sum of the elastic force of the numerical structure $\mathbf{Kx}$ and the restoring force of the experimental subsection $\mathbf{R}$.

$$\boldsymbol{Kx} + \boldsymbol{R} = \boldsymbol{F} \tag{2}$$

In this case no time integration is needed and the numerical model can be solved by a static finite element analysis. It is not necessary to compensate for actuator dynamics or other time delays due to communication between e.g. data acquisition systems such as digital image correlation or controllers, since time is not an issue in this matter. However, it is necessary to compensate for the communication delay given the fact that the experimental subsection yields a restoring force equivalent to the displacement for the previous iteration step.

Since the timing is not relevant the hybrid simulation program can run a state machine structure as outlined in (Bitter, et al., 2007) and a concrete example of such a program is presented in (Høgh, et al., 2015). The method is suitable for structures subjected to static loads with one section behaving nonlinearly. In this research the quasi-static approach was used in (Høgh, et al., 2015) and (Waldbjørn, et al., 2013). In (Carrion & Spencer Jr., 2007) the method is mentioned as an alternative to real-time and pseudodynamic testing for laboratories without the necessary computational resources to perform time integration and no dynamic capabilities of the actuators and/or controllers.

Ramp and Hold vs. Continues Loading

Timing is not irrelevant even though no dynamic effects are included. This is due to the force relaxation in materials. The testing procedure is outlined in Fig. 6 where the hybrid simulation is divided into ramp and hold phases; during the hold phases the finite element model is solved for the given time step. In this time the force relaxes, cf. Fig. 6 right which is a source of error. For this reason it is still desired to run the FEM as fast as possible even for a quasi-static hybrid simulation. However, a method was suggested in order to avoid stress relaxation during the "hold" phases in (Hughes, et al., 1979). The method is a predictor/corrector where the upcoming displacement is predicted by the previous time steps and when the numerical calculations are done a Corrector adjusts the command signal to move towards the next displacement step.

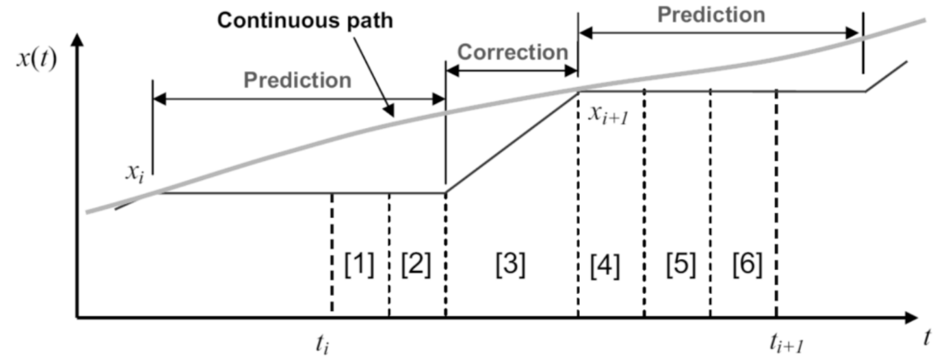

Fig. 6 Force relaxation in a ramp and hold compared to a continues loading approach cf. (Carrion & Spencer Jr., 2007)

Pseudodynamic

The concept of pseudo-dynamic hybrid simulation covers simulations where the finite element model is run as a dynamic analysis, while the experiment is run statically (Mercan & Ricles, 2008). The equation of motion is presented in eq. (3) where the **M** is the mass matrix, **C** the damping matrix, **K** the stiffness matrix, R the restoring force vector from the experimental substructure and the F is the external load vector applied the finite element model. The **a**, **v** and **x** vectors are the acceleration, velocity and displacement, respectively. The time integration can is usually performed for some variation of the Newmark algorithm (Newmark, 1959), such as the implicit average acceleration method as in (Chen, et al., 2014) and (Høgh, et al., 2016) or the operator splitting method (Pinto, et al., 2004). The main shortcomings of the model are that the correct strain rate and dynamic effects i.e. damping and inertia, is not included in the physical experiment. The strain rate is critical to applications such as MR dampers in building structures. The inertia effects are critical in the case of heavy physical substructure. However, this can be accommodated for by including the mass of the experimental substructure in the mass matrix M, as done in (Pinto, et al., 2004).

$$\boldsymbol{Ma} + \boldsymbol{Cv} + \boldsymbol{Kx} + \boldsymbol{R} = \boldsymbol{F} \tag{3}$$

This type of simulation does essentially not set any other requirements to computational speed of the finite element code than does the quasi-static hybrid simulation, since the experiment is run at low rates independent of the rate of the external loading. The noise in pseudodynamic hybrid simulation can be characterised as random error e.g. A/D conversion and measurement equipment noise and systematic errors e.g. inadequate response of the servo-hydraulic or electric actuators (Shing & Mahin, 1987) and communication delay (Maghareh, et al., 2014).

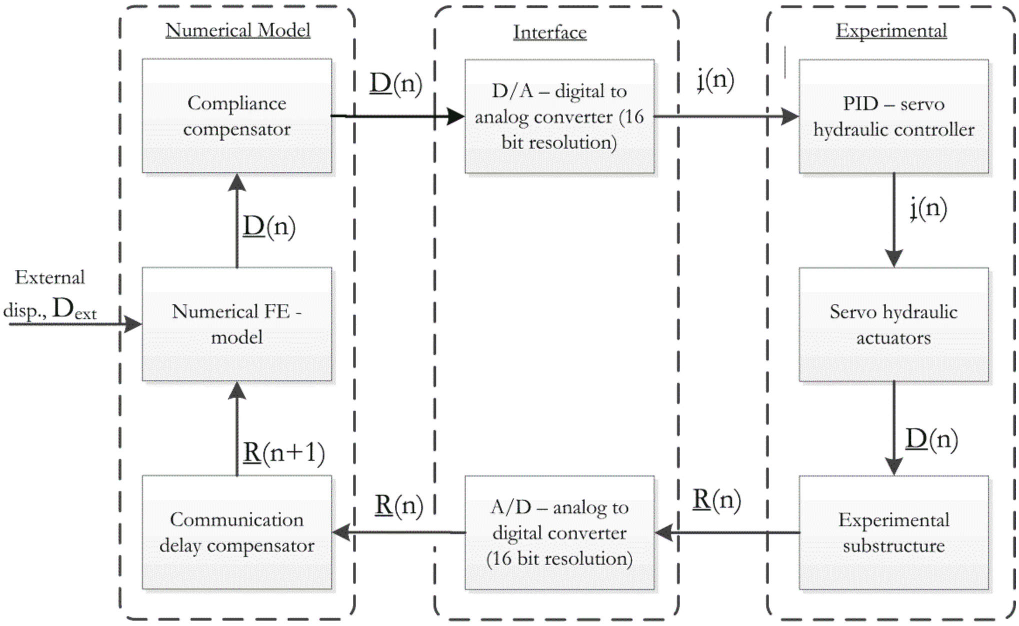
Numerical Model
Interface
Experimental
Compliance compensator
D(n)
D/A – digital to analog converter (16 bit resolution)
j(n)
PID – servo hydraulic controller
D(n)
j(n)
External disp., D_ext
Numerical FE - model
Servo hydraulic actuators
R(n+1)
D(n)
Communication delay compensator
R(n)
A/D – analog to digital converter (16 bit resolution)
R(n)
Experimental substructure

Fig. 7 Generic quasi-static or pseudodynamic hybrid simulation communication flow chart. The flow chart is from (Høgh, et al., 2015) but slightly modified so the processes are generic

The program architecture for a pseudo-dynamic hybrid simulation is equal to the one from the quasi-static with the one exception that the finite element model is run as time integration instead of a static analysis. The data communication between the finite element model and the experiment is the same as for quasi-static hybrid simulation due to experimental substructure being tested statically. Concerns of computational time are equivalent to those for quasi-static hybrid simulation where timing is not an issue other than for the sake of force relaxation, cf. chapter: "*Ramp and Hold vs. Continues Loading*". The data communication in a pseudodynamic hybrid simulation between the numerical substructure the interface program (LabVIEW (Høgh, et al., 2015), OpenFresco (Høgh, et al., 2016) or others) and the experimental substructure (i.e. controller and data acquisition system) is outlined for a generic hybrid simulation program in Fig. 7.

During this dissertation pseudodynamic hybrid simulation was utilized for a simulation of a D-string stiffener embedded into a wind turbine blade in order to limit opening of sandwich panels in trailing edge section (Høgh, et al., 2016). In this test the implicit average acceleration time integration scheme was included. This was an ideal setup for pseudodynamic approach due to the dynamic effects of the physical substructure being negligible compared to the numerical model.

Real-Time

In real-time hybrid simulation both the numerical model and the physical experiment is loaded dynamically at the correct rate. The equation of motion is essentially the same as the one presented in eq. (3), except the restoring force from the physical substructure is including the dynamic contributions. In the real-time approach the time integration must thereby run as fast as the experiment and often for small time steps to ensure stability of the integration scheme and this sets great challenges for the computational resources on the hardware. This also limits the complexity of the finite element model compared to pseudodynamic and quasi-static.

Different time integration schemes has been developed and implemented for real-time hybrid simulation, such as explicit schemes; e.g. central difference, operator splitting (Wu, et al., 2005), direct integration algorithm (Cheng & Ricles, 2008), and furthermore implicit schemes, e.g. unconditionally stable implicit scheme (Shing, et al., 1991), generalized alpha methods (Chung & Hulbert, 1993) and others. The integration schemes are classified as unconditionally stable of conditionally stable. Stability is defined as no increase in displacement amplitudes for a free vibration test (i.e. no damping). Unconditionally stable means that the time integration is stable for all time steps sizes *h*. conditionally stable means that the time integration scheme is only stable for time steps smaller than a certain threshold value, $h < h_{\max}$.

A generic real-time hybrid simulation program communication flow is outlined in Fig. 8. Opposed to the program architecture outlined Fig. 7, here multiple processes runs simultaneously and a parallel programming software must therefore be utilized, e.g. LabVIEW or MatLab Simulink. The flow chart is valid for e.g. the simulation in (Høgh, et al., 2016) and is a parallel modified producer consumer loop. A producer consumer loop means that one loop produces data while the other processes it. The modification comes since here both loops are producers and consumers and must run at the same speed, since the FEM always needs the latest restoring force and the physical experiment needs the command signals from the code. In the presented generic approach the first producer/consumer loop includes a control program handling the: Interpolation/Extrapolation, Communication delay, A/D and D/A conversion. A finite element code handles the time integration and an external hardware handles the compliance compensation (if any). The second producer/consumer loop handles the application of commands signals and restoring force measurements by a PID controller.

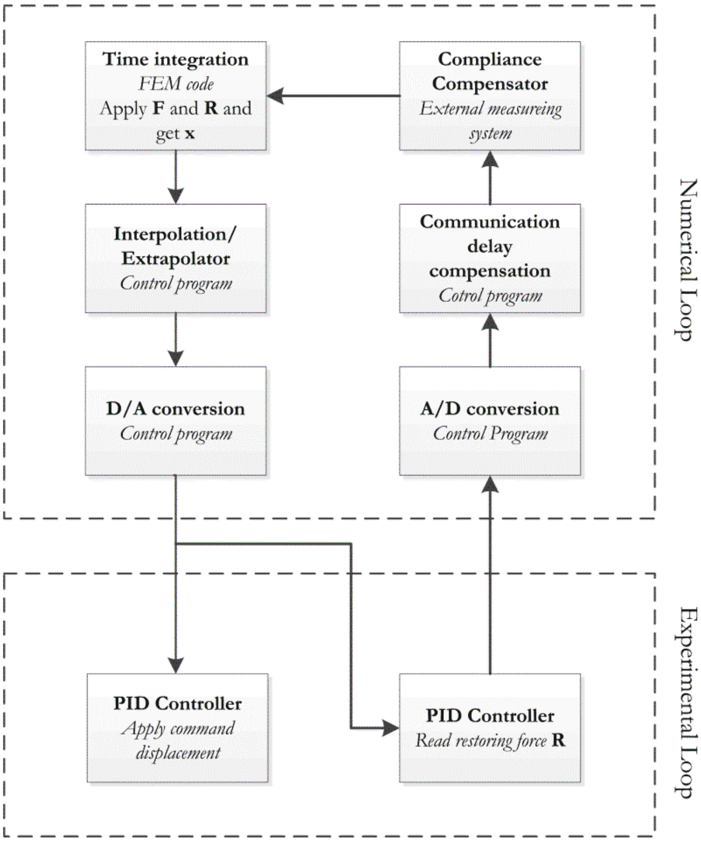
Time integration
FEM code
Apply F and R and get x
Compliance Compensator
External measureing system
Interpolation/ Extrapolator
Control program
Communication delay compensation
Cotrol program
D/A conversion
Control program
A/D conversion
Control Program
Numerical Loop
PID Controller
Apply command displacement
PID Controller
Read restoring force R
Experimental Loop

Fig. 8 Example of a generic real-time hybrid simulation program

Delay and Compensation

In the following is a description of common control, compensation and data acquisition techniques utilized in hybrid simulation. General description of the main concepts is given, but this section puts the main focus on the techniques used and/or developed in the publications' by the author. These techniques were the ones found suitable for hybrid simulation of Single-component structures or other wind turbine blade or composite hybrid simulations applications.

Time Delay

Communication Delay

Communication delay is describing the delay caused by the finite element model being one time step in front of the actuator, i.e. the restoring force. The communication delay causes a decrease in stiffness of the experimental structure when increasing loading and an increase in stiffness of the experimental structure when unloading. The size of the communication delay depends on the size of the load increments, i.e. larger load increments yields larger communication delays. Communication delay is an inherent part of a hybrid simulation for all time scales and must therefore always be compensated for. In (Høgh, et al., 2015) two communication delay compensator was utilized, the first was a linear compensator using the 3 or 4 point compensator using the previous restoring forces and external forces to extrapolate the restoring force by least square linear regression. The compensator was included with limited success due to instability issues when the forces changed sign. The other compensator attempted in the study was a third or fourth order Lagrange compensator, cf. eq. (4), where P is the Lagrange polynomial as function of the external load F, given as the sum of all the Lagrange coefficient polynomials L_i and the restoring force for the i'th amount of points. This compensator was unfortunately not successful due to instability due to noise and the studies therefore not documented in the publication (Høgh, et al., 2015).

$$P_n(F) = \sum_{i=0}^{n} R_i(F) L_i(F) \tag{4}$$

Another compensator was later included in the real-time hybrid simulation in (Waldbjørn, et al., 2016) with success. The compensator used Lagrange but extrapolated the next restoring forces based on restoring force as function of time instead of external load.

Transfer System Delay – Actuator Dynamics

Transfer system delay is defined as the time lag between a commanded signal from the numerical model and the feedback signal from the actuator. This leads to an error in the hybrid simulation that causes negative damping which can result in instabilities if the effective damping of the system is negative (Ahmadizadeh, et al., 2008) and (Chen & Tsai, 2013). Much effort has been invested in compensation methods for transfer system delay. Examples of this is the feed-forward phase lead compensator (Chen & Tsai, 2013), adaptive inverse technique (Chen, et al., 2012), prediction by third order polynomial fitted to previous displacement values (Horuichi, et al., 1999) and a discrete third order inverted compensator (Phillips & Spencer, 2011). In (Høgh, et al., 2016) a direct inverted first order compensator is utilized for transfer system compensation.

Compliance and Inertia of Load Train

Compliance Compensation

Depending on the compliance of the load train compared to the compliance of the specimen it might be necessary to compensate for the displacements in the load train by on-specimen measurements. In (Høgh, et al., 2015) large compliance of the load train was observed yielding in erroneous displacements being applied the specimen when using the actuator LVDT measurements for control in the tests. For Single-component hybrid simulation several actuators, an advanced load train and a transition zone might be necessary.

It is therefore likely that compliance compensation is needed. The method used in (Høgh, et al., 2015) and (Høgh, et al., 2016) was integrating DIC measurements in an outer control loop correcting the actuator displacements in the following time step, cf. eq. (5) and (6). In the equations $\mathbf{D}_c$ is the command displacement vector, $\mathbf{K}_{DIC}$ the gain vector, $\mathbf{e}$ the error vector, $\mathbf{D}_{c0}$ the desired displacements, $\mathbf{D}_{DIC}$ the displacements measured by DIC, n denotes the time step. The approach is similar to the one used in (Spencer, et al., 2015), except DIC is used instead of LVDTs. DIC was also used for control in an outer loop in (Fayolle, et al., 2007) but not in a hybrid simulation In the quasi-static tests it was possible to run the compensator with a gain of 1.0 but in the real-time test such a high gains caused instability and gains in the range of $\mathbf{K}_{DIC}$ = [0.0075; 0.010] was used instead. The equations are referring to DIC measurements but the same procedure can be applied for other types of on-specimen measurements.

$$\boldsymbol{D}_c(n) = \boldsymbol{K}_{DIC}\boldsymbol{e}(n-1) + \boldsymbol{D}_{c0}(n) \tag{5}$$

$$\boldsymbol{e}(n-1) = \boldsymbol{D}_c(n-1) - \boldsymbol{D}_{DIC}(n-1) \tag{6}$$

Inertia Force Compensation

Inertia force compensation must be applied in real-time hybrid simulation in the case that the mass of the load train is high enough to cause a considerable inertia force compared to the restoring force from the experimental substructure (Høgh, et al., 2016). The inertia actions in dynamic oscillations consist of six different actions, being forces and torques in three axes and around these three axes, respectively. The inertia forces and torques are presented in eq. (7) and (8), F is the force, m the mass, a the acceleration, τ the torque, I the moment of inertia, a the angular acceleration and t the time. The mass and moment of inertia in different directions might not easily be calculated if the load train consists of multiple parts as was the case in (Waldbjørn, et al., 2016). It is therefore suggested to perform an oscillation test where the specimen is not inserted in the load train. In this way the mass and moment of inertia around the three axis of rotation can be determined as the slope in a force/torque versus acceleration/angular acceleration plot as done in (Høgh, et al., 2016). For most applications several of these force and torque contributions might be negligible, e.g. few degrees of freedom in the shared boundary or if displacements are predominately in one direction.

$$F_m(t) = ma_m(t) \;\; for\, m = x, y, z \tag{7}$$

$$\tau_m(t) = I_m\alpha_m(t) \;\; for\, m = x, y, z \tag{8}$$

The accelerations and angular accelerations can be measured by accelerometers or they can be derived from the displacements and rotations measured by the actuator LVDTs and RVDTs or other instruments, e.g. DIC, cf. eq. (9) and eq. (10). However this approximate differentiation yields noise and filtering might be needed. If filtering is applied it should be done before differentiation for optimal results. Alternatively it is suggested to use the command signal to calculate the force and/or torques since this signal has less noise than the feedback.

However, this is only valid in the case of good correspondence between the command and feedback signal of the actuator.

$$F(t) = m\frac{d^2x}{dt^2} \cong m\frac{\Delta^2 x}{\Delta t^2} = m\frac{x_2 - 2x_1 + x_0}{\Delta t^2} \tag{9}$$

$$\tau(t) = I\frac{d^2\varphi}{dt^2} \cong I\frac{\Delta^2 \varphi}{\Delta t^2} = I\frac{\varphi_2 - 2\varphi_1 + \varphi_0}{\Delta t^2} \tag{10}$$

Interpolation and Extrapolation Methods

Controllers usually runs at frequencies higher than 1.0 kHz, cf. (Material Testing Systems, MTS, 2015) in order to ensure a smooth transfer of the displacements and thereby not introducing high frequent noise in the test. However, if the time integration is running at lower frequencies (which is usually the case, cf. time step *h* > 10ms) the controller is missing points and this can be solved by using an Interpolator. The interpolation algorithm determines command signals between the time steps and thereby ensures a smooth displacement transfer. The procedure is outlined in Fig. 9a) and different approach can be applied for this such as a third order polynomial fitting, (Bonnet, et al., 2008).

In a real-time hybrid simulation the actuator must always run and never stop to wait for a command signal, since this will lead to incorrect velocities and accelerations of the shared boundary. In order ensure this one must ensure that the time integration runs for a time step so long that the actuator will always have a command signal in the queue. However in this case the program does not exploit the full computational resources of the hardware since time integration will be inactive for faster sub steps. These unused computational resources can be utilized using an extrapolator (Elkhoraibi & Mosalam, 2007). In this approach the time integration does not have to be done until before the actuator is done applying the previous time step, since the program extrapolates the next time step and sends this as a command to the controller. When the time integration is done the extrapolated signal is then corrected, see procedure sketched in Fig. 9b). This approach has been used with success in several studies (Elkhoraibi & Mosalam, 2007). The extrapolator can be performed using the same polynomial as used for interpolation.

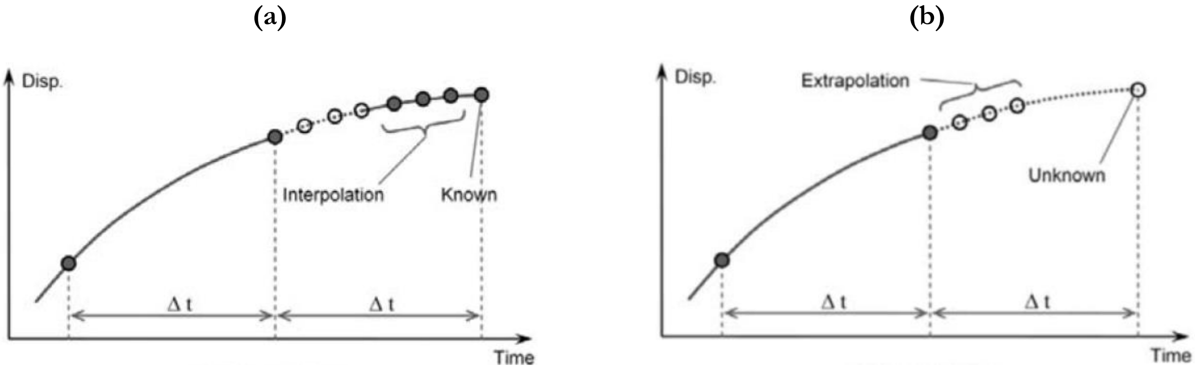

Fig. 9 Example of (a) interpolation between known displacement points and (b) extrapolation of the command signal in order to get command signal to the actuators, cf. (Shing, 2008)

Data Acquisition

In Multi-component hybrid simulations measurements are usually performed by LVDT and load cell in the actuators solely. In this research two advanced measuring techniques has been utilized and outlined in the following.

Digital Image Correlation

Digital image correlation is a non-contact full-field measurement technique for 3D or 2D measurements. In the studies only 3D DIC has been utilized due to the benefits compared to 2D DIC being; the possibility of alignment of the displacements according to the specimen and actuators instead of cameras, 3D displacement measurements for evaluation of out-of-plane measurements. DIC uses two techniques to determine strains and displacements: image matching and photogrammetry. Photogrammetry relates the displacements in the digital image to real displacements by a calibration. In the calibration a calibration object with known dimensions are photographed from various positions and the sensors thereby calculates the intrinsic (aperture, lens distortion etc.) and extrinsic (camera orientations) parameters i.e. (Sutton, et al., 2009). Image matching matches the images from the two cameras using by dividing each digital image into facets of a certain amount of pixels and matches the same facet for the two images from the two sensors. The size of the facet is a compromise between high spatial resolution i.e. few pixels per facets to get many measurement points and high displacement resolution i.e. many pixels per facets to get few but more accurate displacement. The facets size also depends on the material tested i.e. metals has a more homogeneous strain distribution than composites, hence large facet points are needed for composites to get a more homogeneous strain field. The DIC measurements can be evaluated by the parameters listed in Table 1.

Table 1 Comprehensive table of DIC parameters modified version of table in (Høgh, et al., 2015)

Technique used	3D Image Correlation
Facet	20 pixel
Overlay	3 pixel
Sensor	4M 1" CCD chip
Focal length	20mm
Field of View	960mm x 960mm
	2048 x 2048 pixel
Measurement points	24818
Displacement	
Spatial resolution	20 pixel
Resolution, σ	
Standard dev.	
In-plane	5.1 μm x 3.5 μm
Out-of-plane	21.7 μm

Fibre Bragg Grating

Fibre Bragg grating is a technique for strain measurements in points. Light is emitted through an optic fibre and reflected at the Bragg gratings. The gratings are a series of thousands of reflective layers positions at a distance of λ_0 between. When light hits the grating it is reflected and refracted cf. Fresnel equation and the light with the same wavelength of λ_0, as the sensor, is amplified by constructive interference and visible to the interrogator as a peak. A change in the sensors length e.g. equivalent to a strain in the material can be traced by a change in the reflectivity of the sensor $\Delta\lambda$. In eq. (11) the correlation between wavelength and strain is determined by a gauge factor k_ε and a contribution from the temperature change multiplied by the gauge factor k_T.

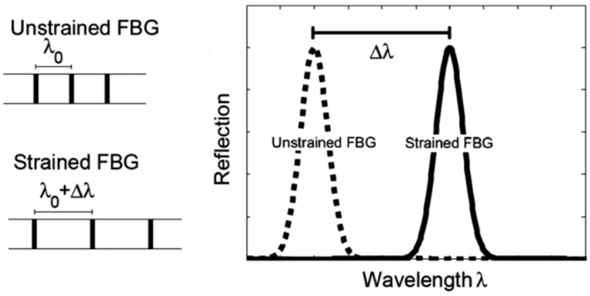
Unstrained FBG
λ_0
Strained FBG
$\lambda_0+\Delta\lambda$
$\Delta\lambda$
Reflection
Unstrained FBG
Strained FBG
Wavelength λ

Fig. 10 Schematic illustration of the FBG concept (Høgh, et al., 2015)

$$\frac{\Delta\lambda}{\lambda_0} = \varepsilon k_{\varepsilon} + k_t \Delta T \tag{11}$$

Generic Three-Axial Test Setup

During the project a three-axial test setup was designed in order to be able to test specimens in 2D in three degrees of freedom i.e. vertical and horizontal displacements and in-plane rotations. The test setup consisted of 3 actuators inserted into an adjustable steel beam structure and the three actuators are connected together by a steel structure, cf. Fig. 11. The figure shows the setup with a specimen installed that was used in the hybrid simulation presented in (Høgh, et al., 2015) however, with minor modifications other profiles can be inserted into the setup for hybrid simulation. The vertical actuator A can be moved along the entire length between the vertical columns in order to adjust to different specimen lengths and the horizontal actuators B and C can be moved up and down as well as the support for the specimen.

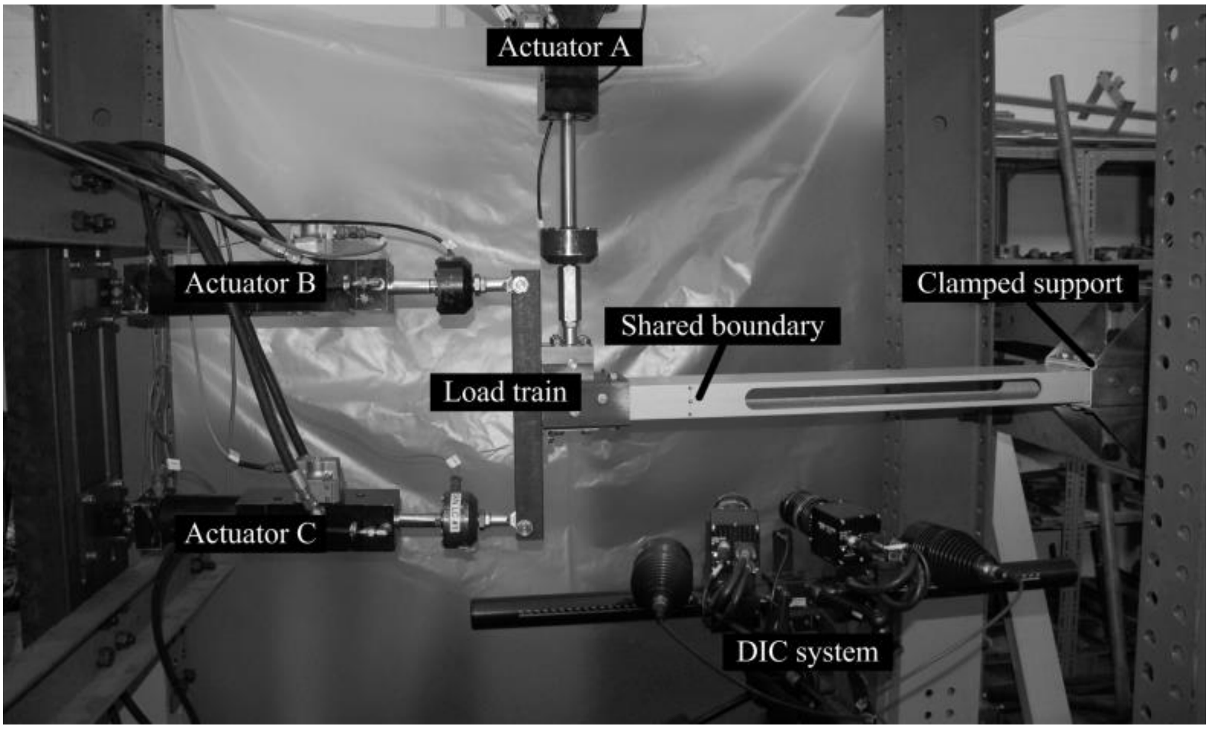

Fig. 11 Three-axial test setup for testing in-plane cf. (Høgh, et al., 2016)

Control and Data Acquisition

The vertical actuator has a capacity of 25kN and stroke of static 182.9mm, dynamic 152.4mm and the horizontal actuators has a capacity of 5kN and a stroke of 114.3mm, dynamic 101.6mm each. The accuracy of the system is evaluated in terms of standard deviation of noise in the case for a test performed with zero displacements and forces applied the specimen. 40000 measurements were then taken and the standard deviation of noise is listed for each actuator in terms of displacement and force, cf. Table 2, cf. (Waldbjørn, et al., 2016).

Table 2 Standard deviation of error of the noise in displacement and force measurements of the test setup (Waldbjørn, et al., 2016)

	actuator A	actuator B	actuator C
Displacement (SD) [mm]	0.0103	0.0016	0.0017
Force (SD) [N]	1.66	1.12	3.67

A 12M digital image correlation system is setup for measurements and control in an outer control loop for real-time pseudodynamic or quasi-static hybrid simulations. The accuracy of the DIC setup is evaluated in terms of standard deviation of noise for a series of points taken with zero displacements applied. The data is presented in (Høgh, et al., 2016). The values are the displacements and rotations in the shared boundary and the out-of plane displacements for a series of 2000 measurements, cf. Table 3.

Table 3 Standard deviation (SD) of error of displacements and rotation

SD u_x [μm]	SD u_y [μm]	SD φ_z [°]	SD u_z [μm]
0.419	4.157	1.108e-3	0.777

The maximum force capacity of the test setup is calculated by the force capacity of each actuator and the geometrical lengths of the setup cf. Table 4. The moment and normal force capacity is dependant and an MN-diagram for the test setup is presented in Fig. 12.

Table 4 Maximum moment normal force and shear force of the test setup

M_{max} [kNm]	N_{max} [kN]	V_{max} [kN]
±1.40	±10.0	±25.0

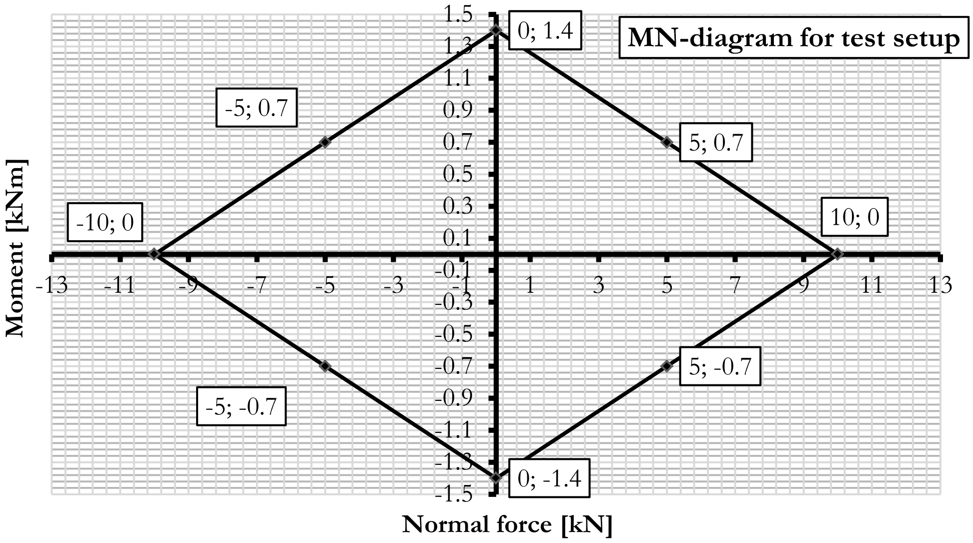

Fig. 12 Moment and normal force diagram (MN-diagram) for the test setup, the shear force capacity is independent of the moment and normal force applied

The setup is connected to an MTS TestStar II analogue controller with capacity of 4 channels (i.e. actuators in control) and generation of command signal at 3kHz. The controller is connected to a PC running the control software and the setup has two options for connection to a LabVIEW based hybrid simulation code. One is a quasi-static or pseudo dynamic hybrid simulation code running on a PC and communicating to the controller through a LabVIEW NI9263 for output and NI9205 for input board developed in (Høgh, et al., 2015) and presented in Fig. 7. The benefit of this code is the ability of running a generic ANSYS code making it versatile for generic numerical substructuring and the shortcoming is the computational speed of ANSYS is not able to run in real-time. The other option is a real-time program developed in (Waldbjørn, et al., 2016) running on a LabVIEW board of the type NI cRIO9074, generic code for real-time documented in Fig. 8. The program is able to run at computational speeds of up to 50Hz for simple FE models. However the downside is the lack of generic finite element capacity given the fact that the MatLab program running the FEM must be designed uniquely for every hybrid simulation.

Control and Measurement of Shared Boundary

Displacement Control

The displacements from the shared boundary in the finite element model are transferred to the specimen through the load train by the three actuators. The displacements in the actuators, $\mathbf{D}_{act}$, in order to obtain a given displacement in the shared boundary, d_x, d_y and φ_z, are determined by a trigonometric relation using the fix points of the actuators, cf. Fig. 13. The actuator displacements, eq. (12), are determined from the sum of the displacement in the shared boundary, d_x and d_y, and the contribution from the rotation of the shared boundary, $x_{m,\varphi}$ and $y_{m,\varphi}$, cf. eq. (20) and (21).

$$\mathbf{D}_{act}(\mathrm{n})=\begin{bmatrix}\sqrt{\left(x_A(n)-x_{A,fix}\right)^2+\left(y_A(n)-y_{A,fix}\right)^2}\\ \sqrt{\left(x_B(n)-x_{B,fix}\right)^2+\left(y_B(n)-y_{B,fix}\right)^2}\\ \sqrt{\left(x_C(n)-x_{C,fix}\right)^2+\left(y_C(n)-y_{C,fix}\right)^2}\end{bmatrix}^T \tag{12}$$

$$x_m(n)=x_{m,\varphi}(n)+d_x(n) \quad \text{for } m=A,B,C \tag{13}$$

$$y_m(n)=y_{m,\varphi}(n)+d_y(n) \quad \text{for } m=A,B,C \tag{14}$$

$$x_{m,\varphi}(n)=r_m \cos\left(\arccos\left(\frac{x_m(n-1)}{r_m}\right)+\varphi_z\right) \quad \text{for } m=A,B,C \tag{15}$$

$$y_{m,\varphi}(n)=r_m \sin\left(\arcsin\left(\frac{y_m(n-1)}{r_m}\right)+\varphi_z\right) \quad \text{for } m=A,B,C \tag{16}$$

Restoring Force Measurements

The test setup is controlled by three actuators connected in a load train, cf. Fig. 13. The sectional forces at the shared boundary: *N, V, M*, cf. eq. (19), (20) and (21) are calculated by the actuator forces R_A, R_B and R_C. The trigonometric relations between the actuator forces eq. (17) and the section forces in the shared boundary eq. (18) is derived using the actuators' supports, $x_{A,fix}$, $y_{A,fix}$ $x_{B,fix}$, $y_{B,fix}$ $x_{C,fix}$ and $y_{C,fix}$ and the angles in relation to the load train, cf. Fig. 13.

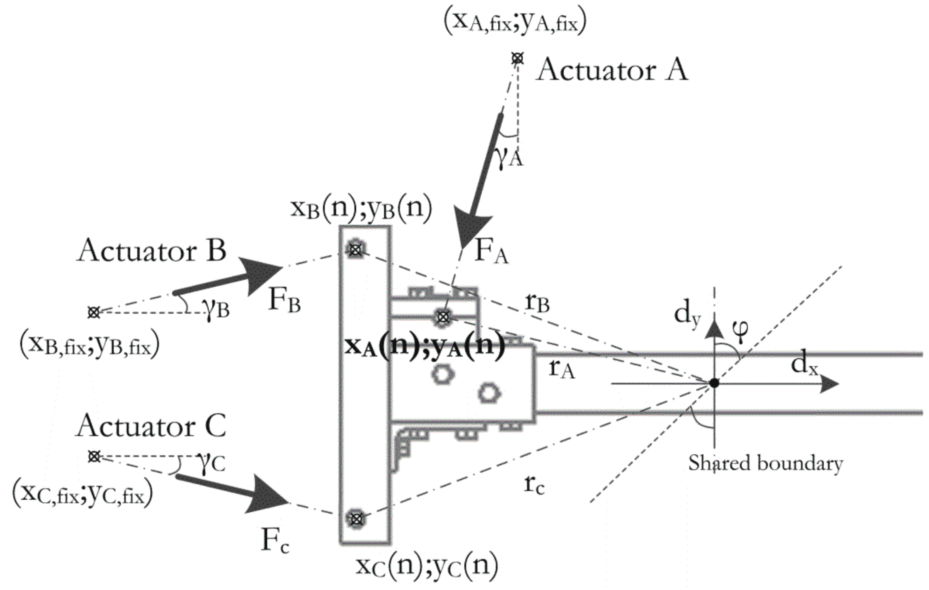

Fig. 13 The load train of the three axial load train, cf. (Høgh, et al., 2015)

$$\boldsymbol{R}_{act}(n)=[R_A(n)\ R_B(n)\ R_C(n)] \tag{17}$$

$$\boldsymbol{R}(n)=[R_V(n)\ R_H(n)\ M(n)] \tag{18}$$

$$R_V=R_A\cos(\gamma_A)+R_B\sin(\gamma_B)+R_C\sin(\gamma_C) \tag{19}$$

$$R_H=R_A\sin(\gamma_A)+R_B\cos(\gamma_B)+R_C\cos(\gamma_C) \tag{20}$$

$$\begin{aligned} M=&R_A\big(\cos(\gamma_A)\,(x_A(n)-x(n))+\sin(\gamma_A)(y(n)-y_A(n))\big)\\ &+R_B(\cos(\gamma_B)(y(i)-y_B(n))+\sin(\gamma_B)(x_B(n)-x(n)))\\ &+R_C(\cos(\gamma_C)(y(i)-y_C(n))+\sin(\gamma_C)(x_C(n)-x(n))) \end{aligned} \tag{21}$$

Dynamic Verification of Test Setup

The dynamic properties of the setup are evaluated by performing a test where no specimen is installed in the test setup and the actuators are set to oscillate in a sine curve for different frequencies. The restoring force is then logged as function of the acceleration calculated by eq. (9). The test was conducted for six frequencies, cf. Table 5 and the force versus acceleration is plotted for a frequency of $f = 2.96$ Hz, cf. Fig. 14. The purpose of the test is to determine the inertia force of the load train in order to be able to compensate for it, cf. chapter: "*Inertia Force Compensation*", the mass of the load train is determined as the slope of the force vs. acceleration curve and ideally it should be independent of the frequency at which the test is performed. However, in Table 5 it is observed that the slope i.e. mass, is varying greatly with the frequency of testing. It is fairly stable in the range of 1.48Hz – 3.70Hz and the value used in (Høgh, et al., 2016) is taken from this range.

Table 5 Calculated mass as function of frequency

f [Hz]	0.74	1.48	2.22	2.96	3.70	4.44
m [kg]	13.67	24.53	23.56	25.68	25.36	28.34

It is assumed that the large deviation in the mass for 0.74Hz is due to friction in the test setup's joints and bearings and the friction from moving the hoses of hydraulic oils. The discrepancy in mass is starting to increase when the frequency is higher than 4.44Hz and this is probably caused by the high frequent vibrations induced in the setup. Ideally the force vs. acceleration plot in Fig. 14 should be a straight line and follow the same path for increasing and decreasing accelerations. However, this was not the case and it is assumed that the discrepancy was due to the effects also affecting the mass, as described above.

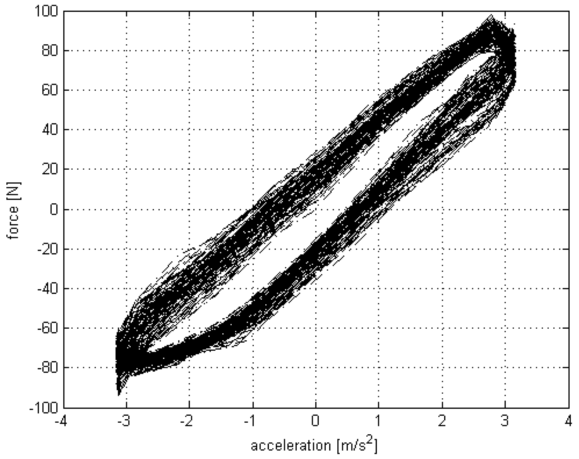

Fig. 14 The force as function of acceleration in the vibration test

Summary of Results

Introduction

In this chapter the publications written by the author is outlined with special emphasize on the context of the overall objective of the dissertation. The main objective of each paper is outlined together with the method, key findings and main conclusions. This chapter serves the purpose of outlining and connecting the publications and present the process of the project. Furthermore, key observations, theory, tests etc. not included in the publications is presented here in order to describe the whole framework and link the papers together.

The initial studies focus mainly on programming and testing of a basic quasi-static hybrid simulation programs (Waldbjørn, et al., 2013) and the development of compliance compensation methods for slow hybrid simulation (Waldbjørn, et al., 2013) i.e. quasi-static. Hereafter, the studies focus on more advanced shared boundary between the numerical model and the physical experiment and implementing the compensation methods for these setups (Høgh, et al., 2015). Hereafter more advanced finite element model is implemented for a pseudo-dynamic simulation (Høgh, et al., 2016) and finally the emphasis is put on development of compensation methods for the load train in a real-time hybrid simulation (Høgh, et al., 2016).

Strain and displacement controls by fibre Bragg grating and digital image correlation

J. P. Waldbjørn, J. H. Høgh, J. W.- Schmidt, M. W. Nielsen, K. Branner, H. Stang, C. Berggreen, Strain, Vol. 50, No. 3, 2014, p. 262-273

Background and Objective

Due to the challenges in controlling and monitoring of the shared boundary in Single-component hybrid simulation it is desired to develop control methods where measurements performed directly on the specimen can be used to control actuators and thereby omitting the compliance of the load train. This paper focuses on and outer control loop using digital image correlation or fibre Bragg Grating technology implemented in an outer control loop in order to increase accuracy.

Fiber Bragg Grating and Digital Image Correlation Technology

Fibre Bragg Grating is a technology where light is emitted through an optical fibre and reflected at premade gratings which are a set of semi reflective/transparent mirrors located at an intermediate distance of λ_0 (Kreuzer, n.d.). When the light is emitted only light of this wavelength is reflected and it can be measured by an interrogator. If the FBG is strained the reflective index changes by $\Delta\lambda$ (Chan, et al., 2006) and the strain ε can be measured as the shift in wavelength by the gauge factor k_ε and initial temperature cf. eq. (22). The method is thereby a point measurement technology and the user will only get a limited amount of point per optical fiber. The benefit of the method is that the fibres can be implemented in the given material during casting and thereby acquire strains from inside the specimen during the entire life cycle of the material (Nielsen, et al., 2013). In the given test an FBG system from Ibsen Photonics was used (Ibsen Photonics, 2009).

$$\frac{\Delta\lambda}{\lambda_0} = \varepsilon k_\varepsilon + k_t \Delta T \tag{22}$$

Digital image correlation is a full field non-contact measurement technique utilizing digital images from sensors to calculate strains and deformations of a surface. The technology can be two or three dimensional depending on the numbers of cameras used, cf. one camera (mono setup) yields 2D and two cameras (stereo setup) yields 3D measurement possibilities. In this test 3D was used due to the possibility of measuring on e.g. curved surfaces and the possibility of alignment according to specimen instead of cameras. The technology uses photogrammetry and image matching for calculation of displacements and strains (Sutton, et al., 2009). The DIC system used for the application is ARAMIS software by GOM (GOM, 2006) and programmed using python scripting function (GOM, 2006).

Test Setup and Compensation

The compensation program was tested on a three point bending setup of a composite beam embedded with FBG fibres and painted with a speckle pattern for DIC measurements. The compensation algorithm is programmed in LabVIEW and the components of the program are presented in Fig. 15. The program generates a command displacement and sends it to the PID controller by MTS through the dynamic link library (DLL) MTS LabVIEW communication (MTS, 2009). The data acquisition system i.e. FBG or DIC measures the feedback displacements/strain and transforms the displacement/strain measured to the displacement in the LVDT of the actuator. The actuator command is then compared to the DIC/FBG feedback and if an error higher than a predefined value is present the program sends a new command signal to the actuator to move equivalent to the measured error. This procedure is continued until next time step in an outer loop structure cf. Fig. 15.

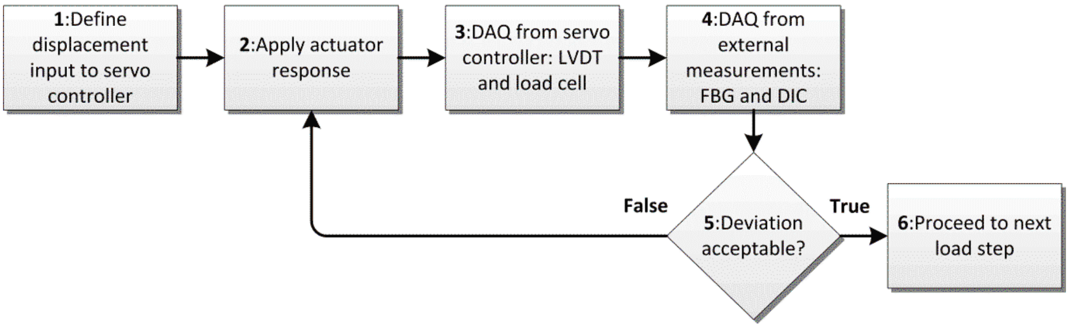
1:Define displacement input to servo controller
2:Apply actuator response
3:DAQ from servo controller: LVDT and load cell
4:DAQ from external measurements: FBG and DIC
5:Deviation acceptable?
False
True
6:Proceed to next load step

Fig. 15 Data flow of communication in FBG and DIC compensation program, cf. (Waldbjørn, et al., 2013)

Results

The FBG and DIC compensation loop is evaluated by running a 90 time steps triangle shape loading, cf. Fig. 16 and Fig. 17. The A) figures present the loading sequence while the B) figures presents the error between the command signal to the LVDT and the feedback displacement measured by FBG or DIC. The B) figures show that every time the error between command and feedback is larger than 20μm/m or 10μm the program corrects the time step. To reach this accuracy the FBG control needed 26 corrections per 90 time steps test i.e. one correction every 3.46 step. The DIC control needed 21 corrections for 90 steps, i.e. one correction every 4.35 steps. If the desired accuracy was increased the number of corrections per time step was increased and vice versa.

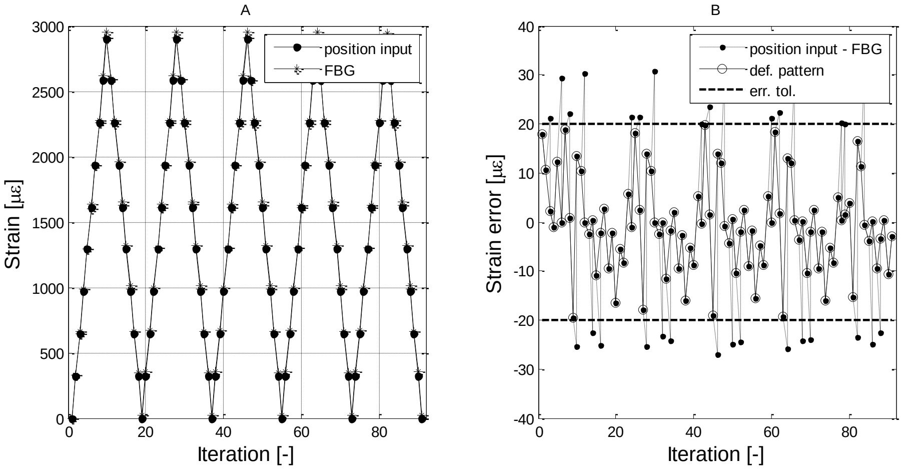

Fig. 16 Test sequence for the FBG controlled test A) the strain command vs DIC feedback B) the outer loop correction by FBG to an accuracy of 20μm/m, cf. (Waldbjørn, et al., 2013)

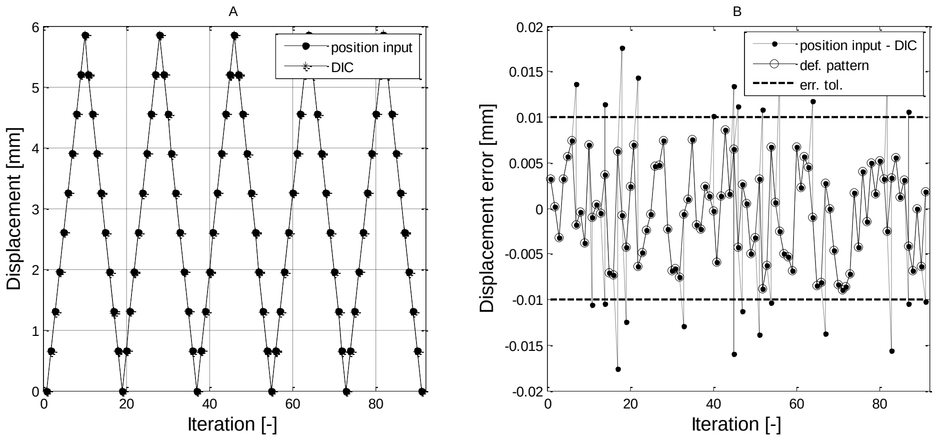

Fig. 17 Test sequence for the DIC controlled test A) the displacement command vs DIC feedback B) the outer loop correction by DIC to an accuracy of 0.01mm, cf. (Waldbjørn, et al., 2013)

Conclusion

A program was programmed in LabVIEW to be able to run tests using an MTS controller and measuring displacements or strains by DIC or FBG sensors and using these measurements to correct the displacements in and outer control loop. The program was thereby able to increase accuracy of tests by increasing the accuracy of the applied displacements. The effects and necessity of the compensation program depends on the compliance of the load train. In the given test the load train had low compliance and yet the accuracy could be improved. The compensation program is later to be used in hybrid simulations where the load train has high compliance such as in possible Single-component hybrid simulations.

Hybrid Testing of Composite Structures with Single-Axis Control

J. P. Waldbjørn, J. H. Høgh, H. Stang, C. Berggreen, J. W.- Schmidt, K. Branner, Proceedings of the 19th International Conference on Composite Materials, 2013

Background and Objective

The objective of this study was to design a hybrid simulation platform capable of running a finite element model, control an actuator and compensate for the compliance in the load train by a compensation algorithm developed in (Waldbjørn, et al., 2013). In order to prove the validity of the program it was chosen to focus on a program structure for quasi-static and pseudo-dynamic simulation. Furthermore, it was chosen to perform the hybrid simulation on a Multi-component structure in order to limit the analysis and verify the program before continuing with a Single-component structure.

Emulated structure and partitioning in numerical and experimental substructure

The hybrid simulation program was tested on a Multi-component structure, cf. Fig. 18. The numerical model was a 4 element steel frame structure and the experimental model was a composite beam tested in a three point bending setup developed in (Waldbjørn, et al., 2013). The setup is a Multi-component setup due to the simplicity of the boundary.

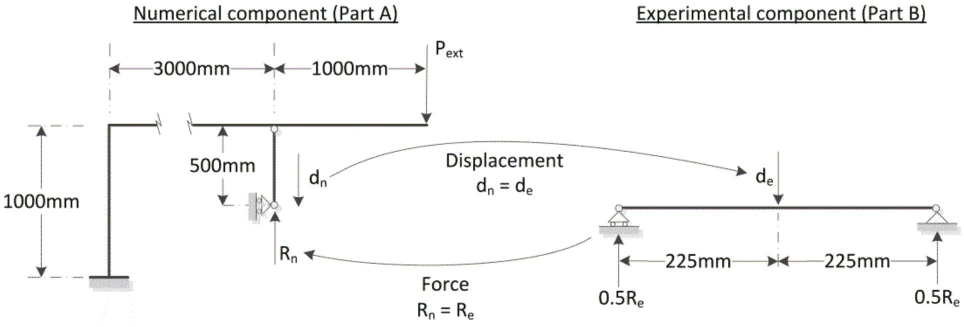

Fig. 18 Structure emulated in the hybrid simulation was a frame structure, part A is the numerical component and part B the experimental (Waldbjørn, et al., 2013)

Hybrid Simulation Program

The hybrid simulation program was developed in LabVIEW capable of communicating with a MTS controller to command displacements to an actuator and to acquire feedback signals here from. The program communicated with ANSYS for FEM modelling by the command prompt, which can later be used to perform more advanced FE models of more comprehensive structures. The hybrid simulation program had architecture of a state machine structure. The state machine is a while-loop structure outlined in Fig. 19. The program is a while loop running through five sub processes for every time step. First the external load was applied the finite element model in ANSYS which generated the command signal, hereafter the command signal was applied the specimen by a PID controller. The error in the displacement due to compliance was corrected by DIC in the compensation method developed in (Waldbjørn, et al., 2013). Finally the restoring force in the specimen was measured and fed back to the finite element program for running of the subsequent time step.

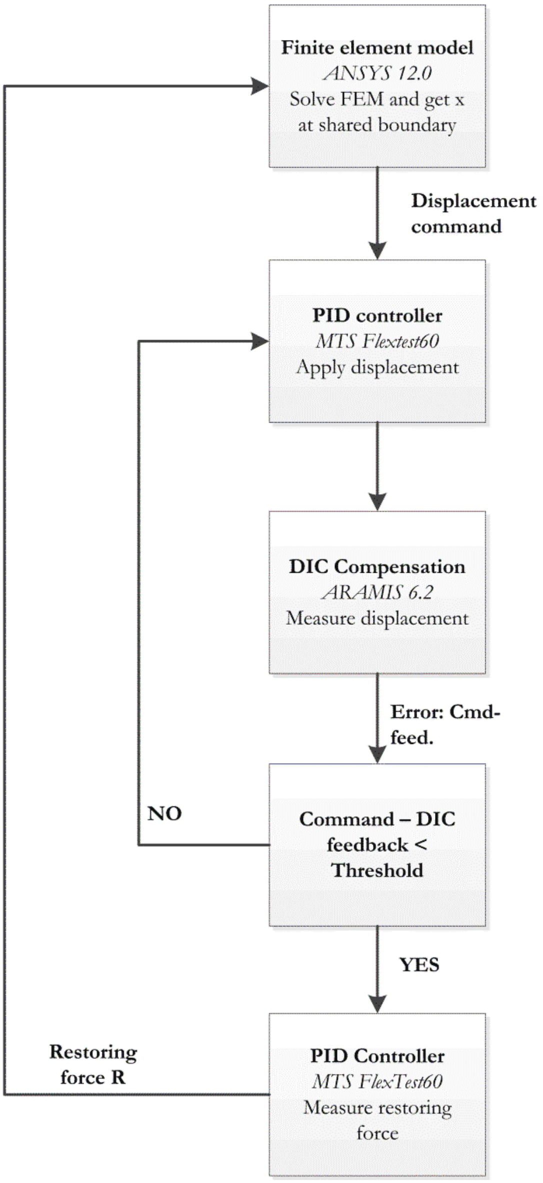
Finite element model
ANSYS 12.0
Solve FEM and get x at shared boundary
Displacement command
PID controller
MTS Flextest60
Apply displacement
DIC Compensation
ARAMIS 6.2
Measure displacement
Error: Cmd-feed.
NO
Command – DIC feedback < Threshold
YES
Restoring force R
PID Controller
MTS FlexTest60
Measure restoring force

Fig. 19 The structure of the LabVIEW state machine hybrid simulation program where the data flow is divided into 5 sub processes. Each process is headlined with the overall process, the software/hardware used and explanatory text of action performed.

Results

In order to validate the hybrid simulation it was compared to two simulations. The first was a finite element of the entire structure and the second an analytical hybrid simulation where the hybrid simulation was used to run the FEM but instead of the experiment a simple analytical equation was set to represent the structure. The comparison with these was used to see if any measurement noise etc. would create erroneous results in the finite element simulation. The three simulations were compared by the displacement in the shared boundary for every time step cf. Fig. 20. It was seen that the error between the models was less than 0.038mm for every time step for displacements up to 6mm, which yields a maximum error of 0.63%. The iteration speed of the program was 0.09Hz which makes the program suited only for quasi-static or pseudo-dynamic testing. Large iteration time was mainly due to the finite element model running ANSYS which reads and writes to the hard drive for every run and the DIC compensation that iterates the displacement until a desired threshold error is obtained.

In the study the stability of the hybrid simulation loop was tested by performing an analytical hybrid simulation, as described. It was therefore possible to change the stiffness of the experiment compared to the numerical model and study how this affected the stability of the hybrid simulation. It was seen that the simulation becomes instable if the stiffness of the finite element model is less than that of the experimental substructure. This is due to the fact that the restoring force would be greater than the external load required to yield a certain displacement of the finite element model this would change the direction of the displacement of the numerical structure for the subsequent time step. The equilibrium in the shared boundary would thereby no longer be present and instability occurring.

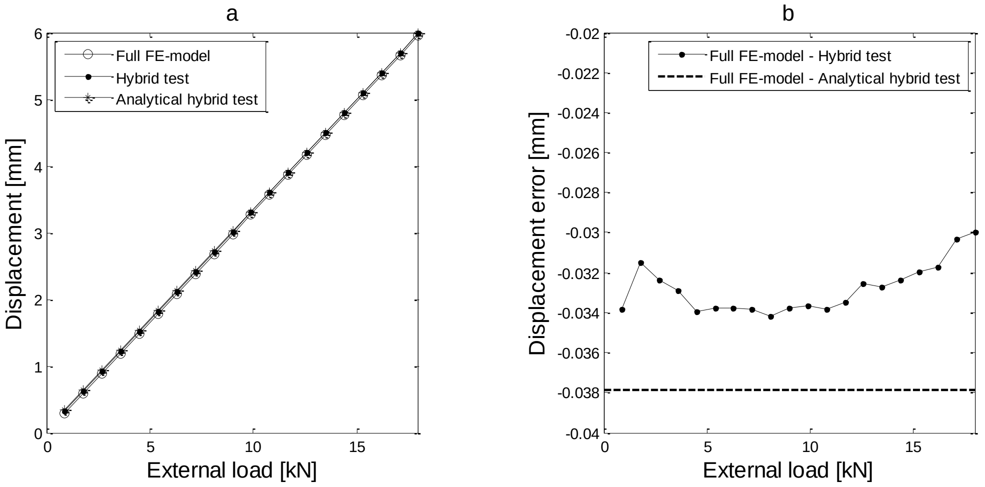

Fig. 20 The comparison of the hybrid simulation to the full FEM of the emulated structure and the analytical simulation of the hybrid simulation (Waldbjørn, et al., 2013)

Conclusion

A hybrid simulation was performed and the hybrid simulation program thereby defined for future use. Advanced control methods were implemented for quasi-static and pseudo-dynamic use. The shared boundary was at this point still very simple i.e. one DOF in order to validate the program and to implement the control methods on a simple setup. The hybrid simulation results were compared to a full FEM and analytical hybrid simulation yielding a discrepancy of less than 0.63% for all time steps.

Quasi-Static Single-Component Hybrid Simulation of a Composite Structure with Multi-Axis Control

J. Høgh, J. P. Waldbjørn, J. W.- Schmidt, H. Stang, C. Berggreen, Strain, Vol. 51, 2015, p. 459-473

Background and Objective

The objective of this study was to test the hybrid simulation program on a Single-component structure and to improve the displacement compensation by DIC to run faster. Furthermore the program architecture was to be rebuilt in order to prepare the program for real-time hybrid simulation by implementing new producer/consumer architecture instead of the state machine approach previously used.

Emulated Structure

The emulated structure tested in the experiment was a double clamped glass fibre reinforced polymer beam with slits cut in top flange in order to initiate non-linear behaviour due to buckling. The structure was divided into numerical and experimental substructures on the middle cf. Fig. 21. It is seen that the test is a Single-component hybrid simulation due to the complexity of the shared boundary. In this study it was chosen to simplify the actions at the boundary to three DOFs under the assumption of no deformations due to shear, cf. Bernoulli-Euler beam theory. In order to verify the validity of the hybrid simulation program a reference test was also performed where the entire structure was tested. The results from this could then later be compared to the hybrid simulation.

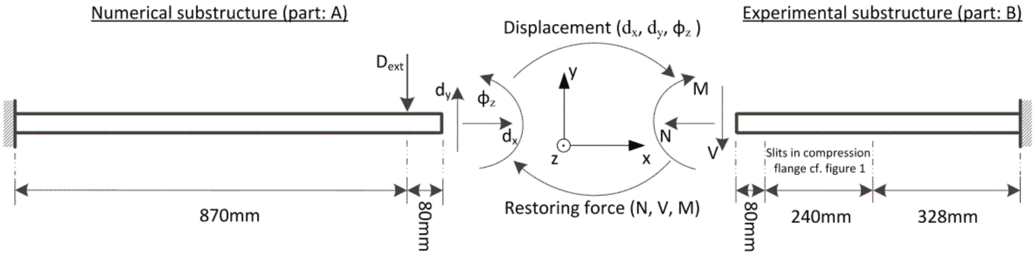
Numerical substructure (part: A)
Displacement (d_x, d_y, ϕ_z)
Experimental substructure (part: B)
D_ext
d_y
ϕ_z
d_x
y
z
x
M
N
V
Slits in compression flange cf. figure 1
870mm
80mm
Restoring force (N, V, M)
80mm
240mm
328mm

Fig. 21 The emulated structure tested in the hybrid simulation including division in numerical substructure and experimental substructure (Høgh, et al., 2015). The figure presents the shared boundary and the actions transferred, including x,y,z orientation

Hybrid Simulation Program Architecture

The architecture of the hybrid simulation program was redesigned from the state machine to a modified producer consumer loop, cf. Fig. 22. The previous architecture (Waldbjørn, et al., 2013) was not capable of running more than one process at a time meaning that real-time was not possible. In the new architecture the processes ran in two loops denominated Finite element model- and Experimental loop and the processes and data communication in each of these are outlined in Fig. 22. The program starts executing the Finite element model loop by calculating the displacements in the shared boundary by in the FEM. Hereafter the actions $[d_x\ d_y\ \varphi_z]$ are transformed into displacements in the actuators, and a trigger is sent to the controller to start applying the displacements. Simultaneously the program reads the forces in the actuators and transforms them into the restoring section forces, reads the displacements by DIC and the FEM model starts running for the next time step, while the actuator is still applying the previous displacements. In order to accommodate for the communication delay, cf. the experiment being one time step behind the finite element model, a compensator was implemented. The compensator extrapolated the subsequent restoring force by a linear or polynomial algorithm using the previous three or four points.

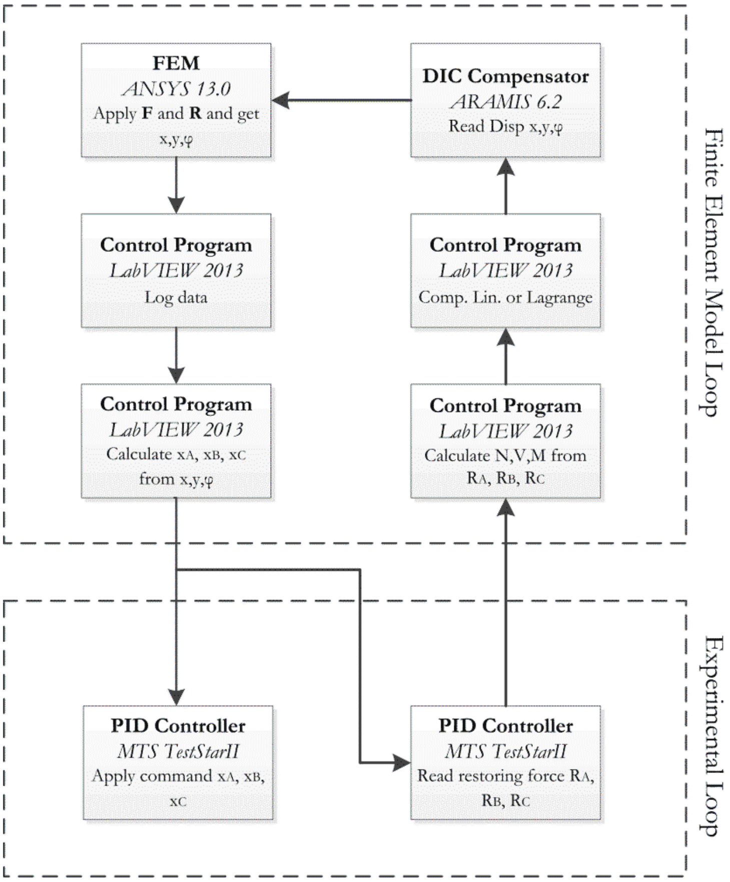
FEM
ANSYS 13.0
Apply F and R and get x,y,φ
DIC Compensator
ARAMIS 6.2
Read Disp x,y,φ
Control Program
LabVIEW 2013
Log data
Control Program
LabVIEW 2013
Comp. Lin. or Lagrange
Control Program
LabVIEW 2013
Calculate xA, xB, xC from x,y,φ
Control Program
LabVIEW 2013
Calculate N,V,M from RA, RB, RC
Finite Element Model Loop
PID Controller
MTS TestStarII
Apply command xA, xB, xC
PID Controller
MTS TestStarII
Read restoring force RA, RB, RC
Experimental Loop

Fig. 22 The double loop structure of the hybrid simulation program i.e. finite element loop and experimental loop

Results

Due to the long calculation time in ANSYS it was not possible to run a real-time hybrid simulation with the given setup. The test was therefore only run for quasi-static testing. For the same reason no compensator was implemented for transfer system delay i.e. time delay between command signal sent until applied by the actuator. The hybrid simulation was evaluated by comparing the overall displacement of the structure in the reference test and in the hybrid simulation, cf. Fig. 23. It is seen that the hybrid simulation was not able to get the correct displacement of the composite beam without the compensation due to the compliance of the load train. Especially in the shared boundary between the numerical and experimental substructure a big gap was seen.

The communication delay compensator was tested and found to have limited success. The linear compensator was able to account for the lack of stiffness due to communication delay but unfortunately it went unstable when changing sign on the loading. The third and fourth order polynomial compensator was not capable of running due to instability and it was therefore not documented in the publication.

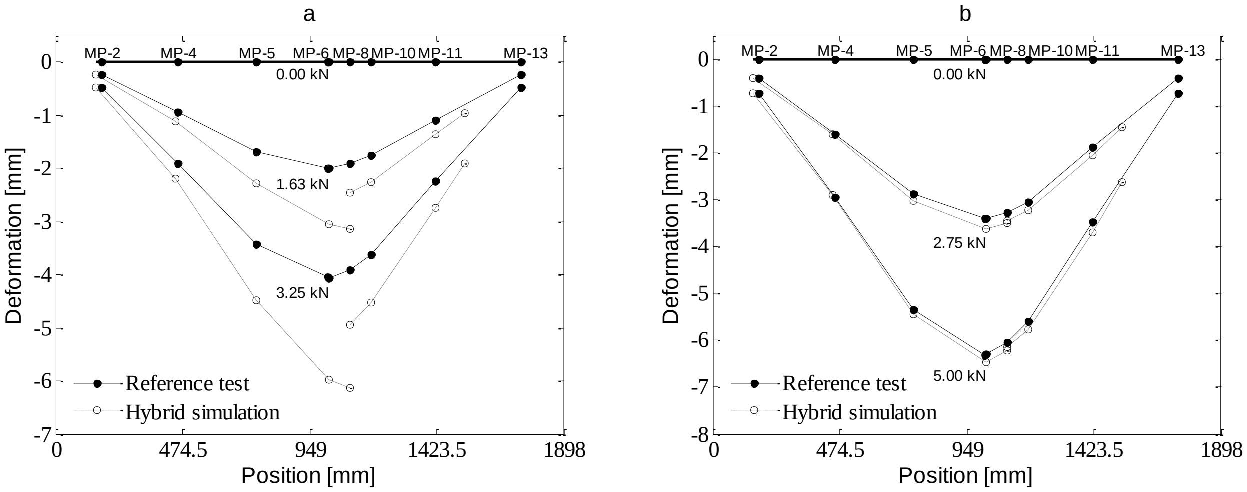

Fig. 23 Comparison of the overall displacement of the composite beam in the hybrid simulation and in the reference test a) shows the displacements with no DIC compensation b) the displacements with DIC compensator and restoring force prediction, cf. communication delay (Høgh, et al., 2015)

Conclusion

During the study a hybrid simulation program was designed for future real-time applications. The program was not able to run in real-time due to slow calculation times of the commercial finite element code ANSYS. However, a quasi-static hybrid simulation was still performed on a Single-component structure with DIC compensation and communication delay compensation. The hybrid simulation proved valid when comparing to a reference test performed on the entire emulated structure.

Hybrid Simulation of D-string Stiffened Wind Turbine Blade

J. Høgh, S. Gunay, K. M. Mosalam, *to be submitted*

Background and Objective

The objective of this study was to utilize hybrid simulation for a composite structure i.e. a 34m wind turbine blade retrofitted with a D-string stiffener polymer rope in order to limit opening of the trailing edge panels possibly causing trailing edge fracture, cf. Fig. 24. The D-string stiffeners are suggested to install at several location along the length of the wind turbine blade but for simplicity only one is tested in the hybrid simulations.

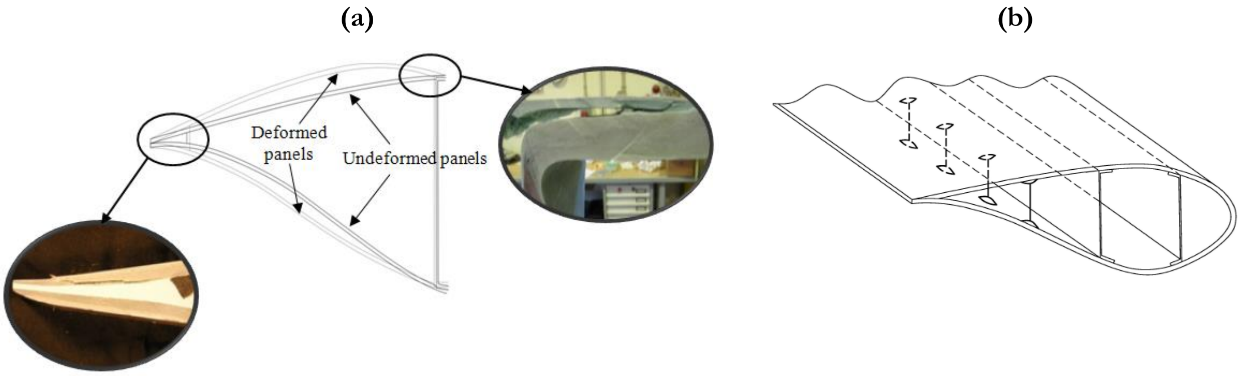

Fig. 24 (a) Crack initiation in trailing edge connection and connection between box girder and aerofoil as presented by Bladena A/S (Bladena A/S, 2015) (b) the position of the D-string stiffeners in the trailing edge panels

Emulated structure and Partitioning in Numerical and Experimental Substructure

A pseudodynamic test was performed using Openfresco for hybrid simulation handling and OpenSees for solution of time integration schemes. The numerical substructure was the 34m SSP glass fiber reinforced polymer wind turbine blade modelled using shell elements and orthotropic material properties.

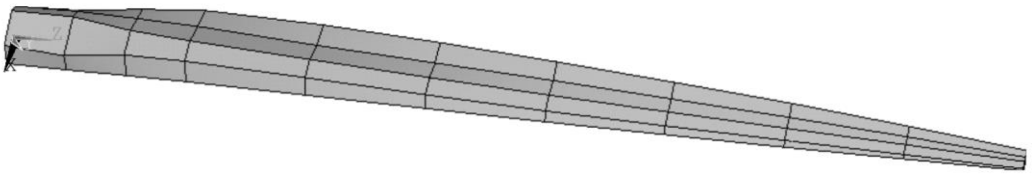

Fig. 25 The finite element model of the 34m SSP wind turbine blade (Høgh, et al., 2016)

Hybrid simulation setup

The pseudodynamic hybrid simulation was utilized in the test due to the clear dynamic effects in the finite element model in the tested loading frequency while the much stiffer D-string experienced the test as being static. The equation of motion eq. was solved using time integration by the implicit average acceleration Newmark algorithm (Shing, et al., 1996) in the open source finite element code OpenSees (University of California, Berkeley, 2012). The communication with the controller was handled in the open source program OpenFresco (Schellenberg, et al., 2007).

$$\boldsymbol{M\ddot{u}} + \boldsymbol{C\dot{u}} + \boldsymbol{Ku} + \boldsymbol{R} = \boldsymbol{F} \tag{23}$$

Results

The efficiency of the D-string stiffener was evaluated by comparing the opening of the trailing edge panels for a test with loading at 0.713Hz with and without the D-string stiffener installed, cf. Fig. 26. It is clearly observed that the D-string decreases the opening of the panels furthermore the loading of the string indicates the D-string relives the trailing edge connection for load (Høgh, et al., 2016).

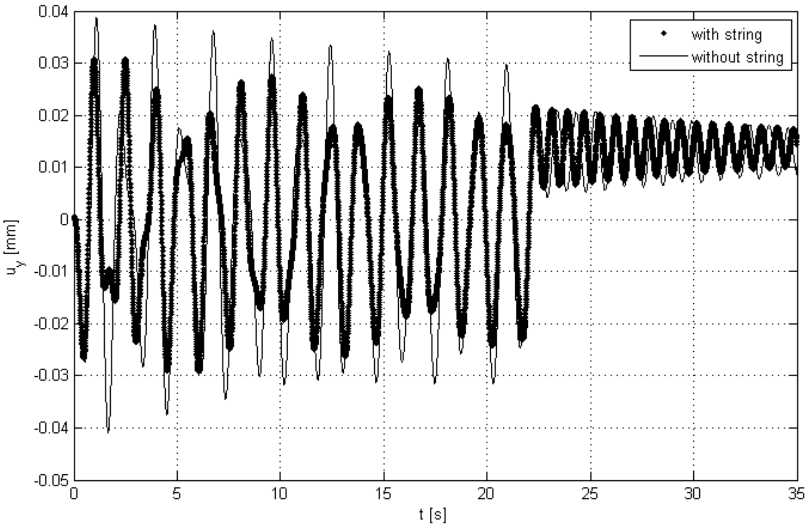

Fig. 26 Opening between trailing edge panels with and without D-string stiffener (Høgh, et al., 2016)

Conclusion

The pseudodynamic hybrid simulation indicated positive effects of the D-string stiffener in terms of decreasing the opening between the trailing edge panels. The displacement was decreased up to 75% cf. Fig. 26. However, due to the simplicity of the finite element model it cannot be concluded whether the positive effects are also present in the real application of the D-string stiffeners. Furthermore pronoun relaxation effects in the D-string stiffeners was observed which indicates the D-strings might lose tension over time which yields in loss of efficiency in decreasing opening of the trailing edge panels.

Compensation Methods in Real-Time Hybrid Simulation

J. Høgh, J. P. Waldbjørn, S. Andersen, C. Berggreen, *to be submitted*

Background and Objective

The objective of the study was to implement compensation for compliance and inertia force of a load train in a hybrid simulation. A DIC compensator had previously been implemented for quasi-static simulations but it the DIC software had a limitation maximum of 7Hz for real-time measurements. It was therefore necessary to reprogram the DIC control in a newer version of the software in order to achieve higher real-time displacement measurements e.g. 90Hz. Furthermore it was desired to test the compensators on a Single-component structure. Emphasis was put on having non-linear response of the numerical substructure so the compensators' and program's stability could be tested for this situation.

Test setup

The structure emulated in the hybrid simulation was a composite box girder clamped in one end and free in the other, cf. Fig. 27. The experimental substructure has two holes in the shear webs in order to initiate large deflections leading to non-linear stiffness response in the test. It can thereby be tested if the program is unstable in the case of non-linear experiment, as is the case for most applications of hybrid simulations. As done earlier, a reference test of the entire beam was performed in order to validate the setup.

The hybrid simulation was run in a LabVIEW program developed in (Waldbjørn, et al., 2016) and the load train compensators are include in the program in (Høgh, et al., 2016) were the overall architecture of the program is outlined in a flowchart.. The full experimental setup is presented in Fig. 28.

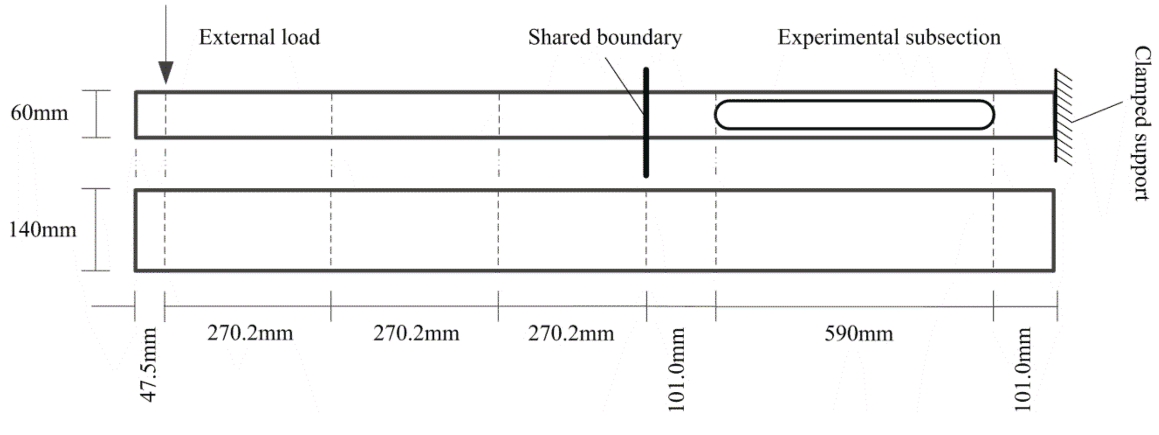

Fig. 27 The emulated structure tested in the hybrid simulation (Høgh, et al., 2016)

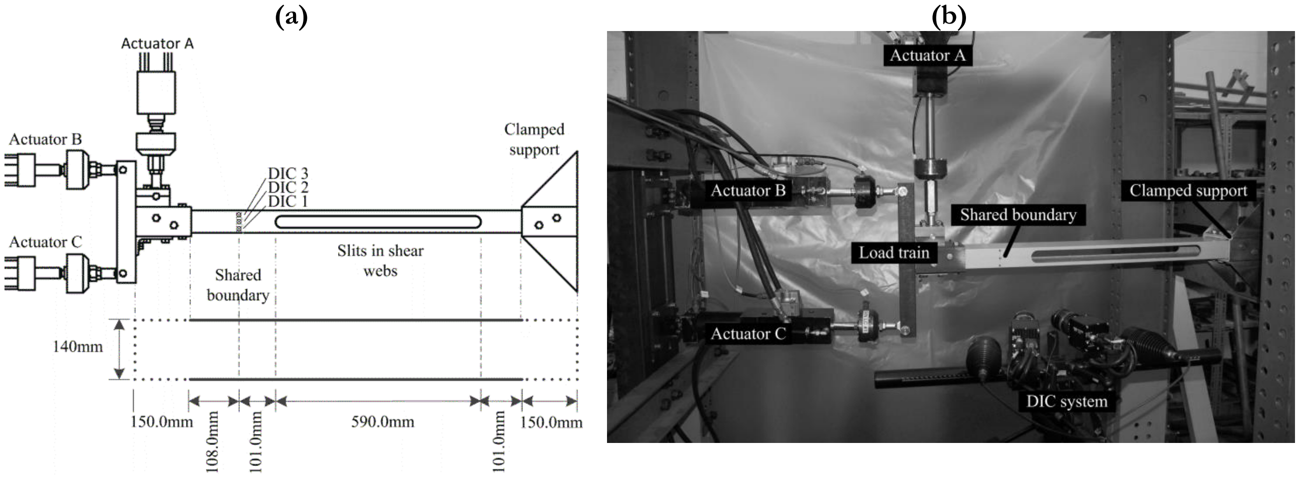
(a)
(b)
Actuator A
Actuator B
Actuator C
Clamped support
DIC 3
DIC 2
DIC 1
Slits in shear webs
Shared boundary
140mm
150.0mm
108.0mm
101.0mm
590.0mm
101.0mm
150.0mm
Actuator A
Actuator B
Clamped support
Shared boundary
Load train
Actuator C
DIC system

Fig. 28 The experimental substructure tested in the hybrid simulation. Figure (a) presents a sketch of the setup and (b) is a photograph of the same setup where the position of the DIC system is presented (Høgh, et al., 2016)

Compensation for Load Train Compliance and Inertia

The main focus of the paper was to implement two compensators handling errors initiated by the load train, cf. Fig. 28. The first issue with the load train was the compliance leading to errors in the shared boundary displacements, cf. Fig. 23a). This was done using the DIC compensator which used and PONTOS Live vs. 8 by GOM to acquire images and calculate displacements and then transfer them to the hybrid simulation code and correct the displacement in a proportional gain outer loop, cf. eq. (24) and eq. (25). In the approach the displacement vector $\mathbf{D}$ contains the displacements and rotation in the shared boundary measured by DIC, $\mathbf{D} = [u_x\ u_y\ \varphi_z]$. The error from the previous time step $\mathbf{e}(n\text{-}1)$ is multiplied by a gain vector $\boldsymbol{K}_{DIC}$ and added to the following time step in order to correct for the error. The *P*-gain approach is used in order to account for noise initiated by too fast correction.

$$\boldsymbol{D}_c(n) = \boldsymbol{K}_{DIC}\boldsymbol{e}(n-1) + \boldsymbol{D}_{c0}(n) \tag{24}$$

$$\boldsymbol{e}(n-1) = \boldsymbol{D}_c(n-1) - \boldsymbol{D}_{DIC}(n-1) \tag{25}$$

The inertia force compensator was utilized due to the large mass of the load train i.e. m = 25.68kg compared to the specimen approximately 5.6kg. From the reference test of the entire emulated structure the force needed to oscillate the box girder is known for 5 different frequencies. This is compared to the force needed to oscillate the load train without a specimen in, cf. Fig. 29. It is clearly seen that the force to excite the load train is considerable compared to the force to excite the specimen, cf. at 2.2Hz the forces are equal. This necessitates for an inertia force compensator as presented in eq. (26). The inertia compensator uses the mass and the displacement command to determine the acceleration of the load train.

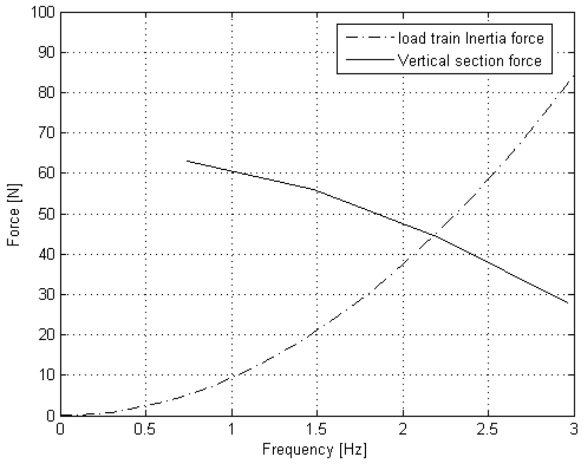

Fig. 29 The force in the actuators for different frequencies at a amplitude of 9.25mm compared to the inertia force of the load train (Høgh, et al., 2016)

$$F(t) = m\frac{d^2x}{dt^2} \cong m\frac{\Delta^2 x}{\Delta t^2} = m\frac{x_2 - 2x_1 + x_0}{\Delta t^2} \tag{26}$$

Results

The DIC compensator was evaluated by comparing the displacements and rotation at the shared boundary for the commanded and feedback displacements. In Fig. 30 the effect of DIC compensator is clearly seen when comparing the command and feedback for without (a) and (b) with DIC compensator. In the publication (Høgh, et al., 2016) the u_x, u_y displacements and the φ_z rotation, but here only the rotation results are included for simplicity. The error between the command and feedback is evaluated for all frequencies in Table 6. The u_x displacement is slowly improving for higher frequencies while the u_y and φ_z is decreasing more rapidly for higher frequencies.

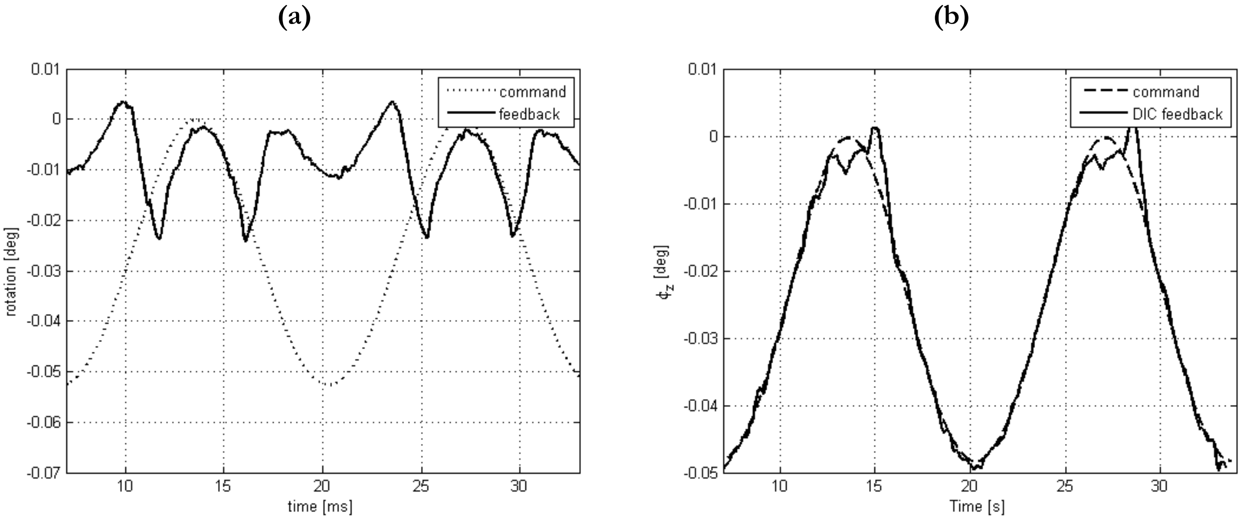

Fig. 30 The command versus feedback displacement in the shared boundary (a) no DIC compensation (b) With DIC compensation for a loading frequency of 0.074Hz (Høgh, et al., 2016)

Table 6 The standard deviation of error between the command and feedback displacements and rotations in the shared boundary for the 5 tested frequencies. The last row displays the maximum amplitude of signal for comparison of the error (Høgh, et al., 2016)

Frequency [Hz]	SD u_x [mm]	SD d_y [mm]	SD φ_z [deg]
0.074	0.2368	0.9339	0.0204
0.74	0.2313	1.4847	0.0203
1.48	0.2139	1.7797	0.0207
2.22	0.2175	4.7717	0.0234
2.96	0.1965	5.8946	0.0249
Amplitude of command signal	0.4626	24.0869	0.0526

The inertia force compensator was increasing the force applied by the actuators and the effects were evaluated for each frequency in terms of the applied force with and without the compensator, cf. Table 7. It is seen that the inertia force compensator is crucial to reading the correct restoring force from the controller.

Table 7 Maximum force applied for each frequency with and without the inertia force compensator activated. The ratio between the two is listed in the last column (Høgh, et al., 2016)

Frequency [Hz]	**Force Amplitude No Inertia Compensation [N]**	**Force Amplitude Inertia Compensation [N]**	**Uncompensated force as ratio of compensated force [%]**
0.074	40.1	40.9	98.1
0.74	42.3	49.0	86.4
1.48	41.0	69.3	59.1
2.22	39.5	107.1	36.9
2.96	28.8	150.1	19.2

Conclusion

The DIC and inertia force compensators were implemented in a real-time hybrid simulation program tested on a Single-component structure. The DIC compensator proved valid for improving the displacements for all tested frequencies. However the efficiency of the DIC compensator decreased as function of frequency due to the communication delay between the DIC measuring system and the hybrid simulation program. The inertia force compensator proved necessary for frequencies higher than 0.74Hz loading frequencies, however due to the error between the command and feedback displacement for higher frequencies the inertia force was also erroneous for these higher frequencies. Finally both compensators were utilized in the same test in order to improve the displacements used to calculate the inertia forces.

Conclusion

The benefits and challenges of performing hybrid simulation on composite structures with special focus on wind turbine blades were investigated and outlined. The concept of Single-component vs. Multi-component hybrid simulation was introduced as a distinct difference between hybrid simulation with a complex shared boundary to hybrid simulations with a simple. The control and measurement challenges in Single-component hybrid simulation were suggested to be solved by advanced control and monitoring techniques using DIC and FBG sensors for on-specimen measurements. However, other measurement techniques could be applied using the same control mechanisms if found more suited for the given setup. The measurements and control techniques were developed for usage in all hybrid simulation time scales even though only tested for quasi-static and real-time. During the studies Multi-component and Single-component hybrid simulations were performed. The Multi-component tests were found suited for testing of retrofitted elements with simple boundaries between the numerical and physical substructure, as was the case with the D-string stiffener. However, the studies also showed the complications of performing hybrid simulation of wind turbine blades in terms of the level of complexity of the FEM in order to get accurate results for a wind turbine blade. This indicates that real-time hybrid simulation of wind turbine blades needs comprehensive finite element models, and such models needs a commercial code with an advanced pre-processor or else they will be too comprehensive to construct. This again requires comprehensive computational resources. It is therefore suggested to focus on pseudodynamic hybrid simulation for wind turbine blades, since computational time is much less critical and this therefore puts much lower demands on the laboratory facilities. The Single-component hybrid simulations was suggested to be suited for large panels etc. in regions sensitive to buckling etc. where it would save the cost of a blade test of the entire structure. However, no such tests were conducted due to the complexity and the given state-of-the art of hybrid simulation in the given project.

List of Figures

Fig. 1 Typical application of hybrid simulation for earthquake engineering 1

Fig. 2 Local fractures in wind turbine blades (a) test by Bladena A/S (Bladena A/S, 2015) fracture in trailing edge and between shear web and spar cap (b) multiple local failure phenomena in trailing edge shear webs connections etc. (Lee & Park, 2016) (c) Local buckling phenomena in the compressive spar cap (Overgaard, et al., 2010) 3

Fig. 3 Examples of generic three-rotor offshore wind turbines (Krenk, 2010) similar to the ones studied in (Bladena A/S, 2015), (Lee & Park, 2016), (Overgaard, et al., 2010) 4

Fig. 4 The overall progress in the hybrid simulations performed during the research. The x-axis represents time/publications and the y-axis the complexity of each of the four evaluation parameters, being; Experiment, FEM, Compensation and Time Scale 5

Fig. 5 The key properties of the shared boundary in (a) Multi-component and (b) Single-component hybrid simulation 8

Fig. 6 Force relaxation in a ramp and hold compared to a continues loading approach cf. (Carrion & Spencer Jr., 2007) 10

Fig. 7 Generic quasi-static or pseudodynamic hybrid simulation communication flow chart. The flow chart is from (Høgh, et al., 2015) but slightly modified so the processes are generic 11

Fig. 8 Example of a generic real-time hybrid simulation program 12

Fig. 9 Example of (a) interpolation between known displacement points and (b) extrapolation of the command signal in order to get command signal to the actuators, cf. (Shing, 2008) 15

Fig. 10 Schematic illustration of the FBG concept (Høgh, et al., 2015) 17

Fig. 11 Three-axial test setup for testing in-plane cf. (Høgh, et al., 2016) 19

Fig. 12 Moment and normal force diagram (MN-diagram) for the test setup, the shear force capacity is independent of the moment and normal force applied 20

Fig. 13 The load train of the three axial load train, cf. (Høgh, et al., 2015) 22

Fig. 14 The force as function of acceleration in the vibration test 23

Fig. 15 Data flow of communication in FBG and DIC compensation program, cf. (Waldbjørn, et al., 2013) 27

Fig. 16 Test sequence for the FBG controlled test A) the strain command vs DIC feedback B) the outer loop correction by FBG to an accuracy of 20μm/m, cf. (Waldbjørn, et al., 2013) 27

Fig. 17 Test sequence for the DIC controlled test A) the displacement command vs DIC feedback B) the outer loop correction by DIC to an accuracy of 0.01mm, cf. (Waldbjørn, et al., 2013) 28

Fig. 18 Structure emulated in the hybrid simulation was a frame structure, part A is the numerical component and part B the experimental (Waldbjørn, et al., 2013) 29

Fig. 19 The structure of the LabVIEW state machine hybrid simulation program where the data flow is divided into 5 sub processes. Each process is headlined with the overall process, the software/hardware used and explanatory text of action performed. 30

Fig. 20 The comparison of the hybrid simulation to the full FEM of the emulated structure and the analytical simulation of the hybrid simulation (Waldbjørn, et al., 2013) 31

Fig. 21 The emulated structure tested in the hybrid simulation including division in numerical substructure and experimental substructure (Høgh, et al., 2015). The figure presents the shared boundary and the actions transferred, including x,y,z orientation 32

Fig. 22 The double loop structure of the hybrid simulation program i.e. finite element loop and experimental loop 33

Fig. 23 Comparison of the overall displacement of the composite beam in the hybrid simulation and in the reference test a) shows the displacements with no DIC compensation b) the displacements with DIC compensator and restoring force prediction, cf. communication delay (Høgh, et al., 2015) 34

Fig. 24 (a) Crack initiation in trailing edge connection and connection between box girder and aerofoil as presented by Bladena A/S (Bladena A/S, 2015) (b) the position of the D-string stiffeners in the trailing edge panels 35

Fig. 25 The finite element model of the 34m SSP wind turbine blade (Høgh, et al., 2016) 35

Fig. 26 Opening between trailing edge panels with and without D-string stiffener (Høgh, et al., 2016) 36
Fig. 27 The emulated structure tested in the hybrid simulation (Høgh, et al., 2016) 37
Fig. 28 The experimental substructure tested in the hybrid simulation. Figure (a) presents a sketch of the setup and (b) is a photograph of the same setup where the position of the DIC system is presented (Høgh, et al., 2016) 38
Fig. 29 The force in the actuators for different frequencies at a amplitude of 9.25mm compared to the inertia force of the load train (Høgh, et al., 2016) 39
Fig. 30 The command versus feedback displacement in the shared boundary (a) no DIC compensation (b) With DIC compensation for a loading frequency of 0.074Hz (Høgh, et al., 2016) 39

References

Ahmadizadeh, M., Mosqueda, G. & Reinhorn, A. M., 2008. Compensation of actuator delay and dynamics for real-time hybrid simulation. *Earthquake Engineering and Structural Dynamics,* Volume 37, pp. 21-42.

Bitter, R., Mohiuddin, T. & Nawrokki, M., 2007. *LabVIEW: Advanced Programming Techniques, 2nd Edition.* s.l.:CRC Press.

Bladena A/S, 2015. *Bladena.* [Online]
Available at: http://www.bladena.com/abe/Publications.aspx
[Accessed 1 12 2015].

Bonnet, P. A., Williams, M. S. & Blakeborough, A., 2007. *Compensation of actuator dynamics in real-time hybrid tests.* Oxford, Proceedings of the Institution of Mechanical Engineers Part I Journal of Systems and Control Engineering, pp. 251-264.

Bonnet, P. A., Williams, M. S. & Blakeborough, A., 2008. Evaluation of numerical time-integration schemes for real-time hybrid testing. *Earthquake Engineering and Structural Dynamics,* Volume 37, pp. 1467-1490.

Bunsell, A. R. & Renard, J., 2005. *Fundamentals of fibre reinforced composite materials.* Cornwall, UK: IOP Publishing Ltd.

Carrion, J. E. & Spencer Jr., B. F., 2007. *Model-based Strategies for Real-time Hybrid Testing,* Urbana-Champaign, Illinois, USA: Newmark Structural Engineering Laboratory (NSEL).

Chan, T. H. et al., 2006. Fiber Bragg grating sensors for structural health monitoring of Tsing Ma bridge: Background and experimental observation. *Engineering Structures,* Volume 28, pp. 648-659.

Chen, C., Ricles, J. M. & Guo, T., 2012. Improved Adaptive Inverse Compensation Technique for Real-Time Hybrid Simulatino. *Journal of Engineering Mechanics,* 138(12), pp. 1432-1446.

Cheng, C. & Ricles, J. M., 2008. Development of Direct Integration Algorithms for Structural Dynamics Using Discrete Control Theory. *Journal of Engineering Mechanics,* 134(8), pp. 676-683.

Chen, P.-C. & Tsai, K.-C., 2013. Dual compensation strategy for real-time hybrid testing. *Earthquake Engineering and Structural Dynamics,* 42(1), pp. 1-23.

Chen, Z. et al., 2014. Equivalent force control method for substructure pseudo-dynamic test of a full-scale masonry structure. *Earthquake Engineering & Structural Dynamics,* Volume 43, pp. 969-983.

Chung, J. & Hulbert, G. M., 1993. A Time Integration Algorithm for Structural Dynamics with Improved Numerical Dissipation: The Generalized-alpha Method. *Journal of Applied Mechanics,* Volume 60, pp. 371-375.

Cook, R. D., 1995. *Finite element modeling for stress analysis.* Madison, USA: John Wiley & Sons, Inc.

Eder, M. A., Bitsche, R. D., Nielsen, M. & Branner, K., 2014. A practical approach to fracture analysis at the trailing edge of a wind turbine rotor blade. *Wind energy,* Volume 17, pp. 483-497.

Elkhoraibi, T. & Mosalam, K. M., 2007. Towards error-free hybrid simulation using mixed variables. *Earthquake Engineering and Structural Dynamcis,* 36(11), pp. 1497-1522.

Ellis, G., 2000. *Control System Design Guide.* San Diego, California, USA: Academic Press.

Facchinetti, A. & Bruni, S., 2012. Hardware-in-the-loop hybrid simulation of pantograph-catenary interaction. *Journal of Sound and Vibration,* Volume 2783-2797, p. 331.

Fayolle, X., Calloch, S. & Hild, F., 2007. Controlling testing machines with digital image correlation. *Experimental techniques,* 31(3), pp. 57-63.

GOM, 2006. *ARAMIS - User Manual - Software.* Braunschweig, Germany: GOM.

GOM, 2006. *The GOM Scripting Language.* Braunschweig, Germany: GOM.

Hansen, M. H., 2004. Aeroelastic Stability Analysis of Wind Turbines Using an Eigenvalue Approach. *Wind Energy,* Volume 7, pp. 133-143.

Horuichi, T., Inoue, M., Konno, T. & Namita, Y., 1999. Real-time hybrid experimental system with actuator delay compensation and its application to a piping system with energy absorber. *Earthquake Engineering and Structural Dynamics,* 28(10), pp. 1121-1141.

Hughes, T. J., Pister, K. S. & Taylor, R. L., 1979. Implicit-explicit finite elements in non-linear transient analysis. *Computer Methods in Applied Mechanics and Engineering (Part 1),* pp. 159-182.

Høgh, J. H., Gunay, S. & Mosalam, K., 2016. Hybrid Simulation of a D-string Stiffened Wind Turbine Blade. *To be Submitted.*

Høgh, J., Waldbjørn, J., Andersen, S. & Berggreen, C., 2016. Compensation Methods in Real-time Hybrid Simulation. *To be submitted.*

Høgh, J. et al., 2015. Quasi-static single-component hybrid simulation of a composite structure with multi-axis control. *Strain,* Volume 51, pp. 459-473.

Ibsen Photonics, 2009. *I-MON E-USB 2.0 Product Specification.* Farum, Denmark: Ibsen Photonics A/S.

Inman, D. J., 2001. *Engineering Vibrations.* s.l.:Prentice Hall.

Jacobsen, A., Hitaka, T. & Nakashima, M., 2010. Online test of building frame with slit-wall dampers capable of condition assement. *Journal of Constructional Steel Research,* 66(11), pp. 1320-1329.

Jensen, F. M., Falzon, B. G., Ankersen, J. & Stang, H., 2006. Structural testing and numerical simulation of a 34m composite wind turbine blade. *Composite Structures,* Volume 76, pp. 52-61.

Jensen, M. F., 2008. *Ultimate strength of a large wind turbine blade, PhD dissertation,* Roskilde & Kgs. Lyngby, Denmark: Risø National Laboratory for Sustainable Energy & Department of Civil Engineering, Technical University of Denmark.

Krenk, S., 2010. Free Vibrations. In: *Dynamics of Structures: Theory and Analysis, Department of Mechanical Engineering, Technical University of Denmark.* s.l.:s.n.

Kreuzer, M., n.d. *Strain Measurement with Fiber Bragg Grating Sensors.* Darmstadt, Germany: HBM.

Lee, H. G. & Park, J., 2016. Static test until structural collapse after fatigue testing of a full-scale wind turbine blade. *Composite Structures,* Volume 136, pp. 251-257.

Lin, Y. Z. & Christenson, R. E., 2009. Comparison of Real-time Hybrid Testing with Shake Table Test for an MR Damper Controlled Structure. *American Control Conference,* pp. 5228-5233.

Maghareh, A., Dyke, S. J., Prakash, A. & Bunting, G. B., 2014. Establising a predictive performance indicator for real-time hybrid simulation. *Earthquake Engineering & Structural Dynamics,* Volume 43, pp. 2299-2318.

Material Testing Systems, MTS, 2015. *MTS.* [Online]
Available at: https://www.mts.com/en/products/producttype/test-components/controllers/flextest-controllers/index.htm
[Accessed 20 6 2015].

Mercan, O. & Ricles, J. M., 2008. Stability analysis for real-time pseudodynamic and hybrid pseudodynamic testing with multiple sources of delay. *Earthquake Engineering and Structural Dynamics,* Volume 37, pp. 1269-1293.

MTS, 2009. *LabVIEW Programming Libraries: Model 793.00 Software.* s.l.:MTS Systems Corporation.

Nakashima, M. & Masaoka, N., 1999. Real-Time On-Line Test for MDOF Systems. *Earthquake Engineering and Structural Dynamics,* Volume 28, pp. 393-420.

Newmark, N. M., 1959. Method for Computation for Structural Dynamics. *ASCE Journal of Engineering, Mechanical Division,* Volume 85, pp. 67-94.

Nielsen, M. W. et al., 2013. Life cycle strain monitoring in glass fibre reinforced polymer laminates using embedded fibre Bragg grating sensors from manufactoring to failure. *Journal of Composite Materials,* Volume 0, pp. 1-17.

Overgaard, L. C., Lund, E. & Thomsen, O. T., 2010. Structural collapse of a wind turbine blade. Part A: static test and equivalent single layered models. *Composites: Part A,* Volume 41, pp. 257-270.

Pan, P. et al., 2006. Development of Peer-to-Peer (P2P) Internet Online Hybrid Test System. *Earthquake Engineering and Structural Dynamics,* 35(7), pp. 867-890.

Phillips, B. M. & Spencer, B. F., 2011. *Model-based servo-hydraulic control for real-time hybrid simulation,* Urbana-Champaign, Illinois, USA: Newmark Structural Engineering Laboratory.

Pinto, A. V., Pegon, P., Magonette, G. & Tsionis, G., 2004. Pseudo-dynamic testing of bridges using non-linear substructuring. *Earthquake Engineering and Structural Dynamics,* Volume 33, pp. 1125-1146.

Saouma, V. & Sivaselvan, M., 2008. *Hybrid Simulation - Theory, Implementation and Applications.* London, UK: Taylor & Francis.

Schellenberg, A., Mahin, S. A. & Fenves, G. L., 2007. *A software framework for hybrid simulation of large structural systems.* Long Beach, CA, USA, Proceedings of the ASCE Structures Congress, pp. 1-16.

Schubel, P. J. & Crossley, R. J., 2012. Wind Turbine Blade Design. *Energies,* Volume 5, pp. 3425-3449.

Shing, P. B., 2008. Integration schemes for real-time hybrid testing. In: *Hybrid Simulation - Theory, Implementation and Applications.* London, UK: Taylor and Francis, pp. 25-34.

Shing, P.-S. B. & Mahin, S., 1987. Cumulative experimental errors in pseudodynamic tests. *Earthquake Engineering and Structural Dynamics,* Volume 15, pp. 409-424.

Shing, P. B., Nakashima, M. & Bursi, S. O., 1996. Application of Pseudodynamic Test Method to Structural Research. *Earthquake Spectra,* 12(1).

Shing, P.-S. B., Vannan, M. T. & Carter, E. W., 1991. Implicit time integration for pseudodynamic tests. *Earthquake Engineering and Structural Dynamics,* Volume 20, pp. 551-576.

Spencer, B. F., Chang, C.-M., Frankie, T. M. & Kuchima, D. A., 2015. Multiple Degrees of Freedom Positioning Correction for Hybrid Simulation. *Journal of Earthquake Engineering,* 19(2), pp. 277-296.

Sutton, M. A., Orteu, J. J. & Schreier, H. W., 2009. *Image Correlation for Shape, Motion and Deformation Measurements.* New York, USA: Springer.

Sutton, M. A., Orteu, J.-J. & Schreier, H. W., 2009. *Image Correlation for shape, motion and deformation measurements.* s.l.:Springer.

Takanashi, K. & Nakashima, M., 1987. Japanese Activities on On-Line Testing. *Journal of Engineering Mechanics,* 113(7), pp. 1014-1032.

University of California, Berkeley, 2012. *OpenSees Wiki.* [Online]
Available at: http://opensees.berkeley.edu/wiki/index.php/Main_Page
[Accessed 30 1 2015].

Verma, M. & Rajasankar, J., 2012. Improved model for real-time substructuring testing system. *Engineering Structures,* Volume 41, pp. 258-269.

Waldbjørn, J. et al., 2016. Single-component Multi-rate Real Time Hybrid Simulation pilot test on a composite structure. *To be submitted.*

Waldbjørn, J. et al., 2013. *Hybrid Testing of Composite Structures with Single-axis Control.* Montreal, Canada, Proceedings of the 19th International Conference on Composite Materials, pp. 4094-4104.

Waldbjørn, J. et al., 2013. Strain and Deformation Control by Fibre Bragg Grating and Digital Image Correlation. *Strain.*

Waldbjørn, J. P. et al., 2016. Single-component Multi-rate Real Time Hybrid Simulation pilot test on a composite structure. *To be submitted.*

Williams, M. S., 2007. *Real-time hybrid testing in structural dynamics.* Brisbane, Australia, 5th Australasian Congress on Applied Mechanics, ACAM, pp. 2-11.

Wu, B., Bao, H., Ou, J. & Tian, S., 2005. Stability and accuracy analysis of the central difference method for real-time substructure testing. *Earthquake Engineering and Structural Dynamics,* Volume 34, pp. 705-718.

Wu, B., Xu, G., Wang, Q. & Williams, M., 2005. Operator-splitting method for real-time substructure testing. *Earthquake Engineering and Structureal Dynamics,* 35(3), pp. 293-314.

Zenkert, D., 1995. *Sandwich Construction.* Eastborne: CPI Antony Rowe.

Zenkert, D. & Battley, M., 2006. *Foundations of Fibe Composites.* Lyngby, Denmark: Technical University of Denmark.

Publications

50 YEARS of strain
strain
An International Journal for Experimental Mechanics

Strain and Displacement Controls by Fibre Bragg Grating and Digital Image Correlation

J. Waldbjørn*, J. Høgh†, J. Wittrup-Schmidt*, M. W. Nielsen‡, K. Branner§, H. Stang* and C. Berggreen†

*Department of Civil Engineering, Technical University of Denmark, Brovej Building 118, 2800, Kgs. Lyngby, Denmark
†Department of Mechanical Engineering, Technical University of Denmark, Nils Koppels Alle, Building 403, 2800, Kgs. Lyngby, Denmark
‡Department of Mechanical Engineering, Technical University of Denmark, Produktionstorvet Building 425, 2800, Kgs. Lyngby, Denmark
§Department of Wind Energy, Technical University of Denmark, Frederiksborgvej 399, 4000 Roskilde, Denmark

ABSTRACT: Test control is traditionally performed by a feedback signal from a displacement transducer or force gauge positioned inside the actuator of a test machine. For highly compliant test rigs, this is a problem since the response of the rig influences the results. It is therefore beneficial to control the test based on measurements performed directly on the test specimen. In this paper, fibre Bragg grating (FBG) and Digital Image Correlation (DIC) are used to control a test. The FBG sensors offer the possibility of measuring strains inside the specimen, while the DIC system measures strains and displacement on the surface of the specimen. In this paper, a three-point bending test is used to demonstrate the functionality of a control loop, where the FBG and DIC signals are used as control channels. The FBG strain control was capable of controlling the test within an error tolerance of 20 μm m^{-1}. However, the measurement uncertainty offered by the FBG system allowed a tolerance of 8.3 μm m^{-1}. The DIC displacement control proved capable of controlling the displacement within an accuracy of 0.01 mm.

KEY WORDS: *digital image correlation, displacement control, fibre Bragg grating, fibre reinforced plastic, three-point bending*

Introduction

Mechanical testing is commonly controlled by a proportional-integral-derivative (PID) controller using the feedback signal from a load cell or a gauge positioned in the actuator of the testing machine e.g. linear variable differential transducer (LVDT). However, the compliance of the load train will in this case affect the results, and it is therefore more accurate to control the test by measurements performed directly on the specimen e.g. by a clip gauge [1], where the strain from the gauge is fed into the PID control loop as an analogue signal. Other measurement techniques have also been used to control tests e.g. digital image correlation [2]. In these efforts, the signal from the external measurements has not been used in the PID controller, instead, an outer control loop was designed to correct the displacement/strain applied by the PID controller in the inner control loop. These methods might be useful when testing specimens with complex geometry and/or test rigs with joints and bearings. In such cases, the desired strain state is not easily obtained, since the displacement measured by the LVDT at the actuator is not the same as the displacement in the specimen, and it is therefore possible to obtain higher accuracy if measurements are performed directly on the specimen and feed into the control loop. The effect of the compliance of the load train is thereby omitted.

FBG sensors are gauges inside optical fibres capable of measuring strains by changes in a reflected light beam. Due to the small diameter and environmental robustness of the fibre optic sensor, it can be embedded into several types of materials e.g. laminated/sandwich composites and concrete, without affecting the mechanical properties [3] of the test specimen. This has made the FBG technology widespread within the field of mechanical engineering covering manufacturing techniques, material/component testing, structural health monitoring (SHM) and damage assessment and support control systems. By embedding/attaching FBG sensors to a structure during manufacturing, it is possible to monitor the process-induced temperature and residual strains as they develop [4–6]. Within material/component testing, the FBG sensor provides accurate and local measurement capabilities of internal stress distribution, stress concentrations and vibrations [7, 8]. Furthermore, FBG sensors can detect cracks and delamination, which are key information in glass fibre reinforced polymer (GFRP) testing [9, 10]. Also, in SHM, the FBG sensors are used for the observation of the in-service structural performance due to ageing and degradation caused by the environment. In this case, the sensors can be used to monitor the integrity of the structure [11–15]. The environmental robustness and high resolution of the FBG sensors enable high precision control suitable for systems in which geometry or harsh environmental conditions do not allow the use of other sensor technologies [16]. When performing tests where a certain strain state is difficult to obtain due to a complex test rig/geometry, it is beneficial to use FBG sensors for control, since they can measure strains directly on the specimen or even inside.

DIC is a technique capable of calculating strains and displacement on a surface on the basis of digital images. Within the field of mechanical and civil engineering, the DIC technology is widespread within multiple categories e.g. material characterization (Young's modulus, Poisson's

© 2014 Wiley Publishing Ltd

doi: 10.1111/str.12089

ratio, elasto-plastic behaviour, etc.), component testing, fracture mechanics and high speed testing for dynamic and high strain rate measurements. With the ability to identify both local and global strain distribution and perform measurements in the plastic regime, the DIC technology has proven to be a useful tool within material testing [17–20]. The DIC technique inherently has no limit of size, and it has been applied for varying length scales covering a few square millimetres up to multiple square metres [21–23]. In fracture mechanics, the DIC technique is able to deliver information about crack propagation, which can be used for the determination of important fracture mechanic parameters [24, 25]. The DIC technique has the ability of high rate image acquisition, which makes it suitable for dynamic measurements [26–28] or even blast tests where it has been used for image acquisition in the range of megahertz [29]. The DIC system is capable of delivering high resolution 3D full field measurements, which are easily integrated in the testing environment. When dealing with a complex specimen geometry and/or load train, the measurement technique represents a substitute to a large number of analogue gauges including extensometers, potentiometers and strain gauges. Thus, with the aim of performing real-time measurements from multiple positions on the test object surface, the DIC technique is implemented in this work for static displacement control.

This paper documents a series of three-point bending tests controlled by a feedback signal acquired from the test specimen by DIC and FBG measurements for displacement and strain controls, respectively. This is performed by a control loop that operates and acquires data from a test station, FBG interrogation system and DIC system. The displacement is applied by the test station using a servo-hydraulic actuator operated by a PID controller. The FBG measurements are obtained by emitting light through two optical fibres, each containing three FBG sensors. The optical fibres are embedded into the GFRP beams during manufacturing, one at the top and one at the bottom of the beam. The reflected light is analysed by an interrogator and converted to strain. The DIC measurements are performed by a stereoscopic camera system, capable of tracking the displacement of the specimen surface by image matching and photogrammetry. The experiments are performed within the linear elastic regime for five GFRP beams with a predefined error tolerance to document the functionality of the control loop.

Principle of Fibre Bragg Grating

An FBG is a short segment of several thousand organised layers with varying refractive indices written into a single mode fibre. When a broad band light beam strikes the interface between each layer in the FBG, the light is reflected and refracted cf. Fresnel equation [29]. When the grating period is equal to the wavelength, each single interface reflection is reflected in the phase magnifying the energy level by positive interference forming a narrow band spectral peak. The remaining reflected spectra are out of the phase with the grating period and therefore erased. By straining the FBG, a shift of the peak reflectivity is generated as illustrated in Figure 1, which is convertible to multiple physical quantities including strain, temperature and vibrations. [30].

Knowing the initial wavelength λ_0, the wavelength change $\Delta\lambda$ and the temperature change ΔT of the specimen, the strain is calculated from Equation (1).

$$\frac{\Delta\lambda}{\lambda_0} = \varepsilon k_\varepsilon + k_t \Delta \mathrm{T} \tag{1}$$

where the gauge factors k_ε and k_t are provided by the FBG manufacturer. The identification of the narrow band light reflected by the FBG is performed by an interrogation monitor, which converts the incident light to an array of discrete digital intensity data.

Principal of Digital Image Correlation

The DIC technique is a non-contact, full field measurement method based on grey-value digital images [31]. The system has two imaging sensors tracking the shape, motion and displacement of an object surface in three dimensions [27]. Figure 2 illustrates a DIC setup with a commercial system, capable of acquiring images of the specimen surface, which are subsequently analysed by the DIC software, [32].

DIC utilise two techniques to acquire data: image matching and photogrammetry [31]. Image matching identifies the position of each measurement point in the two camera images. This is done by dividing the first camera image into squared facets containing multiple pixels. For each facet, a suitable transformation matching the homologous area in the second camera image is derived tracking each successive image with sub-pixel accuracy. The surface must have a stochastic speckle pattern in order

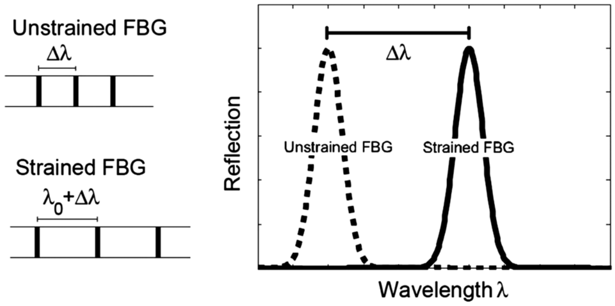

Figure 1: The change in peak reflectivity as a function of the grating period

© 2014 Wiley Publishing Ltd
doi: 10.1111/str.12089

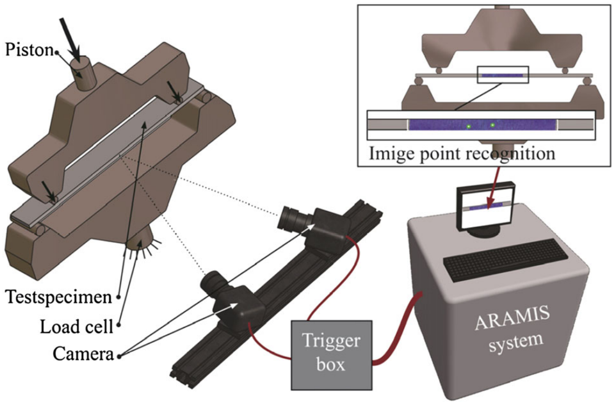

Figure 2: A four-point bending test with the commercial DIC system; ARAMIS

for the facets to be uniquely identifiable. Photogrammetry performs a transformation between the geometric properties of the measurement surface in the photographic image. This technique relies on a calibration to determine the imaging parameters for each camera (intrinsic) and the relative position and orientation of the cameras with respect to each other (extrinsic) [32]. The outcome is a 3D full field component shape and surface displacement field, along with the components of a plane strain tensor.

Test Setup

The test specimen is loaded in a four-column MTS 810 test machine with a T-slot strong table and an axial servo-hydraulic actuator with a static stroke of ±33.00 mm. The servo-hydraulic actuator is an MTS model 244.22 with a load capacity of 100 kN. The oil flow through the actuator is controlled by an MTS servo valve, model 252.24C-04 with a capacity of 38 L min^{-1}. Two feedback transducers are mounted in conjunction with the actuator: an internal LVDT and a load cell model MTS 661.19E-04 with a capacity of 25 kN. The actuator is operated, and the transducer signal is acquired by an MTS FlexTest60 PID controller. The loading nose and support rollers are 40 and 25 mm in diameter, respectively, cf. Figure 3, and the support rollers are able to move horizontally. Electrical resistance strain gauges are mounted on the specimens of the type SR-4 general purpose strain gauges from Vishay Micro-Measurements. The gauge resistance is 120.0Ω ± 0.3% and gauge length 6.99 mm for all specimens, while the gauge factor is 2.075 ± 0.5% for beams 1 and 3 and 2.035 ± 0.5% for the remaining. The optical fibres embedded in the specimens are silica fibres provided by FOS&S. Each fibre contains three draw tower gratings (FBG sensors) with a gauge length of 4.00 mm and an Ormocer coating (cladding diameter of 125 μm). The sensitivity coefficients k_ε and k_T are equal to 7.75E-7 μm m^{-1} and 6.27E-6 K^{-1}, respectively. The signal is acquired by a stand-alone interrogator type: I-MON 512 E-USB with a wavelength range of 1510–1595 nm cf. [33]. The surface is painted with a stochastic black speckle pattern on a white background, and three measurements points (MP) are selected, cf. Figure 3. The displacement of the measurement points is tracked by the commercial DIC system of the type ARAMIS from the company Geseltshaft für Optische Messtechnik (GOM). The camera resolution is 4 megapixels (2352 × 1728 pixels) with 20 mm focal length Titanar lenses. The images are divided into facets of 15 × 15 pixels, with a shift of 13 pixels. The cameras were calibrated to an intersection deviation of 0.024 pixels, with a 250 × 200 mm ARAMIS calibration panel to obtain a measurement area of 330 mm width and 330 mm height. The accuracy of the DIC setup is evaluated by a micrometre of the type: Mitutoyo — series 164 and range 0–50 mm. The micrometre offers an accuracy and resolution

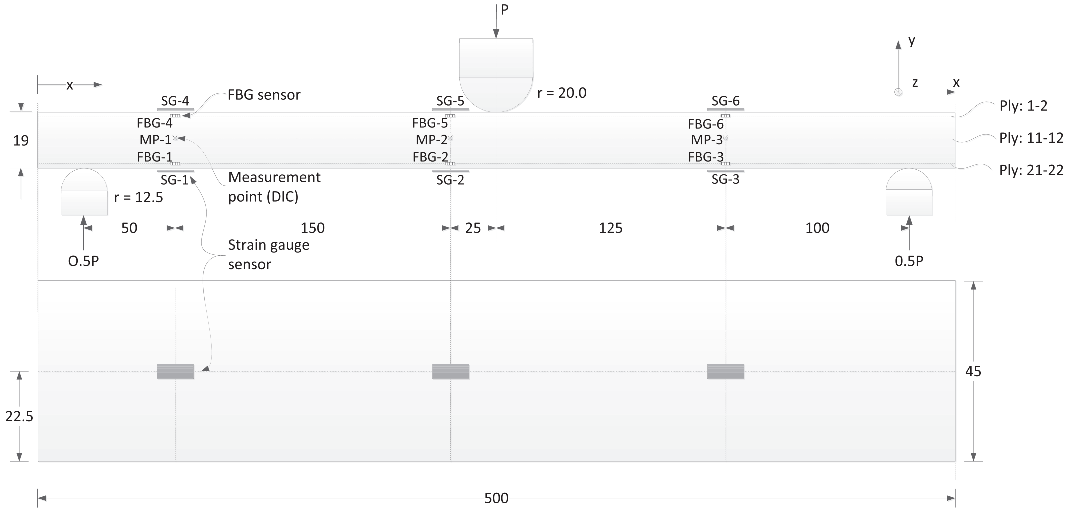

Figure 3: Dimensions of the test setup and specimen along with numbering and location of various sensors

doi: 10.1111/str.12089

of 3 μm and ±1 μm, respectively, and is mounted to a linear motion system type: THK-RSR7W. The dimensions of the three-point bending setup and test specimen along with numbering of the FBG sensors, electrical resistance strain gauges and the DIC measurement points (MPs) are displayed in Figure 3.

The entire test setup, with the specimen inserted into the three-point bending rig with the mounted gauges, is presented in Figure 4.

Specimen properties

The test specimen is a GFRP beam with 22 plies of unidirectional (UD) fibre mats of the type L1200/G50F-E06-A, from Devold AMT, with a nominal area weight of 1246 g m^{-2}. The matrix is a thermoset epoxy resin of the type Airstone 760E mixed with Airstone 776H hardener, from Dow Chemicals Company. Five GFRP beams were produced by vacuum infusion with a fibre orientation in the *x*-direction (see Figure 3) and fibre volume fraction of 55% [34]. The stiffness and strength properties of the beams are calculated by the rule-of-mixture on the basis of UD mechanical properties listed in Table 1 [35].

The load capacity at first ply failure (FPF) is estimated on the basis of the max stress failure criterion [35]. This yields a corresponding force of $F_{FPF} = 8.00$ kN. The Young's modulus of the specimen has been determined experimentally to 40.21 GPa.

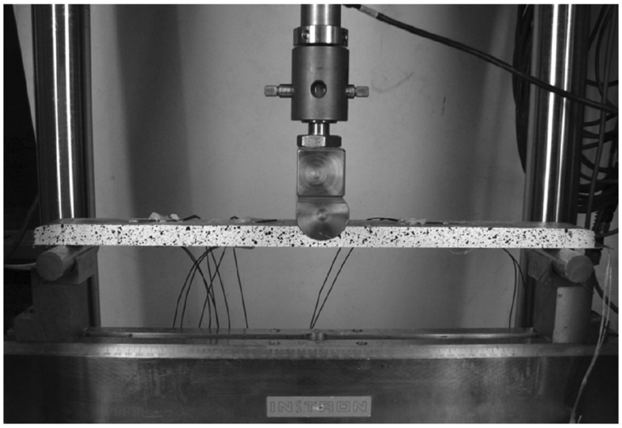

Figure 4: The three-point bending setup with a GFRP beam applied strain gauges, speckle pattern and FBG sensors

Control Loop

The control loop enables static displacement control operated by a feedback signal acquired from the test specimen using DIC or FBG measurements. This control system follows the architecture of a single input-single output feedback control loop [36]. This test configuration is implemented in LabVIEW 8.6, and the implemented test algorithm includes two independent systems: the displacement controlled actuator and the external data acquisition (DAQ) system. The displacement controlled hydraulic actuator is operated through an MTS FlexTest 60 servo controller [37] by the TCP/IP port using a dynamic link library (DLL) [38]. The external DAQ system includes the DIC and FBG measurements. The control loop is executed in a state-machine framework [39] according to the flowchart illustrated in Figure 5.

The control loop is initiated by feeding a displacement input to the servo controller (1) operated by a feedback signal from the LVDT in the actuator. In (2), the actuator is moved towards the end level in a monotonic motion with a predefined time rate. When the defined displacement is reached, the data from the servo controller: LVDT and load cell signals along with the external measurements: FBG and DIC are acquired by (3) and (4), respectively. The displacement input is compared with the response of the specimen, and a deviation is derived. If the deviation is within the error tolerance, the control loop is ready to receive the next user defined displacement input in (6). If the deviation exceeds the error tolerance, the actuator is moved in the direction necessary to reduce the error with a magnitude equal to the deviation. This is carried out by repeating the entire loop from (1) – (5) until a deviation below the error tolerance is obtained.

FBG system—control loop communication

A real-time communication between the I-MON 512E interrogator and the LabVIEW is established through the USB port by a dynamic link library (DLL) [40]. These DLL files are implemented directly in the LabVIEW environment, while all the data analyses are hard-coded in the LabVIEW according to [41]. The functions in the control sequence are presented in a flow chart diagram in Figure 6.

In Figure 6, the communication is initiated in (1), which identifies and configures a communication between the LabVIEW and the I-MON interrogator. The data are collected in a block mode setup separated in three tasks: acquire a single image, convert the analogue signal to an

Table 1: Mechanical properties of a UD-glass fibre ply

E_1 (GPa)	E_2 (GPa)	G_{12} (GPa)	υ_{12} (−)	$\hat{\sigma}_{1t}$ (MPa)	$\hat{\sigma}_{1c}$ (MPa)	$\hat{\sigma}_{2t}$ (MPa)	$\hat{\sigma}_{2c}$ (MPa)	$\hat{\tau}_{12}$ (MPa)
40	9.8	2.8	0.3	1100	600	20	140	70

© 2014 Wiley Publishing Ltd
doi: 10.1111/str.12089

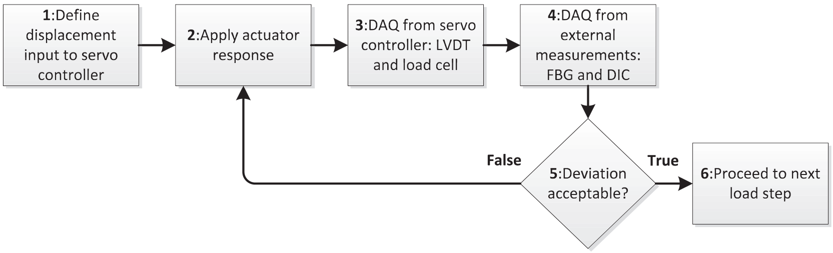
1:Define displacement input to servo controller
2:Apply actuator response
3:DAQ from servo controller: LVDT and load cell
4:DAQ from external measurements: FBG and DIC
5:Deviation acceptable?
False
True
6:Proceed to next load step

Figure 5: Control loop algorithm operating and acquiring data from servo controller, FBG interrogator and DIC system

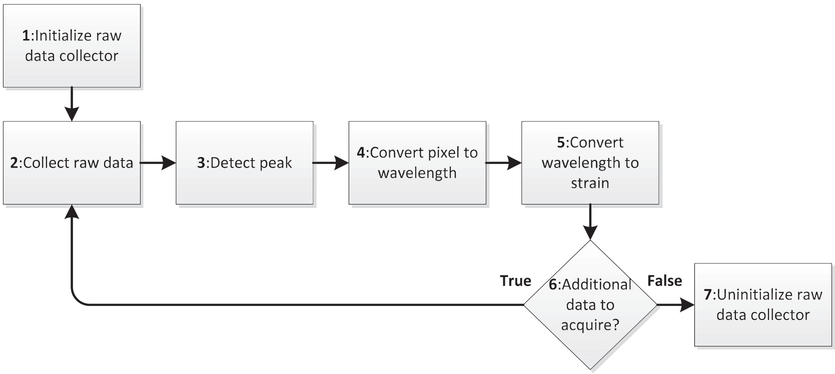
1:Initialize raw data collector
2:Collect raw data
3:Detect peak
4:Convert pixel to wavelength
5:Convert wavelength to strain
6:Additional data to acquire?
True
False
7:Uninitialize raw data collector

Figure 6: Communication procedure between control loop algorithm and FBG interrogator

array of discrete intensity data and transfer the data from the PCB buffer to the LabVIEW software. The data acquisition is performed in (2) with a predefined cycle time for each iteration. The photoelectrical signal is generated by the linear image sensor consisting of 512 elements. Each element represents one pixel in the image sensor, while the appertaining integer describes the individual pixel response generated by the incident light. The locations of the pixels representing the reflection peak, generated by the reflection spectra of the multitude FBG sensors, are identified in (3). The function pinpoints the individual pixels exceeding the pixel response, defined by a threshold parameter. By a Gaussian fit routine, the location of the peak is determined by including a predefined number of neighbouring pixels in the analysis. In (4), the relation between the pixels on the linear image sensor and the optical wavelength is described by a fifth degree polynomial [33]. A compensation for temperature drift in the interrogator is included by a correction equation [33]. All calibration coefficients are acquired through the USB port from the electronically erasable programmable read-only memory (EEPROM). The relation between the wavelength and strain, present in each FBG included in the system, is outlined in (5) cf. Equation (1). If no additional measurements from the I-MON interrogator are required (6), the programme is stopped (7). This is done by releasing the main PCB internal image data buffer, USB camera, and finally, the USB device and DLL.

Strain control by FBG

The FBG strain control is performed by using strain data from the FBG sensors to obtain an equivalent displacement at the loading point. This is inserted as a displacement input in the control loop cf. Figure 5. The strains at the location of the FBG sensors are converted to a displacement by Bernoulli–Euler beam theory, Navier's stress relation and Hooke's law.

$$\frac{d^2u}{dx^2} = -\frac{M}{EI}z, \qquad \sigma = \frac{M}{I}z, \qquad \sigma = E\varepsilon \tag{2}$$

This yields two relations between displacement and strain for the three-point bending load case

$$u_{max} = \frac{1}{24}\frac{L^3\varepsilon(x)}{xz} \text{for } x \leq \frac{L}{2} \tag{3}$$

$$u_{max} = \frac{1}{24}\frac{L^3\varepsilon(x)}{(L-x)z} \text{ for } x \geq \frac{L}{2} \tag{4}$$

where x is the position in the x-direction cf. Figure 3, u_{max} is the deflection at centre position, L is the length between the support points, z is the distance from the neutral axis to the FBG sensors in the y-direction and $\varepsilon(x)$ is the strain in the x-direction at the position x. The displacement input at the loading point is derived as the average deflection of all six FBG sensors embedded in the specimen cf. Figure 3.

DIC system—control loop communication

The GOM IVIEW software is an extension to the ARAMIS measurement system capable of acquiring single measurement points on the specimen surface in real time [17]. From each measurement point, the 3D coordinates are obtained and fed to the LabVIEW program through a TCP/IP connection. The TCP/IP communication and image processing, performed by IVIEW, is handled in a Python macro with commands from the GOM package [42]. The steps in the communication between the two systems are presented by the flowchart in Figure 7.

In Figure 7, the communication between LabVIEW and DIC is initiated by opening a TCP/IP port in (1). When this communication is established and verified, the LabVIEW application sends a trigger signal to (2) initiating the image acquisition with a predefined frame rate. The coordinates for each measurement point are calculated real time and fed to an internal image buffer. LabVIEW is requesting image data in (3) by generating a trigger signal. This trigger signal is fed through the TCP/IP connection to (4) transferring the data stored in the buffer to (5). When all the data are transferred, the image data buffer is overwritten with new image data while waiting for the next trigger signal by (3). When all the requested data are acquired and the LabVIEW application is terminated, the TCP/IP connection is closed by (7).

Displacement control by DIC

DIC displacement control is carried out using the displacement signals from the measurement points on the surface, cf. Figure 3, to obtain an equivalent displacement at the loading point. These data are inserted as a displacement input for the control loop cf. Figure 5. The relation between the maximum displacement and displacement at a given coordinate *x* is again derived from the Bernoulli–Euler beam theory.

$$u_{max} = \frac{u(x)}{3\left(\frac{x}{L} - \frac{4}{3}\left(\frac{x}{L}\right)^3\right)} \; for \; x \leq \frac{L}{2} \tag{5}$$

$$u_{max} = \frac{u(x)}{4\left(\left(1 - \frac{x}{L}\right)\left(\frac{2x}{L} - \frac{1}{4} - \left(\frac{x}{L}\right)^2\right)\right)} \; for \; x \geq \frac{L}{2} \tag{6}$$

where *u(x)* is the displacement in the *y*-direction at position *x*. The displacement input is obtained by averaging the u_{max} calculated from each of the three measurement points.

Results

A GFRP specimen is tested within the linear elastic regime in a three-point bending rig cf. Figure 4 with a ramped displacement rate of 1 mm s^{-1}. The setup is operated by a feedback signal from the test specimen by using FBG and DIC measurements for static strain and displacement control, respectively.

FBG sensor strain control

Static strain control by FBG is utilised to limit the deviation between the displacement input and FBG measurements, within a given error tolerance. The magnitude of this tolerance is given on the basis of the measurement uncertainty and repeatability [43] offered by the FBG system. The repeatability has a standard uncertainty of 0.0994 μm m^{-1} from a sample of 160 measurements for each FBG, acquired under constant conditions with a frequency of 970 Hz. The stand-alone interrogation monitor measures wavelengths with an accuracy of ±10 pm cf. [33], which corresponds to ±8.3 μm m^{-1} cf. Equation (1). The error tolerance is defined to ±20 μm m^{-1}, which is equal to approx. ±0.69% of the peak strain, cf. Figure 8. A displacement input with a triangular waveform is applied including 91 iterations forming five peaks. The peak-to-peak amplitude of the displacement input is 2900 μm m^{-1} between plies 21–22 at the loading point, see Figure 3. The displacement input is validated by FBG measurements,

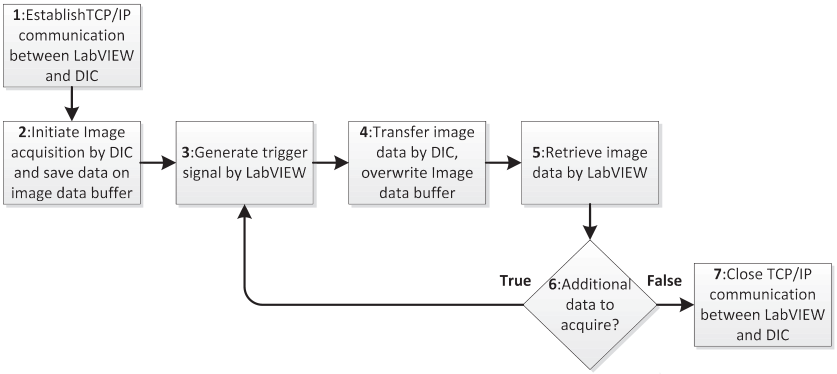
1:EstablishTCP/IP communication between LabVIEW and DIC
2:Initiate Image acquisition by DIC and save data on image data buffer
3:Generate trigger signal by LabVIEW
4:Transfer image data by DIC, overwrite Image data buffer
5:Retrieve image data by LabVIEW
True
6:Additional data to acquire?
False
7:Close TCP/IP communication between LabVIEW and DIC

Figure 7: Communication procedure between: control loop algorithm and DIC system

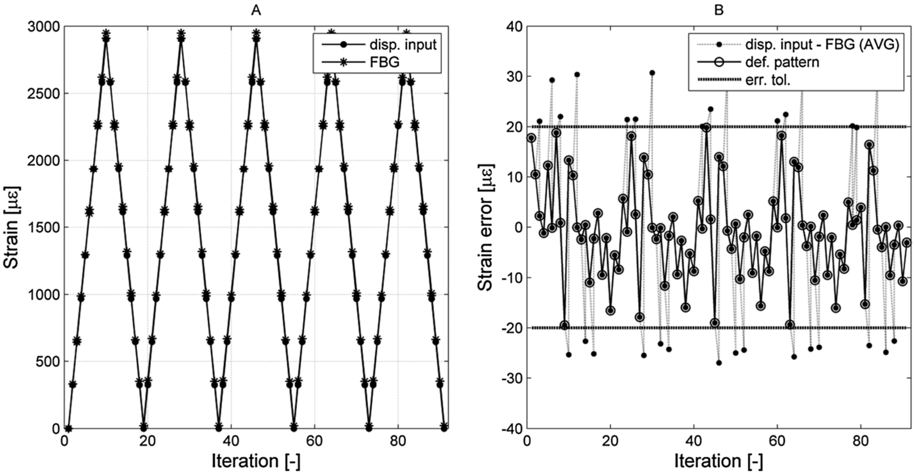

Figure 8: Strain control by FBG (A) displacement input and FBG and (B) discrepancy between displacement input and FBG

which are calculated by converting the strain data from each FBG sensor to obtain an equivalent strain between plies 21–22 at the centre of the beam and take the average of all six measurements. Operated by a feedback signal from the FBG measurements, the prescribed displacement input along with the appurtenant FBG measurement is presented in Figure 8A. Furthermore, the deviation between the displacement input and FBG measurement is available in Figure 8B.

In Figure 8B, multiple violations of the error tolerance are observed. The system reacts by adjusting the position of the actuator in the direction necessary to reduce of the error. The resulting displacement pattern operated within the error tolerance is marked with circles in Figure 8B. The discrepancy between the displacement input and each of the six FBG measurements is presented in Figure 9.

Except FBG 2 and FBG 5, a linear dependent discrepancy between the displacement input and FBG reading is observed in Figure 9. This could indicate an unexpected variation of the inter-ply location of the embedded optical fibre. However, other effects including stress concentrations generated by the support rollers /loading nose and imperfections in the specimen also have an influence. The average time elapsed between each iteration is approx. 3.5 s. Three tests are accomplished on the same test specimen. The number of adjustments, needed to maintain a deviation within the error tolerance for each test is presented in Table 2.

To validate the output from the FBG sensors, six strain gauges are attached to the specimen: three at the top in compression and three at the bottom in tension cf. Figure 3. With the assumption of having a linear variation of the strain in the ply stack thickness (y-direction), the measurements from the FBG are compared directly with the strain gauge. This is done by multiplying the strain gauge measurement with the factor n, which is the distance from the neutral axis (plies 11–12) to the position of the FBG (plies 21–22) divided by half the beam thickness. A load–strain curve is presented in Figure 10 for specimen 1, including the strain in the FBG and appertaining strain gauge multiplied by an n factor of 0.91.

Except SG-3/FBG-3 and SG-1/FBG-1, a small deviation between the FBG and strain gauge is detected. However, a systematic error between the FBG and appurtenant strain gauge is detected for all six cases with a confidence interval of 95%. To accept the hypothesis of having a random error between the FBG and appurtenant strain gauge, the factor n is adjusted. The results are presented in Table 3 for five different test specimens.

The empty cells in Table 3 refer to a lack of data due to malfunctioning of strain gauges during testing.

DIC displacement control

Static strain control by DIC is performed to restrict the discrepancy between the displacement input and DIC measurements within a predefined error tolerance. The magnitude of the error tolerance is given on the basis of the measurement uncertainty and repeatability [43] offered by the DIC system. The repeatability is determined from a sample of 100 measurements for each measurement point, acquired under unchanged conditions to have a standard uncertainty of 2.91 μm. The measurement uncertainty is determined as the discrepancy between the displacement measured at a measurement point by the DIC system and a micrometre. With 10 samples equally distributed over a displacement range of 0–6 mm, the measurement uncertainty is 0.01 mm. From the given measurement uncertainty and repeatability, an error tolerance of ±0.01 mm is defined, which is equal to 0.17% of the peak displacement. A displacement input with a triangular waveform is assigned including 91 iterations forming five peaks. The peak-to-peak amplitude of the displacement

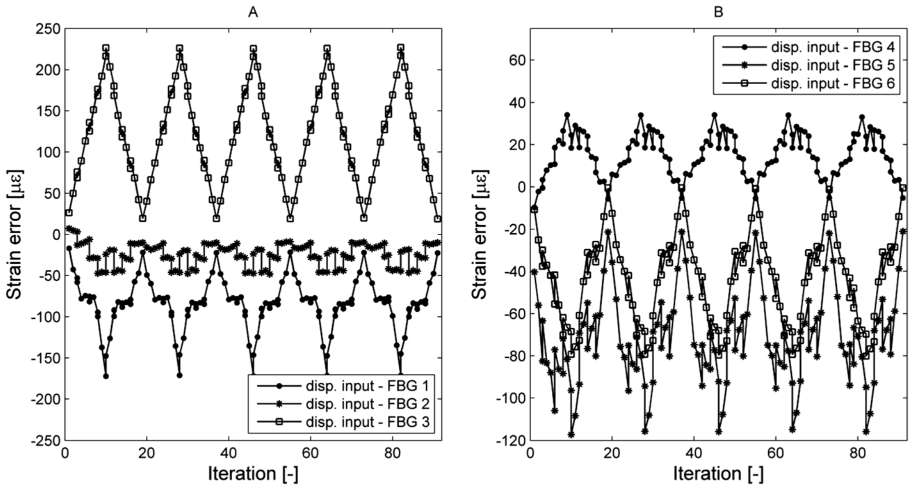

Figure 9: Discrepancy between displacement input and each FBG: (A) FBG 1–3 and (B) FBG 4–6

Table 2: Number of adjustments required in strain control by FBG for each test

Test number (–)	Number of adjustments (–)
1	28
2	26
3	24

input is 5.87 mm at the loading point of the specimen. The displacement input is validated by DIC measurements, which are generated by converting the displacement from each stage point to an equivalent displacement at the loading point and take the average of all three measurements. Operated by a feedback signal from the DIC measurements, the prescribed displacement input along with the appurtenant DIC measurement is presented in Figure 11A. Furthermore, the deviation between the displacement input and DIC measurement is available in Figure 11B.

In Figure 11B, the discrepancy between the displacement input and DIC measurements exceeds the error tolerance multiple times. The system reacts by moving the actuator with a magnitude equal to the respective displacement error. The resulting displacement pattern operated within the error tolerance is marked with circles. The discrepancy between the displacement input and each of the three DIC measurements is presented in Figure 12.

In Figure 12, a linear dependent discrepancy between the displacement input and DIC measurement is observed. The discrepancy increases when enlarging the distance between the loading nose and measurement point in the *x*-direction (see Figure 3). This tendency may be due to the assumptions

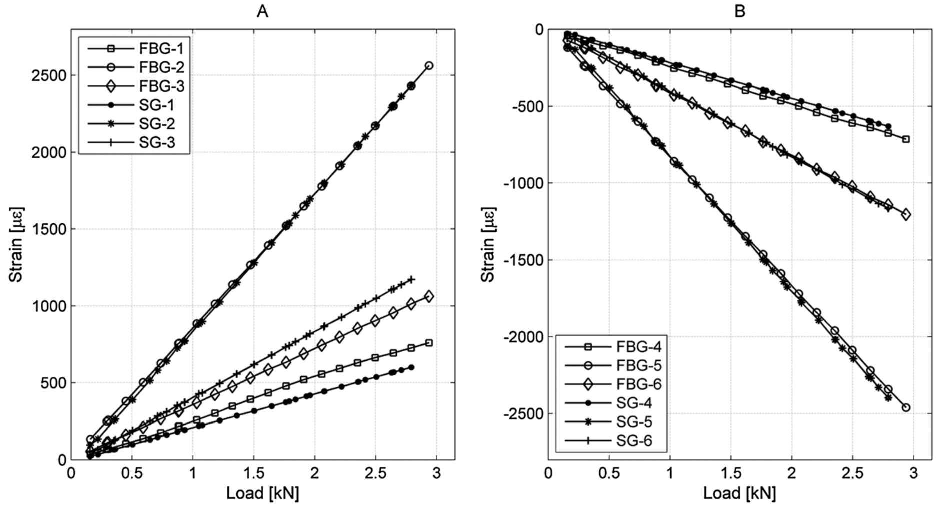

Figure 10: Load–strain curve for each individual FBG and SG: (A) bottom fibres in tension and (B) top fibres in compression

Table 3: Factor n to eliminate the deviation between the FBG and appurtenant strain gauge

Test specimen (−)	SG1 (−)	SG2 (−)	SG3 (−)	SG4 (−)	SG5 (−)	SG6 (−)
1	1.01	0.92	0.83	1.14	0.93	0.77
2	0.98	0.93	-	1.00	0.86	0.74
3	1.13	0.89	0.77	0.97	0.87	0.87
4	0.94	-	0.86	0.72	0.79	0.95
5	0.85	-	0.88	1.00	-	0.83

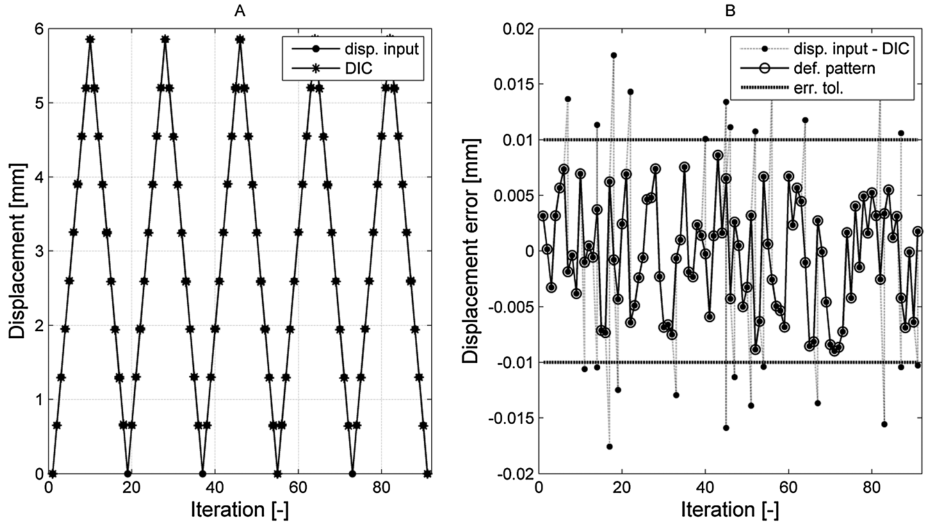

Figure 11: Strain control by DIC: (A) displacement input and DIC and (B) deviation between displacement input and DIC

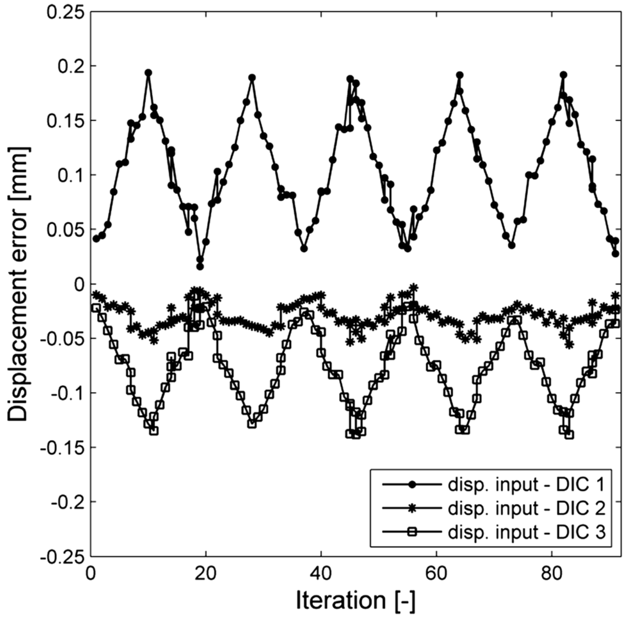

Figure 12: Discrepancy between displacement input and each DIC measurement

concerning the displacement shape of the beam, not being fulfilled. The average time elapsed between each iteration is approx. 3.5 s, and three tests are accomplished on the same test specimen. The number of adjustments needed to maintain a deviation within the error tolerance for each test is presented in Table 4.

Discussion

Control loop

In this investigation, the control loop was successfully demonstrated using two different measurement techniques: FBG and DIC for strain and displacement controls, respectively. Each time the discrepancy between the displacement input and the actual response of the specimen exceeded the error tolerance, the system reacted by moving the actuator with a magnitude equal to the respective displacement error. When the discrepancy was within the error tolerance, the next displacement input was applied in the subsequent iteration.

Table 4: Number of adjustments required in displacement control by DIC for each test

Test number (−)	Number of adjustments (−)
1	25
2	17
3	20

The control loop operated with an iteration frequency of 0.29 Hz for the given system, this frequency could be enhanced by using better hardware to operate the control loop. However, changing the system architecture from a state-machine framework to a cascade feedback loop would be another opportunity allowing a full dynamic response of the system [2]. However, given that the sampling rate of the external measurements is lower than the bandwidth of the PID controller, multiple iterations are made without knowing whether the error tolerance is exceeded. This means that, depending on the bandwidth of the external measurement system and PID controller, a number of iterations that are performed between each correlation are executed.

FBG sensor strain control

The control loop was successfully demonstrated for strain control with an error tolerance of $\pm 20\,\mu\mathrm{m\,m^{-1}}$, which generated a total of 24–28 correlating adjustments with a total of 91 iterations cf. Figure 8A. According to Figure 8B, it is expected that the number of correlating adjustments is increased if the error tolerance is decreased and vice versa. With a measurement uncertainty and repeatability of $\pm 8.3\,\mu\mathrm{m\,m^{-1}}$ and $0.0994\,\mu\mathrm{m\,m^{-1}}$, respectively, an error tolerance of $\pm 20\,\mu\mathrm{m\,m^{-1}}$ was accepted. However, decreasing the error tolerance to the level of the measurement uncertainty would be an opportunity.

The FBG measurements were compared with strain gauges as a reference, and a systematic error was detected for all six FBGs. This is mainly caused by a combination of two effects: the stress concentrations generated by the support rollers / loading nose and imperfections in the specimen. However, other effects also affect the FBG signal [30]. When comparing the strain acquired by the FBG system with the measurements from the strain gauges, some mismatches are detected cf. Figure 10 and Table 3. This could be explained by stress concentrations along with variations of the distance between the neutral axes to the FBG sensor. However, when $n \geq 1$, cf. Table 3, the FBG sensor appears to be positioned at the same level or above the appurtenant strain gauge. This indicates that the stress concentrations have a significant impact on the FBG measurements rather than variations of the FBG position. To support that theory, previous research with similar specimens showed that the optical fibres were found to be situated at the same inter-ply region [34].

The strain data from the FBG measurement are converted to an equivalent displacement by the Bernoulli–Euler beam theory. An error of that reconstructed displacement will be present due to the number of strain sensors, position of the strain sensors and uncertainty of the strain sensor signal [16]. That error could be erased by calibrating the FBG signal against the surface displacement as a function of the induced forces. However, that solution is only valid when staying within the linear elastic response.

DIC displacement control

The control loop was successfully demonstrated for displacement control with an error tolerance of ±0.01 mm, which generated a total of 17–25 correlating adjustments with a total of 91 iterations, Figure 11. According to Figure 11, it is expected that the number of correlating adjustments is increased if the error tolerance is decreased and vice versa. With a measurement uncertainty and repeatability of 0.01 mm and 2.91 μm, respectively, an error tolerance of ±0.01 mm was selected.

The static displacement control uses three measuring points to reduce the signal noise and the influence of local effects e.g. stresses concentrations, material defects and geometrical imperfections. However, when multiple measurement points are included, it is necessary to make assumptions concerning the displacement shape of the beam that might not be fulfilled. This could be avoided by oversampling a single measurement point, but this approach will only improve the repeatability, not the bias.

In [2], the standard displacement uncertainty is calculated to $\rho_u = 0.0421$ pixels for a facet size of 15 × 15 pixels and shift of 15 pixels. In this study, the standard displacement uncertainty is calculated to 3.3021 μm for a facet size of 15 × 15 pixels and shift of 15 pixels. This is converted to pixels by the measurement height of 330 mm and camera height resolution of 1728 pixels, thereby, 5.236 pixels/mm. With a displacement deviation of 2.91 μm, the resolution is 0.015pixels. This is 2.8 times higher pixel resolution than found in [2].

Conclusion

Five GFRP beams were loaded in the linear elastic regime in a three-point bending test configuration controlled by feedback signals from DIC and FBG measurements for displacement and strain control, respectively, obtained directly on or inside the specimen. The test configuration was obtained using a control loop algorithm, operating and acquiring data from the servo-hydraulic controller, FBG interrogator and DIC system. It was demonstrated that such a test configuration is beneficial when a given stress state is required as a control parameter in connection with e.g. a complex test rig, loading configuration or specimen geometry. With the precision and accuracy offered by the DIC and FBG system, the test setup was capable of operating within an error tolerance of 0.01 mm and $20\,\mu\mathrm{m\,m}^{-1}$ for displacement and strain controls, respectively.

ACKNOWLEDGEMENTS

The authors would like to acknowledge the financial support from the Danish Centre for Composite Structures and Materials (DCCSM) funded by the Danish Council for Strategic Research within Sustainable Energy and Environment (Grant 09-067212).

REFERENCES

1. Mallat, A. and Alliche, A. (2011) A modified tensile test to study the behaviour of cementitious materials. *Strain* **47**, 499–504.
2. Fayolle, X., Galloch, S. and Hild, F. (2007) Controlling testing machines with digital image correlation. *Exp. Tech.* **31**, 57–63.
3. Udd, E. (1996) Fiber optic smart structures. *IEEE* **84**, 60–67.
4. Khoun, L., Oliveira, R. D., Michaud, V. and Hubert, P. (2011) Investigation of process-induced strains development by fibre Bragg grating sensors in resin transfer moulded composites. *Composites* **42**, 274–282.
5. Molimard, J., Vacher, S. and Vautrin, A. (2010) Monitoring LCM Process by FBG sensor under birefringence. *Strain* **47**, 364–373.
6. Hsieh, M. Y., Tsai, L., Chiang, C. C., Lin, C. L. and Fang, B. L. (2012) Curing residual strain monitoring in different layer of Gr/Epoxy laminated composites using embedded optical fiber Bragg grating sensors. *SPIE* **8409**, 1–8.
7. Mitzutani, Y. and Groves, R. M. (2011) Multi-functional measurements using a single FBG sensor. *Exp. Mech.* **51**, 1489–1498.
8. Zhang, H., Ghandehari, M. and Sidelev, A., *et al.* (2011) Monitoring the hysteresis effects in a strain-stress curve of carbon fiber reinforced laminates by FBG technology. *SPIE* **7753**, 1–4.
9. Palaniappan, J., Ogin, S. L., Thorne, A. M., Reed, G. T., Crocombe, A. D., Capell, T. F., Tjin, S. C. and Mohanty, L. (2008) Disbond growth detection in composite–composite single-lap joints using chirped FBG sensors. *Compos. Sci. Technol.* **68**, 2410–2417.
10. Ling, H.-Y., Lau, K.-T., Su, Z. and Wong, E. T.-T. (2007) Monitoring mode II fracture behaviour of composite laminates using embedded fiber-optic sensors. *Composites* **38**, 488–497.
11. Gebremichael, Y. M., Li, W. and Meggitt, B. T., *et al.* (2005) A field deployable, multiplexed Bragg grating sensor system used in an extensive highway bridge monitoring evaluation tests. *IEEE Sens. J.* **5**, 510–519.
12. Kerrouche, A., Boyle, W. J. O., Sun, T., Grattan, K. T. V., Schmidt, J. W., Täljsten, B. (2009) Enhanced FBG sensor-based system performance assessment for monitoring strain along a prestressed CFRP rod in structural monitoring. *Sens. Actuators, A* **151**, 127–132.
13. Kerrouche, A., Boyle, W. J. O., Gebremichael, Y., Sun, T., Grattan, K. T. V., Täljsten, B. and Bennitz, A. (2008) Field tests of fibre Bragg grating sensors incorporated into GFRP for railway bridge strengthening condition monitoring. *Sens. Actuators, A* **148**, 68–74.
14. Gebremichael, Y. M., Li, W. and Boyle, W. J. O., *et al.* (2005) Integration and assessment of fibre Bragg grating sensors in an all-fibre reinforced polymer composite road bridge. *Sens. Actuators, A* **118**, 78–85.
15. Kerrouche, A., Leighton, J., Boyle, W. J. O., Gebremichael, Y. M., Sun, T., Grattan, K. T. V. and Täljsten, B. (2008) Strain measurement on a rail bridge loaded to failure using a fiber Bragg grating-based distributed sensor system. *Sens. Actuators, A* **8**, 2059–2065.
16. Mueller, U. C., Zeh, T., Koch, A. W. and Baier, H. (2006) Fiber optic Bragg grating sensors for high-precision structural deformation control in optical systems. *SPIE* **6167**, 127–132.
17. Guastavino, R. and Göransson, P. (2007) A 3D displacement measurement methodology for anisotropic porous cellular foam materials. *Polym. Test.* **26**, 711–719.
18. Owolabi, G. M. and Singh, M. N. K. (2009) A comparison between two analytical models that approximate notch-root elastic-plastic strain-stress components in two-phase, particle-reinforced, metal matrix composites under multiaxial cyclic loading: experiments. *Int. J. Fatigue* **28**, 918–925.
19. Jones, A., Shaw, J. and Wineman, A. (2006) An experimental facility to measure the chemorheological response of inflated elastomeric membranes at high temperature. *Exp. Mech.* **46**, 579–587.
20. Moser, R. and Lighter, J. G. (2007) Using three-dimensional digital imaging correlation techniques to validate tire finite-element model. *Exp. Tech.* **31**, 29–36.
21. Helm, J. D., Sutton, M. A. and McNeill, S. R. (2003) Deformations in wide, center-notched, thin panels, Part I: three-dimensional shape and deformation measurements by computer vision. *Opt. Eng.* **42**, 1293–1305.
22. Vialettes, P., Siguier, J.-M., Guigue, P., Karama, M., Mistou, S., Dalverny, O., Granier, S. and Petitjean, F. (2006) Experimental and numerical simulation of super-pressure balloon apex section: mechanical behavior in realistic flight conditions. *Adv. Space Res.* **37**, 2077–2081.
23. Leblanc, B., Niezrecki, C., Avitabile, P., Chen, J., Sherwood, J. and Hughes, S. (2011) Full-field inspection of a wind turbine blade using three-dimensional digital image correlation. *SPIE* **7979**, 2077–2081.
24. Luo, P. F. and Huang, F. C. (2000) Application of stereo vision to the study of mixed-mode crack-tip deformations. *Opt. Lasers Eng.* **33**, 349–368.
25. Corr, D., Accardi, M., Graham-Brady, L. and Shah, S. (2007) Digital image correlation analysis of interfacial debonding properties and fracture behavior in concrete. *Eng. Fract. Mech.* **74**, 109–121.
26. Pan, B. and Li, K. (2011) A fast digital image correlation method for deformation measurement. *Opt. Lasers Eng.* **49**, 841–847.

27. Siebert, T. and Crompton, M. J. (2010) Application of high digital image correlation for vibration mode shape analysis. In: *Society of the SEM Annual Conference*, Indianapolis, Indiana USA.
28. Siebert, T., Becker, T., Splitthof, K. and Neumann, I. (2007) High-speed digital image correlation: error estimations and applications. *Opt. Eng.* **46**, 51004/1-7.
29. Arora, H., Hooper, P. A. and Dear, J. P. (2011) Dynamic response of full-scale sandwich composite structures subject to air-blast loading. *Composites Part A* **42**, 1651–1662.
30. Chan, T. H., Yu, L., Tam, H. Y., Ni, Y. Q., Liu, S. Y., Chung, W. H. and Cheng, L. K. (2006) Fiber Bragg grating sensors for structural health monitoring of Tsing Ma bridge: background and experimental observation. *Eng. Struct.* **28**, 648–659.
31. Kreuzer, M. (2013) Strain Measurement with Fiber Bragg Grating Sensors. HBM, Darmstadt, Germany
32. Sutton, M. A., Orteu, J.-J. and Schreier, H. W. (2009) Image Correlation for Shape, Motion and Deformation Measurements, Springer, New York, U.S.A.
33. GOM, ARAMIS. (2006) User Manual - Software. GOM, Braunschweig, Germany.
34. Ibsen Photonics. (2009) I-MON E-USB 2.0 Product Specification. Ibsen Photonics A/S, Farum, Denmark.
35. Nielsen, M. W., Wittrup-Schmidt, J., Hattel, J., Høgh, J. H., Waldbjørn, J. P., Andersen, J. and Markussen, T. L. (2014) Life cycle strain monitoring in glass fibre reinforced polymer laminates using embedded fibre Bragg grating sensors from manufacturing to failure. *Composites Materials, to be published* **48**, 365–381.
36. Zenkert, D. and Battley, M. (2006) Composite Lightweight Structures, DK-2800 Kgs. Technical University of Denmark, Lyngby, Denmark
37. Svrcek, W. Y., Mahoney, D. P. and Young, B. R. (2007) Fundamentals of single input-single output systems. In: Fundamentals of Single Input-Single Output Systems in A Real-Time Approach to Process Control. John Wiley & Sons Ltd., Chichester, UK.
38. MTS. (2004) FlexTest SE & GT Digital Servocontrollers. MTS Systems Corporation, Minnesota, U.S.A.
39. MTS. (2009) LabVIEW Programming Libraries: Model 793.00 Software. MTS Systems Corporation, Minnesota, U.S.A.
40. Bitter, R., Mohiuddin, T. and Nawrocki, M. (2001) LabView Advanced Programming Techniques. CRC Press, Boca Rotan, Florida, USA.
41. Ibsen Photonics. (2011) Camera driver manual. Ibsen Photonics A/S, Farum, Denmark.
42. Ibsen Photonics. (2011) User Manual, Ibsen Photonics A/S, Farum, Denmark.
43. GOM. (2006) The GOM Scripting Language. GOM, Braunschweig, Germany.

HYBRID TESTING OF COMPOSITE STRUCTURES WITH SINGLE-AXIS CONTROL

Jacob Waldbjørn[1], Jacob Høgh[1], Henrik Stang[1], Christian Berggreen[1], Jacob Wittrup-Schmidt[1],
Kim Branner[2]
[1]Department of Civil Engineering, Technical University of Denmark, Kgs. Lyngby, Denmark
[2]Department of Wind Energy, Technical University of Denmark, Roskilde, Denmark

Keywords: *hybrid testing, hardware-in-the-loop, substructural testing, composites, three point bending, finite element modelling, high-precision control*

Abstract

Hybrid testing is a substructuring technique where a structure is emulated by modelling a part of it in a numerical model while testing the remainder experimentally. Previous research in hybrid testing has been performed on multi-component structures e.g. damping fixtures, however in this paper a hybrid testing platform is introduced for single-component hybrid testing. In this case, the boundary between the numerical model and experimental setup is defined by multiple Degrees-Of-Freedoms (DOFs) which highly complicate the transferring of response between the two substructures. Digital Image Correlation (DIC) is therefore implemented for displacement control of the experimental setup. The hybrid testing setup was verified on a multicomponent structure consisting of a beam loaded in three point bending and a numerical structure of a frame. Furthermore, the stability of the hybrid testing loop was investigated for different ratios of stiffness between the numerical model and test specimen. It was found that when deformations were transferred from the numerical model to the experimental setup, the hybrid test was only stable when the stiffness of the numerical model was higher than the test specimen. The hybrid test gave similar results as a numerical simulation of the full structure. The deviation between the two was primarily due to the response of the specimen in the hybrid test being one load step behind the numerical model.

1 Introduction

In hybrid testing a structure is emulated by combining the response of an experimental- and numerical substructure. The main part of the emulated structure is modelled in a simulation and a part of special interest is tested in an experiment [1], [2]. When combining the response of the two, the behaviour of the full emulated structure can be obtained. With this technique, the response of a given substructure displaying non-linear behaviour e.g. buckling, fracture, can be investigated when exposed to the effect of the remaining structure, without conducting full-scale experiments.

Hybrid testing has previously been applied to investigate seismic protection of building structures [3], [4], [5]. For this application the load bearing structure has been simulated in a numerical model while damping fixtures has been tested experimentally, e.g. elastomer [6], stud types [7], [8], magneto-rheological [4], [9], [10]. These tests were dynamic and the focus was therefore to minimize the time lack between the numerical- and experimental component. This has been done by optimization of e.g. the numerical algorithms [11], [12], [13], and the actuator response [14], [15].

In all of these tests the numerical- and experimental component has been two separate – typically simply connected - structural components and this setup is referred to as multi-component hybrid testing. If hybrid testing is applied to a single-component structure e.g. wind turbine blade, boat hull etc. the boundary conditions between the numerical- and experimental substructure becomes more complicated. This is because the two substructures share boundaries along an edge of a structure instead of e.g. a clearly defined hinge as in the case of a hybrid test with a magneto-rheological damper [4], [9], [10]. This results in single-component hybrid testing having continuous boundaries between the two substructures, resulting in – in principle - an infinite amount of Degrees-Of-Freedom (DOF), compared to multi component hybrid testing where only a limited number of DOFs are present [1], [16]. It is therefore more complicated to monitor and control the deformations of the experimental substructure in a single-component hybrid test. This emphasizes the need for advanced measuring techniques to enable high-precision control of the experimental setup, as presented in [17].

The scope of this paper is to introduce and verify a sound base for single-component quasi-static hybrid testing. Digital Image Correlation (DIC) was implemented as a method to measure deformations to be used in the control loop. A quasi-static hybrid test on a multi component frame structure was conducted to reduce the complexity in verifying the software capabilities when handling the test response and theory. Here the numerical component was a Finite Element (FE) model of a simple frame structure and the experimental specimen a composite beam loaded in three point bending.

2 Hybrid Testing Communication Loop

The Quasi-static hybrid testing platform provides the capability to experimentally test a substructure of interest while simulating the remainder in a numerical model. The software is capable of: executing a FE-model, operating the hydraulic actuators through a multi-axial Proportional-Integral-Derivative (PID) controller and acquire data from several gauges on the test setup. The platform is operated by LabVIEW 8.6 and is executed in a state machine [18] presented in Figure 1.

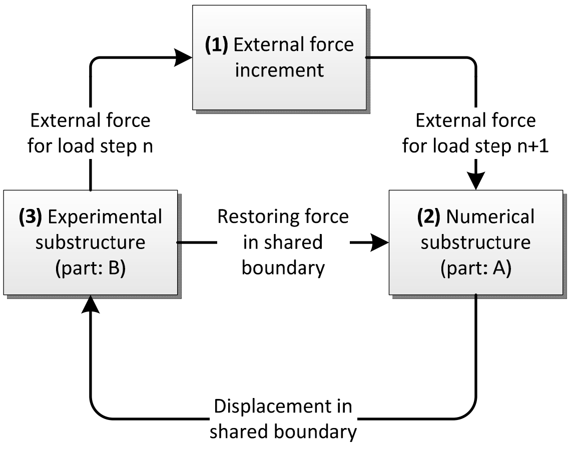
(1) External force increment
External force for load step n
External force for load step n+1
(3) Experimental substructure (part: B)
Restoring force in shared boundary
(2) Numerical substructure (part: A)
Displacement in shared boundary

Figure 1: Dataflow in the quasi-static hybrid testing communication loop

An external force is applied to the numerical model **(1)** and the equivalent displacement at the shared boundary calculated for the numerical substructure in **(2)**. This displacement is transferred to the experimental substructure by the hydraulic actuators in **(3)** controlled by a feedback signal acquired on the test specimen to omit the effect of compliance in the load train cf. [17]. Finally, the restoring force – i.e. the reaction force from the test specimen - in the shared boundary of the experimental substructure is fed back to the shared boundary of the numerical substructure in order to achieve equilibrium at the interface between the two. The loop is repeated by defining the next load increment in **(1)**.

2.1 Numerical substructure (Part A)

The numerical substructure executed by **(2)** in Figure 1 is established through a link between LabVIEW 8.6 and ANSYS 12.1. The steps included in the communication between the two applications are presented in Figure 2.

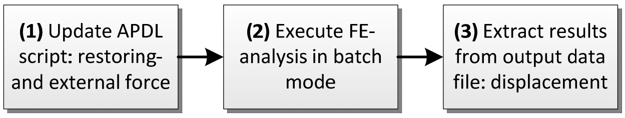
(1) Update APDL script: restoring- and external force
(2) Execute FE-analysis in batch mode
(3) Extract results from output data file: displacement

Figure 2: Dataflow in the LabVIEW and FE-analysis communication (Part A)

The FE-model is defined through the ANSYS Parametric Design Language (APDL-script) which defines geometry, material properties, loads etc. The variable parameters in the APDL-script: external load P_{ext} and restoring force in the shared boundary R_n (see Figure 5) are identified and updated by **(1)**. The APDL-script is executed in **(2)** by the ANSYS software through the windows command prompt. The output data is returned in a text file and the displacement at the shared boundary extracted by **(3)**.

2.2 Experimental substructure (Part B)

The experimental substructure operated by **(3)** in Figure 1 is established through a link between LabVIEW 8.6 and two independent systems: the hydraulic actuator and external Data Acquisition (DAQ) system. The displacement controlled hydraulic actuator is operated through a MTS FlexTest 60 controller [19] by the TCP/IP port using a dynamic link library (DLL) [20]. The external DAQ system collects data from the measuring device DIC [21]. The steps in the communication between LabVIEW, PID-controller and external measuring device are represented in Figure 3.

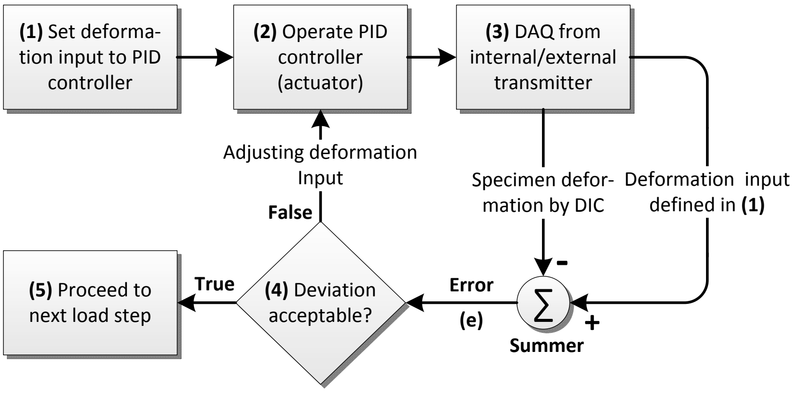
(1) Set deformation input to PID controller
(2) Operate PID controller (actuator)
(3) DAQ from internal/external transmitter
Adjusting deformation Input
False
Specimen deformation by DIC
Deformation input defined in **(1)**
-
(5) Proceed to next load step
True
(4) Deviation acceptable?
Error (e)
Σ
+
Summer

Figure 3: Dataflow in the closed single input-single output control loop (Part B)

The control loop is initiated in **(1)** by prescribing a displacement input to the PID-controller. Operated by the LVDT in the actuator the piston is moved towards the end level in a monotonic motion with a predefined deformation rate by **(2)**. When the predefined displacement is reached the data from the load cell along with the signal from the DIC measuring device are acquired by **(3)**. By comparing the deformation input with the actual response of the specimen a deviation is derived. If the deviation is within a given error tolerance the control loop is ready to receive the next deformation input in **(1)**. If the deviation exceeds the error tolerance the actuator is moved in the direction necessary to reduce the error with a magnitude equal to the deviation. This is achieved by repeating the entire loop from **(2)** – **(4)** until a deviation below the error tolerance is achieved.

3 Hybrid Testing Setup

A somewhat simple multicomponent frame structure presented in Figure 4 is studied to reduce the complexity in verifying the software capabilities.

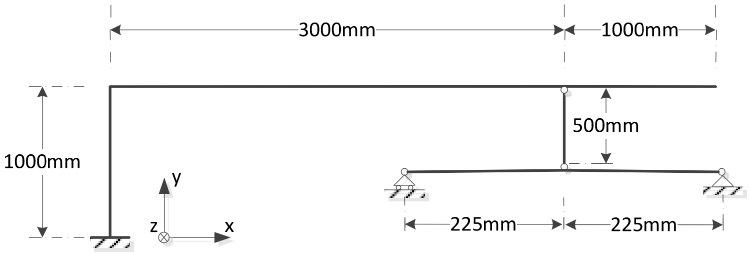
3000mm
1000mm
1000mm
500mm
y
z
x
225mm
225mm

Figure 4: Emulated structure

The emulated structure is separated in a numerical- and experimental component. Each component along with the coupling between them is illustrated in Figure 5.

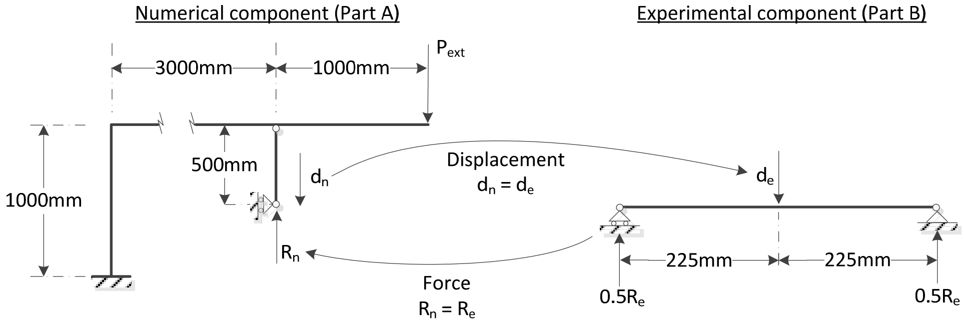
Numerical component (Part A)
Experimental component (Part B)
P_{ext}
3000mm
1000mm
500mm
1000mm
d_n
Displacement
$d_n = d_e$
d_e
R_n
Force
$R_n = R_e$
225mm
225mm
$0.5R_e$
$0.5R_e$

Figure 5: The emulated structure separated in: a) numerical component and b) experimental component

The shared boundary between the two components is defined by a discrete point with two DOFs: translation in the y- and x-direction. With the assumption of having relatively small displacements the translation in the x-direction is neglected. The global stiffness of the numerical- and experimental component named S_A and S_B respectively is defined cf. eq. (1).

$$S_A = \frac{P_{ext}}{d_n} \quad \text{and} \quad S_B = \frac{R_e}{d_e} \tag{1}$$

The global stiffness of the numerical component is 4.94 times higher than the test specimen in the shared boundary.

3.1 Experimental component (Part B)

The experimental component consists of a Glass Fibre Reinforced Polymer (GFRP) beam loaded in three point bending. The specimen has the cross sectional width and height of 45mm and 19mm respectively and includes 22 unidirectional plies of fibre mats type: L1200/G50F-E06-A from Devold AMT with a nominal area weight of 1246g/m^2. Five specimens are produced by vacuum infusion with an epoxy resin type: Airstone 760E mixed with an Airstone 776H hardener from Dow Chemicals Company. The fibre fraction is 55% [22] with the fibre mats oriented in the x-direction cf. Figure 7. The E-modulus in the direction of the fibres is by three point bending found in the range: 38.5-43.3GPa for the five specimens.

3.2 Numerical component (Part A)

The numerical component is discretized in a FE-model using an 8-node plane element with two DOFs in each node: translation in the x- and y direction. The bar connecting the numerical- and experimental component is defined by a 2-node beam element with three DOFs in each node: translation in the x- and y-direction and rotation around the z-axis. When the beam- and plane element is connected the rotation DOF is not transferred to the plane element and the charnier is thereby obtained.

4 Three point bending

The experimental component is loaded in a 4-column MTS 810 axial test station with an axial servo-hydraulic actuator model: 244.22 which provide a maximum force of ±100kN with a stroke of ±33.00mm. The actuator is operated by a servo valve model 252.24C-04 with a capacity of 10l/s. The displacement of the actuator is measured by a linear variable differential transducer (LVDT) and the force measured by an MTS load cell model 661.19E-04 with a max capacity of 25kN. The test station is operated through a MTS FlexTest 60 PID-controller. The test rig has a loading- and support nose of 40mm - and 25mm diameter respectively cf. Figure 7. The motion of the measurement points (see Figure 7) are tracked by the commercial DIC system: ARAMIS by Optical Measuring Techniques (GOM). The side of the test specimen has been applied a random speckle pattern of white background with black dots. The resolution of the DIC sensors is 4 megapixels and the lenses are type: Titanar with a 20mm focal length. The images are divided into interrogation cells of 15x15 pixels with a shift of 2 pixel. The measuring field is 330x330mm^2 calibrated with a 250x200mm^2 calibration panel. The precision and accuracy for each measurement point obtained by the DIC system is determined to an RMS of 0.002mm and 0.009mm respectively. The accuracy of the DIC setup is evaluated by a micrometer of the type: Mitutoyo - series 164 in the range 0-50mm. The full setup of the test station including: specimen mounted in the three point bending rig and DIC camera is presented in Figure 7.

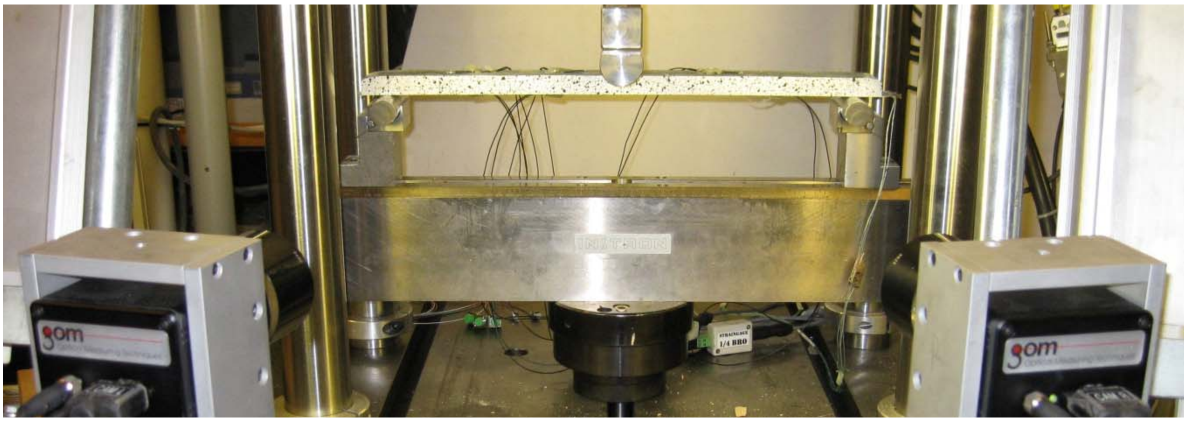

Figure 6: The three point bending setup with GFRP beam and speckle pattern

The position and numbering of the DIC measurement points along with the overall dimension of the specimen and three point bending setup is presented in Figure 7.

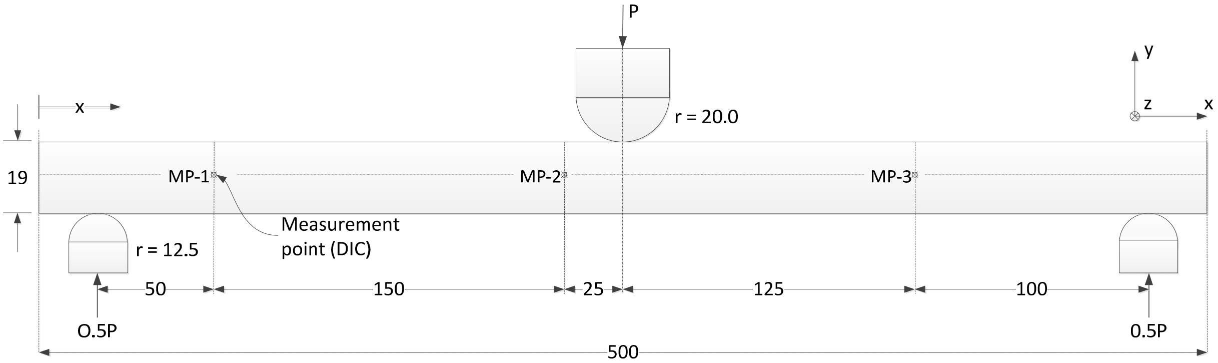

Figure 7: Dimensions of test setup and specimen along with numbering and location of DIC measurement points

5 Test result

Five GFRP specimens are tested in a quasi-static multi-component hybrid testing setup presented in Figure 5. With the hydraulic actuator operated by a feedback signal acquired on the experimental substructure by DIC an error tolerance of 0.01mm is obtained cf. Figure 3. The system is loaded within the linear elastic regime by an external force P_{ext} in increments of 900N ranging from 0 to 18kN. The equivalent vertical displacement of the shared boundary is 0 to 6mm.

5.1 Hybrid Test

The hybrid test is verified by comparing the structural response in three simulations: hybrid test, full FE-model and analytical hybrid test. In the hybrid test, Part A in Figure 5 is modelled numerically and Part B is tested experimentally. In the full FE-model, Part A and B are both modelled numerically cf. figure 4. Here, the experimental component is assigned the same bending stiffness as found from a three point bending test, cf. chapter 3.1. In the analytical hybrid test Part A is modelled numerically and Part B is calculated analytically by Bernoulli-Euler theory. Here, the bending stiffness is the same as found in chapter 3.1. For test specimen four the deformation of the sheared boundary is presented as a function of the external force P_{ext} in figure 8a. To evaluate the deviation between the three simulations the discrepancy between the hybrid test, full FE-model and analytical hybrid test is presented in Figure 8b. The load step frequency of the hybrid testing loop in figure 1is 0.09Hz

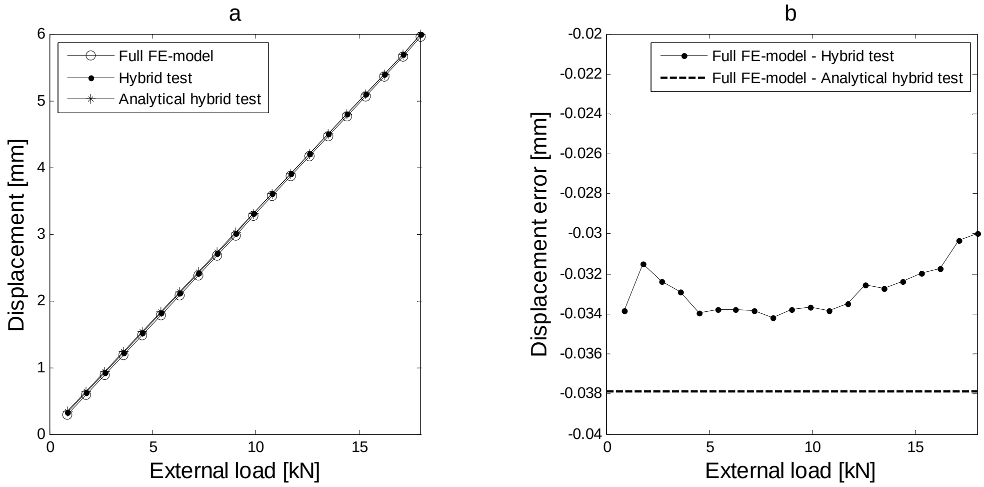

Figure 8: **a) load – deformation relation at the loading point and b) discrepancy between the response of the full FE-model and hybrid test**

From Figure 8, good correlation between the three simulations is achieved. A displacement error of 0.038mm between the full FE-model and analytical hybrid test is observed cf. figure 8b. This deviation is due to the restoring force in the hybrid test being one load step behind the numerical simulation of the full structure. The maximum discrepancy between the full FE-model and hybrid test is found to 0.034mm cf. figure 8b. Here the deviation is caused by both the restoring force in the hybrid test being one load step behind the numerical simulation of the full structure along with other sources of error in the experimental component. The discrepancy between the full FE-model and hybrid test named displacement error (hybrid) and full FE-model and analytical hybrid test named displacement error (FEM) are presented in Table 1 for the remaining four specimens.

Table 1: Displacement- and relatively error for test specimen 1 to 5

Beam number [-]	Displacement Error (FEM) [mm]	Relatively error [%]	Displacement Error (Hybrid) [mm]	Relatively error [%]
1	0.048	0.83	0.042	0.72
2	0.044	0.75	0.038	0.65
3	0.043	0.74	0.038	0.64
4	0.038	0.64	0.034	0.57
5	0.047	0.81	0.041	0.69

The relative error for each displacement error is given with respect to the total displacement of the shared boundary.

5.2 Test of Stability

The stability of the hybrid testing communication loop is affected by the ratio of the global stiffness in the shared boundary for the numerical- and experimental substructure, named S_A and S_B respectively, cf. eq. (1). For this reason a parametric study of the stiffness ratio between the experimental- and numerical substructure is performed. In this study the numerical component (part A, Figure 5) is defined in a FE-model while the response of the experimental component (part B, Figure 5) is calculated analytically from a Bernoulli-Euler assumption. The response at the shared boundary as a function of the external load P_{ext} is presented in Figure 9.

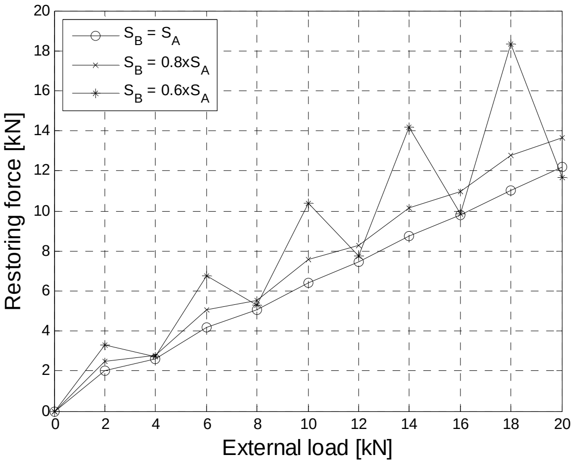

Figure 9: Restoring force in the shared boundary as a function of the external load

From Figure 9, the restoring force in the shared boundary become unstable when $S_A < S_B$. The instability is amplified when the ratio between S_A and S_B is increased. The phenomenon is avoided when the global stiffness of the numerical model is equal or higher than the experimental specimen ($S_A \geq S_B$). In the hybrid test performed in this paper the stiffness of the numerical substructure S_A is 4.94 times higher than the stiffness of the experimental substructure S_B. The hybrid loop is therefore stable. If the hybrid testing communication loop was inverted meaning that: the numerical- and experimental substructure receives a deformation- and force input respectively, instability is avoided if ($S_A \leq S_B$).

6 Discussion

Some discrepancies between the hybrid test and full FE-model was observed cf. Figure 8 and Table 1. This discrepancy is primarily due to the restoring force in the hybrid test being one load step behind the numerical simulation of the full structure cf. Table 1. This results in the overall structure displaying a lower stiffness than in the full finite element simulation. This source of error can be minimized by decreasing the size of the load step. It could also be minimized by predicting a restoring force. However, the efficiency of this method is dependent on the material behaviour of the specimen. In this study, the specimen was linear elastic making it easy to predict. However, if the test was performed on a specimen with non-linear behaviour e.g. plasticity, buckling etc. the response is harder to estimate. This is usually the case when doing hybrid testing, since the benefit of the method is that a part of a structure displaying unpredictable response can be analysed without testing the full structure [5].

The stability of the algorithm was investigated for different stiffness ratios between the numerical model and experimental structure. It was found that the hybrid test was stable when the stiffness of the numerical model was stiffer than the physical specimen, $S_A > S_B$. It was also shown that if the hybrid testing communication loop is inverted (see Figure 5) the opposite was the case. This is in general not an issue in hybrid testing, since tests are usually performed on large structures with high stiffness compared to the structural component of interest;

cf. seismic testing of dampers in buildings [4], [9], [10]. However, one must consider this issue when applying hybrid testing to other types of systems, where the experimental substructure has stiffness higher than, or close to the numerical model. This issue could be addressed by predicting a restoring force for the next load step.

DIC was in this research implemented as a technique to acquire coordinates of three measurement points along the test specimen surface cf. Figure 7. By implementing these measurements in a control loop (see Figure 3) the source of error being slack and deformations in the load train is neglected [23] [24]. Other essential data for handling of the coupling between the substructural parts could include e.g. strain measurements [25]. This could be done on the specimen surface by full field measurements, strain gauges, etc. The GFRP specimen also allows internal strain measurements by Fibre Bragg Gratings (FBG) to include stress concentrations and residual stresses in the specimen [22].

7 Conclusion

A hybrid test was performed and the response compared to a finite element simulation of the full structure. The comparison showed a small deviation primarily caused by the restoring force in the hybrid test being one load step behind the numerical simulation of the full structure. The hybrid testing setup in this study was used to prove the functionality of the hybrid testing communication loop and implement the DIC measurements to control the actuator. In the future the hybrid testing platform will be developed to handle single component structures with more advanced geometry e.g. wind turbine blades.

8 Acknowledgement

The authors acknowledge the financial support from the Danish Centre for Composite structures and Materials for Wind Turbines (DCCSM) funded by the Danish Council for Strategic Research in Sustainable Energy and Environmental (Grant 09-067212).

9 References

[1] X. Shao, A. M. Reinhorn and M. V. Sivaselvan, “Real-Time Hybrid Simulation Using Shake Tables and Dynamic Actuators,” *Journal of Structural Engineering,* vol. 137, no. 7, pp. 748-760, 2011.

[2] O. S. Bursi, A. Gonzalez-Buelga, L. Vulcan, S. A. Neild and D. J. Wagg, “Novel coupling Rosenbrock-based algorithm for real-time dynamic substructure testing,” *Eartquake Engineering and Structural Dynamics,* vol. 37, pp. 339-360, 2008.

[3] K. Takanashi and M. Nakashima, “Japanese Activities on On-line Testing,” *Journal of Engineering Mechanics,* vol. 113, no. 7, pp. 1014-1032, 1987.

[4] C. Chen, J. M. Ricles, T. L. Karavasilis, Y. Chae and R. Sause, “Evaluation of a real-time hybrid simulation system for performance evaluation of structures with rate dependent devices subjected to seismic loading,” *Engineering Structures,* vol. 35, pp. 71-82, 2012.

[5] A. Bonelli and O. S. Bursi, “Generalized-alpha methods for seismic structural testing,” *Earthquake Engineering ad Structural Dynamics,* vol. 33, pp. 1067-1102, 2004.

[6] T. L. Karavalis, J. M. Ricles, R. Sause and C. Chen, “Experimental evaluation of the seismic performance of steel MRFs with compressed elastomer dampers using large-scale real-time hybrid simulation,” *Engineering Structures,* vol. 33, pp. 1859-1869, 2011.

[7] M. Ito, Y. Murata, K. Hoki and M. Nakashima, “Online Hybrid Test on Buildings with Stud-Type Damper Made of Slitted Steel Plates Stiffened by Wood Panels,” *Procedia Engineering,* vol. 14, pp. 567-571, 2011.

[8] A. Jacobsen, T. Hitaka and M. Nakashima, “Online test of building frame with slit-wall dampers capable of condition asessment,” *Journal of Constructional Steel Research,* vol. 66, pp. 1320-1329, 2010.

[9] Y. Z. Lin and R. E. Christenson, “Comparison of Real-time Hybrid Testing with Shake Table Test for an MR Damper Controlled Structure,” *American Control Conference,* pp. 5228-5233, 2009.

[10] J. E. Carrion, B. F. Spencer Jr. and B. M. Phillips, “Real-Time Hybrid Testing of a Semi-Actively Controlled Structure with an MR Damper,” in *American Control Conference*, Hyatt Regency Riverfront, St. Louis, MO, USA, 2009.

[11] R.-Y. Jung, P. B. Shing, E. Stauffer and B. Thoen, “Performance of a real-tme pseudodynamic test system considering nonlinear structural response,” *Earthquake Engineering and Structural Dynamics,* vol. 36, pp. 1785-1809, 2007.

[12] G. Mosqueda and M. Ahmadizadeh, “Combined implicit or explicit integration steps for hybrid simulation,” *Earthquake Engineering and Structural Dynamics,* vol. 36, pp. 2325-2343, 2007.

[13] B. Wu, G. Xu, Q. Wang and M. S. Williams, “Operator-splitting method for real-time substructure testing,” *Earthquake Engineering and Structural Dynamics,* vol. 35, pp. 293-314, 2006.

[14] M. Verma and J. Rajasankar, “Improved model for real-time substructuring testing system,” *Engineering Structures,* vol. 41, pp. 258-269, 2012.

[15] M. Nakashima and N. Masaoka, “Real-Time On-Line Test for MDOF Systems,” *Earthquake Engineering and Structural Dynamics,* vol. 28, pp. 393-420, 1999.

[16] C. Chen, J. M. Ricles, T. M. Marullo and O. Mercan, “Real-time hybrid testing using unconditionally stable explicit CR integration algorithm,” *Earthquake Engineering and Structural Dynamics,* vol. 38, pp. 23-44, 2009.

[17] J. Waldbjørn, J. Høgh, J. Wittrup-Schmidt, M. Nielsen, K. Branner, H. Stang and C. Berggreen, “Strain and Deformation Control by Fibre Bragg Grating and Digital Image Correlation,” *Strain,* (to be submitted).

[18] R. Bitter, T. Mohiuddin and M. Nawrocki, LabView Advanced Programming Techniques, Boca Rotan, Florida, USA: CRC Press, 2001.

[19] MTS, “MTS Systems Corporation, FlexTest Controllers,” MTS Systems Corporation, 8 Oktober 2011.

[Online]. Available: https://www.mts.com. [Accessed 8 Oktober 2011].

[20] MTS, LabVIEW Programming Libraries: Model 793.00 Software, MTS Systems Corporation, 2009.

[21] GOM, ARAMIS - User Manual - Software, Braunschweig, Germany: GOM, 2006.

[22] M. W. Nielsen, J. Wittrup-Schmidt, J. Hattel, J. H. Høgh, J. P. Waldbjørn, J. Andersen and T. L. Markussen, "In-situ measurements using FBGs of process-induced strains during curing of thick glass/epoxy laminate plate: Experimental results and Numerical modeling," *Composites.*

[23] X. Fayolle, S. Galloch and F. Hild, "Controlling Testing Machines with Digital Image Correlation," *Experimental Techniques,* vol. 31, no. 3, pp. 57-63, 2007.

[24] J. Waldbjørn, J. Høgh, J. Wittrup-Schmidt, M. Nielsen, K. Branner, H. Stang and C. Berggreen, "Strain and Deformation Control by Fibre Bragg Grating and Digital Image Correlation," *Strain,* 2013.

[25] U. C. Mueller, T. Zeh, A. W. Koch and H. Baier, "Fiber Optic Bragg Grating Sensors for High-Precision Structural Deformation Control in Optical Systems," *SPIE,* vol. 6167, 2006.

strain
An International Journal for Experimental Mechanics

Quasi-Static Single-Component Hybrid Simulation of a Composite Structure with Multi-Axis Control

J. Høgh*, J. Waldbjørn†, J. Wittrup-Schmidt†, H. Stang† and C. Berggreen*

*Department of Mechanical Engineering, Technical University of Denmark, Kgs. Lyngby, Denmark
†Department of Civil Engineering, Technical University of Denmark, Kgs. Lyngby, Denmark

Abstract: This paper presents a quasi-static hybrid simulation performed on a single component structure. Hybrid simulation is a substructural technique, where a structure is divided into two sections: a numerical section of the main structure and a physical experiment of the remainder. In previous cases, hybrid simulation has typically been applied to structures with a simple connection between the numerical model and physical test, e.g. civil engineering structures. In this paper, the method is applied to a composite structure, where the boundary is more complex i.e. 3 degrees of freedom. In order to evaluate the validity of the method, the results are compared to a test of the emulated structure – referred to here as the reference test. It was found that the error introduced by compliance in the load train was significant. Digital image correlation was for this reason implemented in the hybrid simulation communication loop to compensate for this source of error. Furthermore, the accuracy of the hybrid simulation was improved by compensating for communication delay. The test showed high correspondence between the hybrid simulation and the reference test in terms of overall deflection as well as displacements and rotation in the shared boundary.

KEY WORDS: *composite structure, high-precision control, multi-axial control, single-component hybrid simulation, substructural testing*

Introduction

The ambition to improve the structural and operational performance of large structures within the industry of wind energy [1] has resulted in extensive research regarding large scale- and high performance composite structures. In these efforts, testing has primary been focusing on two scales: full scale and coupon testing [2]. Full scale testing provides valuable knowledge of the structural behaviour but is time consuming and expensive to perform due to the large scale of the structure [1]. The structure is typically tested in simple load configuration which is a significant simplification of the actual loads to which the structure is exposed during service. In order to investigate the material characteristics of the individual materials in the composite structure, coupon testing is conducted [3]. Such tests are performed on specially designed specimens, resulting in idealised stress- and strain states, and as a consequence, they do not account for the complex stress states and interactions between the different materials in the joints, bearings and other critical details throughout the structure.

To address shortcomings in full scale and material testing within the industry of wind energy, the hybrid simulation concept is introduced as a sub-modelling technique. For an SSP34m wind turbine blade (SSP Technology, Stenstrup, Denmark), the 0–13 m segment was identified as the critical section of interest [1, 2]. For that reason, the hybrid simulation concept could be implemented as an alternative to full-scale testing – providing the capability to isolate and experimentally test that section for which a reliable model may not be available. The remainder of the emulated structure is assumed to be well understood and is for that reason handled in a numerical model – capable of handling advanced load cases covering both static and dynamic effects. As a consequence, neither cost-intensive full-scale experiments nor demanding theoretical evaluation procedure is required to reveal the response of the experimental substructure, when exposed to the effect of the remaining structure. The coupling between the numerical and experimental substructure is governed through the interface between the two components referred to here as the shared boundary. During the test, a pre-defined external displacement is applied to the numerical substructure which is equivalent to the loads acting on the structure during service. The corresponding response is computed through a commercial finite element (FE) software and imposed on the experimental substructure using actuators. The forces required to deform the experimental substructure – referred to here as the restoring force – are retrieved and fed back to the numerical substructure to compute the next displacement corresponding to the next time step. This communication is established through an algorithm, referred to here as the hybrid simulation communication loop.

The hybrid simulation technique originated in the late 1960’s, where it was used for simulation of the structural response to an earthquake as an alternative to shake table test [4]. Since then, the research within hybrid simulation has mainly been focused on seismic protection of building structures [5, 6]. Here, the numerical and experimental substructure has been two separate – typically simply connected – structural components referred to here as multi-component hybrid simulation. For this application, the load bearing structure has been simulated

© 2015 Wiley Publishing Ltd
doi: 10.1111/str.12157

in a numerical model, while damping fixtures has been tested experimentally e.g. elastomer [7], stud types [8, 9] and magneto-rheological [10, 11]. However, to close the gap between full scale and material testing within the industry of wind energy, the hybrid simulation concept is implemented for a single component structure – referred to here as single component hybrid simulation. This concept only deviates from the traditional multi-component hybrid simulation by the complexity of the shared boundary which for the single component hybrid simulation consists of an edge instead of e.g. a clearly defined hinge as presented in [12, 13]. This comprises an infinite number of contact points yielding a complex force/displacement distribution in the coupling between the two substructures. The operation of the shared boundary justifies the need for advanced measuring techniques to ensure a high degree of accuracy in the displacement imposed on the shared boundary of the experimental substructure [14, 15]. To the author's knowledge, only a single publication is published concerning single-component hybrid simulation [16]. Here, the concept is introduced, and the system demonstrated on a composite beam with the shared boundary covering a discrete point with a single degrees-of-freedom (DOF).

The scope of this paper is to perform a single-component hybrid simulation – here with special attention paid to the operation of the shared boundary between the numerical and experimental substructure. The emulated structure consists of a composite beam, clamped in both ends and loaded by a single point load. The shared boundary is described as a discrete point with three DOF. Digital image correlation (DIC) is implemented as a method of adjusting the quasi-static imposed displacements on the shared boundary, to fit the command signal received by the numerical model – referred to here as a *DIC compensator*. Furthermore, compensation of communication delay is conducted through linear regression – referred to here as a *communication delay compensator*. A parametric study is conducted where the effect of DIC compensation and communication delay compensation is investigated. Finally, the optimal configuration of these two parameters is identified and demonstrated on an applied case. For verification of the single-component hybrid simulation technique, a test of the emulated structure is conducted – referred to here as the reference test. Here, a point load is applied to the specimen and the global response monitored in multiple measurement point (MP) to compare with the global response of the hybrid simulation.

Hybrid simulation setup

The reference structure consists of a beam which is clamped in both ends and loaded by an external displacement D_{ext} cf. Figure 1. This configuration is studied to reduce the complexity in verifying the hybrid simulation communication loop capabilities and operation of the shared boundary. The material properties of the reference structure are determined by coupon testing cf. Table 1.

The reference structure is separated in a numerical- and experimental substructure. Two slits are located in the compression flange to yield a geometrical non-linear response of the experimental substructure due to buckling, cf. Figure 1. Each substructure along with the coupling between them is illustrated in Figure 2.

The shared boundary between the two substructures is defined by a discrete point with three DOF: translation in the x- and y-direction along with rotation around the z-axis – referred to here as f.

Experimental substructure (section A)

The experimental substructure consists of a 648-mm long thin-walled glass fibre reinforced polymer (GFRP) beam produced by Fibre Pultrusion. The closed rectangular cross section has a width and height of 140 mm and 60 mm, respectively, while the corresponding material thickness is 5 mm and 6 mm cf. Figure 1. Two slits at the centre of the compression flange are initiated in order to include non-linear behaviour. These slits are located 112 mm from each other, each with a length and width of 240 and 4 mm, respectively. The experimental substructure is loaded as a cantilever beam, with the free edge as the shared boundary between the two substructures cf. Figure 2. The in-plane material properties of the tensile/compression flange are presented in Table 1, determined in accordance with D3039/D3039M–08 [17] and D5379/D5379M–12 [18].

The tensile stress–strain relation in both the 1- and 2-direction is demonstrated linear elastic until failure. For the longitudinal tensile specimen, a clear relation between the laminate stiffness and position in the width of the tension/compression flange (2-direction) is observed. The lowest stiffness is found at the centre of the tensile/compression flange while increasing when moving towards the corner of the cross section. This tendency is most likely caused by variances in the fibre content along the width of the tension/compression flange. The 1-direction is the first in-plane direction, corresponding to the x-direction in Figure 2. The 2-direction corresponds to the second in-plane direction (2-direction corresponds to the z-direction for the flanges and y-direction for the sides in Figure 2).

The specimen is in both ends clamped to the rig through a rectangular steel profile cf. Figure 5. Installation plates of steel are positioned on each side of the test specimen for supporting and to avoid critical stress concentrations in the interface between the test specimen and rectangular steel profile. Everything is tightened together by 18 bolts to establish a stiff friction connection between the rectangular steel profile and test specimen, see Figure 3.

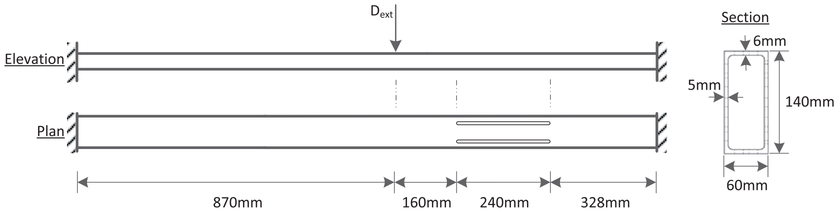
D_{ext}
Elevation
Plan
Section
6mm
5mm
140mm
60mm
870mm
160mm
240mm
328mm

Figure 1: Reference structure representing the overall dimensions, external displacement and boundary conditions

Table 1: In-plane tensile moduli, shear modulus and Poisson's ratio

Specimen [-]	E_1 [GPa]	E_2 [GPa]	ν_{12} [-]	ν_{21} [-]	G_{12} [GPa]	G_{21} [GPa]
1	34.79	10.09	0.23	0.07	3.49	3.10
2	25.48	9.24	0.23	0.08	3.64	2.75
3	21.68	9.31	0.22	0.09	3.56	3.03
4	20.89	10.17	0.21	0.07	3.18	3.38
5	23.65	10.52	0.24	0.09	3.59	2.85
6	32.41	9.91	0.22	0.07	3.08	3.25
7	39.63	10.49	0.25	0.08	3.39	–
8	–	–	–	–	3.33	–
Average	28.36	9.96	0.23	0.08	3.41	3.06
Standard deviation	7.25	0.52	0.01	0.01	0.20	0.24
Coefficient of variance [%]	25.57	5.18	5.89	11.45	5.90	7.75

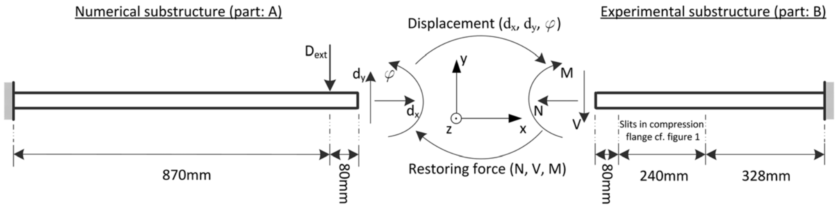
Numerical substructure (part: A)
Displacement (dx, dy, φ)
Experimental substructure (part: B)
Dext
dy
φ
dx
y
z
x
M
N
V
Slits in compression flange cf. figure 1
870mm
80mm
Restoring force (N, V, M)
80mm
240mm
328mm

Figure 2: The reference structure separated in: (A) numerical substructure and (B) experimental substructure

Numerical substructure (section B)

The numerical substructure is simulated in ANSYS 15.0 (ANSYS, Inc, Canonsburg, PA, USA) in a three-dimensional (3D) FE-model, using isoparametric quadrilateral eight-node shell elements of the type: shell281 [19], with a Reissner–Mindlin formulation for the displacement field. Each side of the shell element includes a node in the corner and middle. These elements have six DOF in each node: translation and rotation in the *x*-, *y*-, and *z*-direction. The model has 2256 elements, and orthotropic material properties are assigned according to Table 2. The laminate is assumed transversely isotropic hence G13 = G12, G12 = G21, G13 = G31 and G23 = G32. The G23 has negligible effect on in-plane stiffness and therefore set equal to G12 for simplicity. The same assumption is made for the Poisson's ratio.

The external displacement is applied to the numerical structure as a nodal displacement along a line 870 mm from the clamped support, cf. Figure 1.

The restoring force is applied to the structure at the position of 950 mm from the support, cf. Figure 2. The vertical- and horizontal forces and moment are applied as nodal loads. The nodal loads are distributed statically and work equivalent to the uniformly distributed forces and moments in the structure.

The clamped supports of the FE model are designed as presented in Figure 4 with a width, height and thickness of 160 × 280 × 10 mm and isotropic material properties.

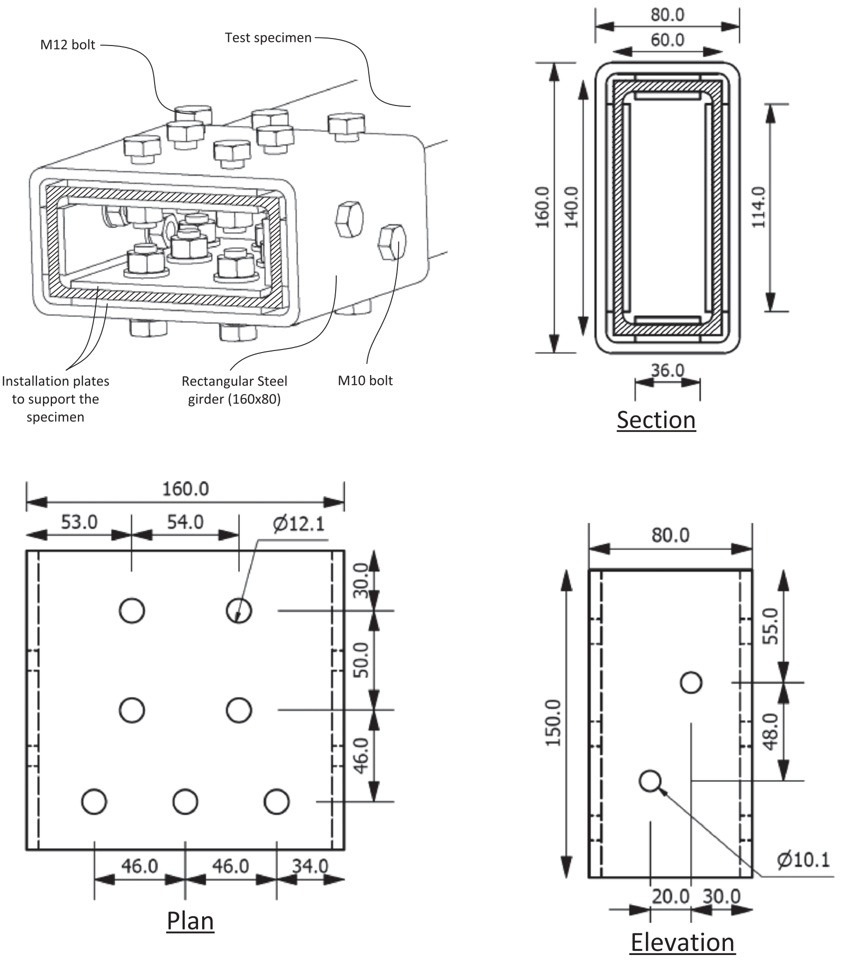
M12 bolt
Test specimen
Installation plates to support the specimen
Rectangular Steel girder (160x80)
M10 bolt
80.0
60.0
160.0
140.0
114.0
36.0
Section
160.0
53.0
54.0
Ø12.1
30.0
50.0
46.0
46.0
46.0
34.0
Plan
80.0
150.0
55.0
48.0
Ø10.1
20.0
30.0
Elevation

Figure 3: Clamped support of the experimental substructure displaying plan, section and elevation view

Table 2: Orthotropic material properties used in the finite element model

E_x [GPa]	E_y [GPa]	E_z [GPa]	G_{xy} [GPa]	G_{yz} [GPa]	G_{xz} [GPa]	υ_{xy} [-]	υ_{yz} [-]	υ_{xz} [-]
28.36	9.96	9.96	3.235	3.235	3.235	0.155	0.155	0.155

To ensure an identical stiffness of the numerical and experimental clamped support, an FE model of the reference structure is created. Here, the Young's modulus, *E*, of the support in the FE model is adjusted to fit the root rotation of the composite beam measured in the test of the reference structure. This rotation is measured by DIC in MPs 12, 13 and 14 cf. Figure 7. The correct rotation occurred with a Young's modulus of 170 GPa.

Experimental test setup

The experimental test setup is handled in a suitably stiff frame structure, re-configurable to handle both the reference test, see Figure 7, and experimental substructure of the hybrid simulation, see Figure 5. Fabricated steel interface plates are mounted to the frame structure to accommodate the swivel base of up to three servo-hydraulic actuators named A, B and C. Actuator A is an Material Testing Systems (MTS) model: 244.12 which provide a force capacity of ±25 kN with a static and dynamic stroke of 182.9 mm and 152.4 mm, respectively. The actuator is operated by a servo valve model: MTS 252.23G-01 with a capacity of 19 L min^{-1}. The displacement of the actuator is monitored by a linear variable differential transducer (LVDT) and the force measured by an MTS load cell model: 661.19E-04 with a capacity of ±25 kN. Actuators B and C are

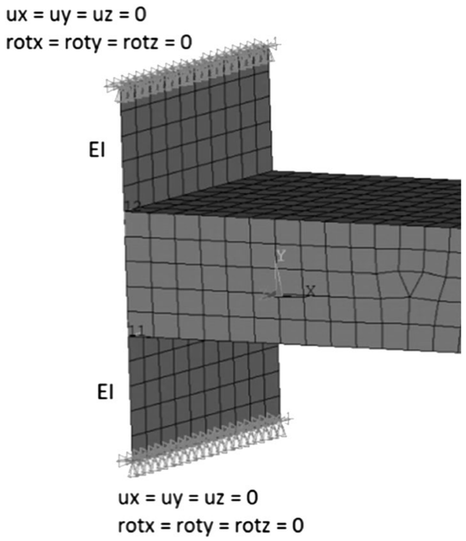

Figure 4: The clamped support of the finite element model

an MTS model: 242.01 which provide a force capacity of ±5 kN with a static and dynamic stroke of 114.3 and 101.6 mm, respectively. The actuator is operated by a servo valve model: MTS 252.21G-01 with a capacity of 4 L min^{-1}. The displacement of the actuator is monitored by an LVDT and the force measured by an MTS load cell model: 661.19E-01 with a capacity of ±5 kN. The actuators are operated through an MTS TestStar II proportional-integral-derivative (PID) – controller with a three-channel configuration. The system is connected to a hydraulic power unit operating at 3000 psi pressure.

Experimental substructure of the hybrid simulation

The experimental substructure of the hybrid simulation consists of the cantilever GFRP beam loaded in the stiff frame structure, described above, by three actuators A, B and C cf. Figure 5. The response of the GFRP beam is monitored on both sides by two individual 3D – DIC systems named: DIC 1 and DIC 2. The camera setup and performance of the DIC system are presented in Table 3.

From the DIC measurements, the displacement of the shared boundary and remainder of the experimental substructure are tracked through five MPs on each side cf. Figure 5. Given that the MPs for DIC 1 are tracked real-time, no full field data is available from this system, due to software limitations. Both sides of the GFRP beam applied a high contrast by a random speckle pattern of white background with black dots. The surface is illuminated with an even and high intensity. The compression and tension flanges are monitored through three strain gauge measurements (SGs) on each side cf. Figure 5. The electrical strain gauges are of the type SR-4 general purpose strain gauges from Vishay Micro-Measurements (951 Wendell Blvd., Wendell, NC 27591, USA).

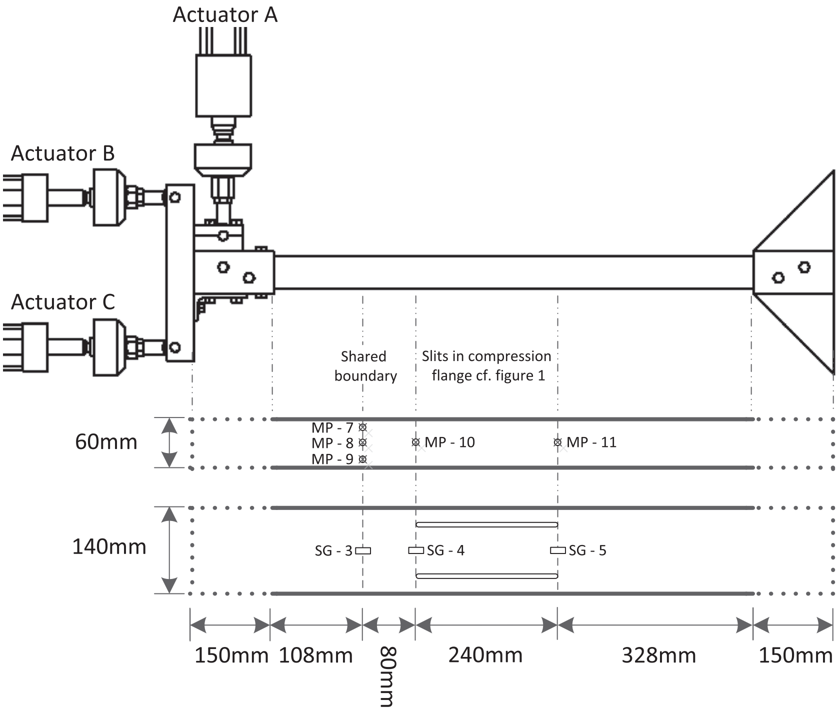

Figure 5: Experimental substructure including test rig and specimen with measurement point (MP) and strain gauge measurement (SG)

Table 3: Setup and performance of the 3D-DIC system

	Hybrid simulation		Reference test	
Configuration label	DIC 1	DIC 2	DIC 3	DIC 4
Side of beam	1	2	1	2
Technique used	3D image correlation	3D image correlation	3D image correlation	3D image correlation
Subset	20 pixel	20 pixel	20 pixel	20 pixel
Shift	13 pixel	13 pixel	13 pixel	13 pixel
Camera	4M 1 in CCD chip	2M 2/3 in CCD chip	4M 1 in CCD chip	2M 2/3 in CCD chip
Lens	20 mm	8 mm	20 mm	8 mm
Field of view	960 mm × 960 mm 2048 × 2048 pixel	590 mm × 590 mm 1600 × 1200 pixel	960 mm × 960 mm 2048 × 2048 pixel	590 mm × 590 mm 1600 × 1200 pixel
Measurement points	24 818	11 360	24 818	11 360
Displacement				
Spatial resolution	20 pixel	20 pixel	20 pixel	20 pixel
Resolution, σ standard deviation				
In-plane	5.1 μm × 3.5 μm	6.6 μm × 3.4 μm	4.1 μm × 3.4 μm	5.6 μm × 3.2 μm
Out-of-plane	21.7 μm	17.2 μm	17.8 μm	17.0 μm

3D-DIC, three-dimensional-digital image correlation; CCD, charge-coupled device.

The gauge resistance is 120.0 Ω ± 0.3% and gauge length 6.00 mm with a gauge factor of 2.075 ± 0.5% for all specimens. The test configuration along with position and numbering of the DIC and SG is presented in Figure 5.

The three DOF of the shared boundary is monitored through three MPs named: MP 7, MP 8 and MP 9 cf. Figure 5. The shared boundary is located 108 mm from the rectangular steel profile to erase any strain concentrations initiated by the clamped support. A numerical analysis of the setup verified that the concentrations were diminished for a load introduction zone longer than 100 mm. Through DIC compensation, the quasi-static imposed displacements at the shared boundary are adjusted to fit the command signal received by the numerical model [14]. The full setup of the test configuration including hydraulic actuators, specimen mounted in the test rig, strain gauges and DIC camera is presented in Figure 6.

Reference test

The reference test consists of the GFRP beam, cf. Figure 1, which is clamped in both ends and loaded in the stiff frame structure described above, by the servo-hydraulic actuator A cf. Figure 7. The response of the GFRP is likewise monitored on both sides by two individual 3D – DIC systems named: DIC 3 and DIC 4. The camera setup and performance of the DIC system are presented in Table 3. From the DIC measurements, the displacement of the shared boundary and remainder of the reference structure are tracked through 14 MPs on each side cf. Figure 7. The compression and tension flanges are monitored through five SGs on each side cf. Figure 7. The electrical strain gauges are of the same type and specifications as the ones used in the experimental substructure of the hybrid simulation. The full test configuration along with position and numbering of the DIC and SG is presented in Figure 7.

The specimen is in both ends clamped cf. Figure 7. Details of the clamping support are given in Figure 3. The full setup of the test configuration including the hydraulic actuator, specimen mounted in the test rig and DIC camera is presented in Figure 8.

Hybrid simulation communication loop

The quasi-static hybrid simulation communication loop provides the capability to experimentally test a substructure of interest while simulating the remainder in a numerical model on an extended time scale. The software is partitioned in a numerical and experimental portion, connected through a digital to analogue–analogue to digital interface. The software is operated in a producer/consumer architecture [20] through LabVIEW 13.0. The outline of the dataflow in the hybrid simulation communication loop is presented in Figure 9.

The interface between the numerical and experimental substructure is generated through a NI9205 and NI9263 LabVIEW board. Product specifications including accuracy and precision are stated in [21] and [22].

An external displacement is applied to the numerical FE-model **(1)** further clarified in Figure 2. The FE-model is defined by the ANSYS parametric design language (APDL-script) and executed in batch mode through the Windows command prompt. The displacement $\underline{d}_{com}(i)$ at the shared boundary for the current load step, i, is extracted in three DOF: translation in the x- and y-direction along with rotation around the z-axis, cf. Figure 2 and Equation [2].

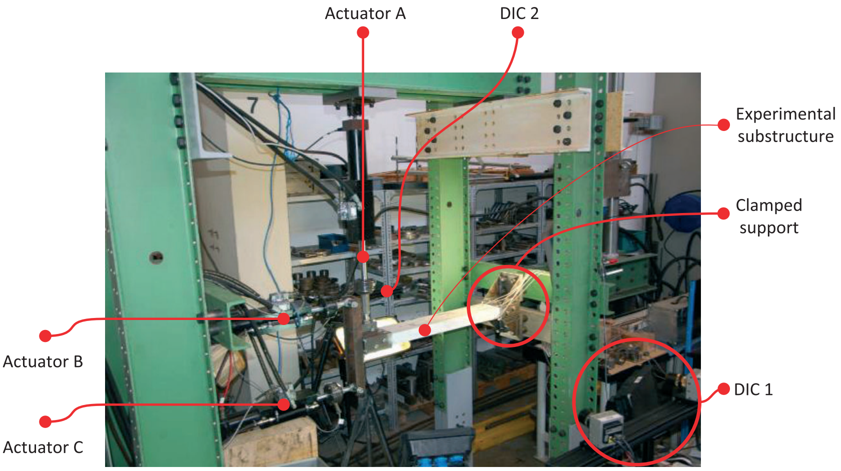
Actuator A
DIC 2
Experimental substructure
Clamped support
Actuator B
DIC 1
Actuator C

Figure 6: The multi-axial single-component hybrid simulation setup with glass fibre reinforced polymer beam, strain gauges and speckle pattern. DIC, digital image correlation

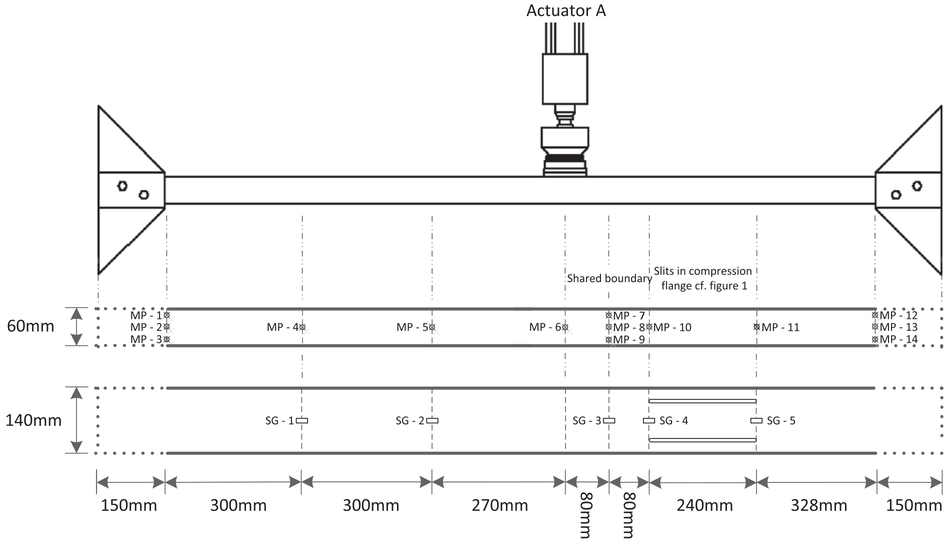
Actuator A
Shared boundary
Slits in compression flange cf. figure 1
60mm
MP - 1
MP - 2
MP - 3
MP - 4
MP - 5
MP - 6
MP - 7
MP - 8
MP - 9
MP - 10
MP - 11
MP - 12
MP - 13
MP - 14
140mm
SG - 1
SG - 2
SG - 3
SG - 4
SG - 5
150mm
300mm
300mm
270mm
80mm
80mm
240mm
328mm
150mm

Figure 7: The test of the reference structure including test rig and specimen with measurement points (MPs)

To eliminate the effect of compliance in the load train, a *DIC compensator* is applied. The in-plane displacement of the shared boundary is tracked by DIC in **(2)** through three MPs named: MP7, MP8 and MP9 cf. Figure 5. The measured displacement is compared with the previous displacement $\underline{d}_{com}(i-1)$ and the deviation, $\underline{d}_{err}(i)$, derived in Equation [3]. This deviation is added to $\underline{d}_{num}(i)$ to find the compensated displacement at the current load step $\underline{d}_{com}(i)$, Equation [4]. $\underline{d}_{num}(i)$, $\underline{d}_{com}(i)$ and $\underline{d}_{err}(i)$ contains x- and y-translation and z-rotation in the format of Equation [2]. This compensator is similar to the one used in [14] except here; only the subsequent command signal is updated instead of iterating several times for every step. The corresponding displacement of actuators A, B and C, $\underline{d}_{act}(i)$ Equation [1] is derived through a trigonometric algorithm following the assumption of rigid body motion in **(3)**.

$$\underline{d}_{act}(i) = [d_A(i)\ d_B(i)\ d_C(i)] \tag{1}$$

$$\underline{d}(i) = [d_x(i)\ d_y(i)\ \varphi(i)] \tag{2}$$

$$\underline{d}_{err}(i) = d_{com}(i-1) - d_{num}(i-1) \tag{3}$$

$$\underline{d}_{com}(i) = \underline{d}_{num}(i) + \underline{d}_{err}(i) \tag{4}$$

In **(3)** Figure 9, the coordinates of actuators A, B and C loading points to the i'th step ($x_m(i)$ and $y_m(i)$) are found by superposition of the translational displacement, $d_x(i)$ and $d_y(i)$, and the position from the rotational contribution,

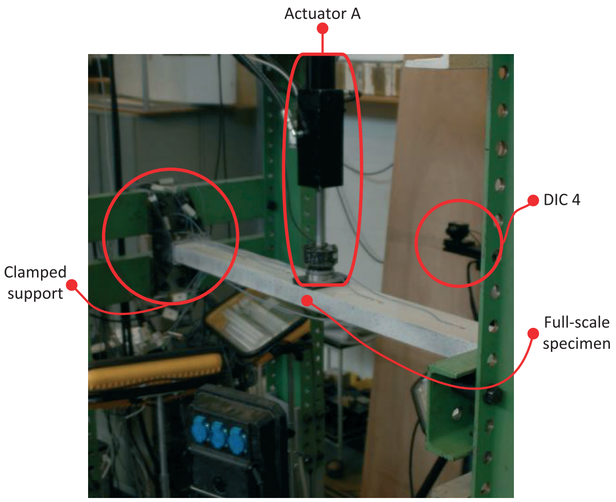
Actuator A
DIC 4
Clamped support
Full-scale specimen

Figure 8: The reference test with glass fibre reinforced polymer beam, strain gauges and speckle pattern. DIC, digital image correlation

$x_{m,\varphi}$ and $y_{m,\varphi}$, assuming rigid body motion of the test rig, cf. Equations (5)–(6). The m denotes the actuators A, B or C.

$$x_m(i) = x_{m,\varphi}(i) + d_x(i) \text{ for } m \;=\; \text{A, B, C} \tag{5}$$

$$y_m(i) = y_{m,\varphi}(i) + d_y(i) \text{ for } m = \;\text{A, B, C} \tag{6}$$

The rotational contribution to the translation, $x_{m,\varphi}$ and $y_{m,\varphi}$, is found by a trigonometric relation between the rotation of the shared boundary, φ, and the actuator loading point position in the previous load step, $x_m(i-1)$ and $y_m(i-1)$, cf. Equations (7)–(8). Here, r_m, is the distance from the shared boundary to the actuator loading point, cf. Figure 10.

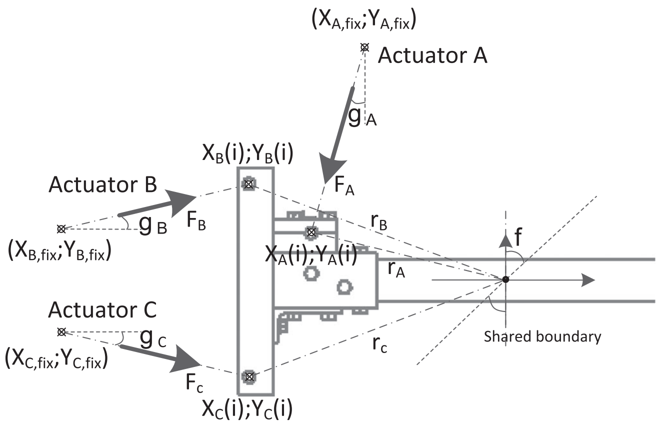
$(X_{A,fix};Y_{A,fix})$
Actuator A
g_A
$X_B(i);Y_B(i)$
Actuator B
F_A
g_B
F_B
r_B
f
$(X_{B,fix};Y_{B,fix})$
$X_A(i);Y_A(i)$
r_A
Actuator C
Shared boundary
g_C
r_C
$(X_{C,fix};Y_{C,fix})$
F_C
$X_C(i);Y_C(i)$

Figure 10: Notation for the calculation of the actuators A, B and C displacements

$$x_{m,\varphi}(i) = r_m \cos\left(\arccos\left(\frac{x_m(i-1)}{r_m}\right) + \varphi\right) \text{ for } m = \text{A, B, C} \tag{7}$$

$$y_{m,\varphi}(i) = r_m \sin\left(\arcsin\left(\frac{y_m(i-1)}{r_m}\right) + \varphi\right) \text{ for } m = \text{A, B, C} \tag{8}$$

The actuator displacement in load step i, $\underline{d}_{act}(i)$, is found from the distance between the actuator fix point, $x_{m,fix}$ and $y_{m,fix}$, and actuator loading point position, $x_m(i)$ and $y_m(i)$, cf. Equation [9].

$$\underline{d}_{act}(i) = \begin{bmatrix} \sqrt{\left(x_A(i) - x_{A,fix}\right)^2 + \left(y_A(i) - y_{A,fix}\right)^2} \\ \sqrt{\left(x_B(i) - x_{B,fix}\right)^2 + \left(y_B(i) - y_{B,fix}\right)^2} \\ \sqrt{\left(x_C(i) - x_{C,fix}\right)^2 + \left(y_C(i) - y_{C,fix}\right)^2} \end{bmatrix}^T \tag{9}$$

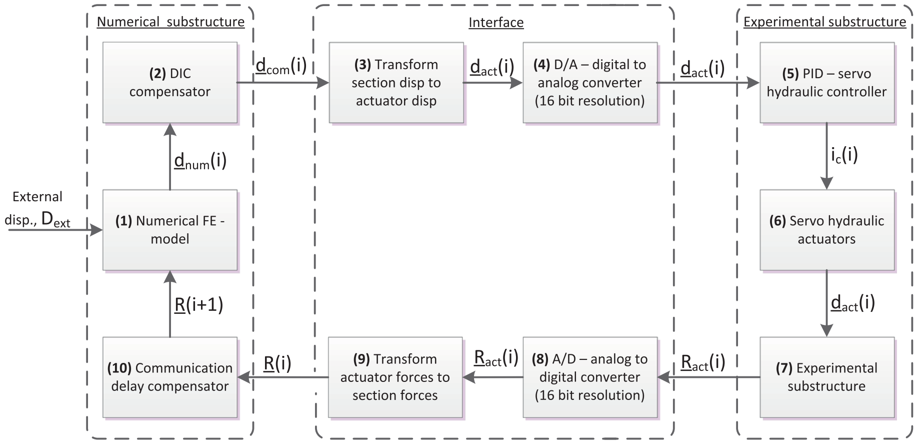
Numerical substructure
Interface
Experimental substructure
(2) DIC compensator
$\underline{d}_{com}(i)$
(3) Transform section disp to actuator disp
$\underline{d}_{act}(i)$
(4) D/A – digital to analog converter (16 bit resolution)
$\underline{d}_{act}(i)$
(5) PID – servo hydraulic controller
$\underline{d}_{num}(i)$
$\underline{i}_c(i)$
External disp., D_{ext}
(1) Numerical FE - model
(6) Servo hydraulic actuators
$\underline{R}(i+1)$
$\underline{d}_{act}(i)$
(10) Communication delay compensator
$\underline{R}(i)$
(9) Transform actuator forces to section forces
$\underline{R}_{act}(i)$
(8) A/D – analog to digital converter (16 bit resolution)
$\underline{R}_{act}(i)$
(7) Experimental substructure

Figure 9: Dataflow in the quasi-static hybrid simulation communication loop. DIC, digital image correlation; FE, finite element; PID, proportional-integral-derivative

Through **(4)**, the current compensated displacement $\underline{d}_{com}(i)$ is transferred to a digital PID controller in **(5)** operated in displacement mode. Here, an electrical command signal $\underline{i}_c(i)$ is generated and passed to the servo valves in **(6)** causing the actuator to move $\underline{d}_{act}(i)$ and apply reaction forces on the test specimen. These actuator forces $R_{act}(i)$ is obtained by load cells in **(7)** and transformed to section forces $R(i)$ through a trigonometric relation in **(9)**, assuming rigid body motion. The relation is derived from Figure 10 and presented in Equations (12)–(14).

$$\underline{R}_{act}(i) = [R_A(i)\, R_B(i)\, R_C(i)] \tag{10}$$

$$\underline{R}(i) = [R_V(i)\, R_H(i)\, M(i)] \tag{11}$$

$$R_V = R_A \cos(\gamma_A) + R_B \sin(\gamma_B) + R_C \sin(\gamma_C) \tag{12}$$

$$\begin{aligned} R_H &= R_A \sin(\gamma_A) + R_B \cos(\gamma_B) + R_C \cos(\gamma_C) \\ M &= R_A\big(\cos(\gamma_A)(x_A(i) - x(i)) + \sin(\gamma_A)\big(y(i) - y_A(i)\big)\big) \end{aligned} \tag{13}$$

$$\begin{aligned} &+R_B\big(\cos(\gamma_B)\big(y(i) - y_B(i)\big) + \sin(\gamma_B)(x_B(i) - x(i))\big) \\ &+R_C\big(\cos(\gamma_C)\big(y(i) - y_C(i)\big) + \sin(\gamma_C)(x_C(i) - x(i))\big) \end{aligned} \tag{14}$$

In a hybrid simulation, the restoring force from the experimental substructure is one step behind the numerical simulation [23] – referred to here as communication delay. This is compensated for by a *communication delay compensator*. In **(10)**, the restoring force for the upcoming load step $\underline{R}(i+1)$ is extrapolated by the three or four previous sets of external displacement D_{ext} and restoring forces $R(i)$. This extrapolation is done by a function ψ, using least-square linear regression [24]

$$\begin{aligned} R_V(i+1) = \psi(&R_V(i-n), D_{ext}(i-n), R_V(i-n+1), \\ &D_{ext}(i-n+1), \ldots,\; R_V(i), D_{ext}(i)) \text{ for } n \;=\; 3, 4 \end{aligned} \tag{15}$$

$$\begin{aligned} R_V(i+1) = \psi(&R_V(i-n), D_{ext}(i-n), R_V(i-n+1), \\ &D_{ext}(i-n+1), \ldots,\; R_V(i), D_{ext}(i)) \text{ for } n = 3, 4 \end{aligned} \tag{16}$$

$$\begin{aligned} M(i+1) = \psi(&M(i-n), D_{ext}(i-n), M(i-n+1), \\ &D_{ext}(i-n+1), \ldots,\; M(i), D_{ext}(i)) \text{ for } n = 3, 4 \end{aligned} \tag{17}$$

Test result

A GFRP beam is tested in a quasi-static single component hybrid simulation setup presented in Figure 2 and Figure 5. A test of the emulated structure is conducted for verification purposes cf. Figure 1 and Figure 7. The system is loaded with a ramped deformation pattern in the range: 0.0 mm to 6.5 mm which is equivalent to a vertical reaction force of 0.0 to 5.0 kN. The load is applied through 20, 40 and 60 steps per period cf. Figure 11 at a rate of approximately 9 s step^{-1}.

In order to verify that both the reference test and hybrid simulation setup do not introduce out-of-plane displacements e.g. twisting, both sides of the GFRP beam are monitored in the MPs stated in Table 4. In here, side 1 is monitored by DIC 1 and 3, while side 2 is monitored by DIC 2 and 4, cf. Figure 6, Figure 8 and Table 3

The numerical substructure represented in Table 4 is not considered, since no out-of-plane deformations are observed. It is noted that the out-of-plane displacements are of a magnitude equal to the measurement precision cf. Table 3 and therefore insignificant. A deviation of vertical and horizontal displacement between sides 1 and 2 is clearly identified for the hybrid simulation, probably induced by misalignment of the load train. The same effect is also identified in the reference test; however, the magnitude is significantly smaller. The deviation between the vertical and horizontal displacement of both sides of the specimen is proportional to the load.

Digital image correlation compensator

By the use of 60 steps per loading period, the difference between enabling and disabling DIC compensation is investigated, cf. Equations (1)–(4).

From Figure 12A, the displacement distribution of the hybrid simulation reveals a significant lack of bending stiffness relative to the reference test along with a discontinuity in the shared boundary of 33% due to compliance in the load train. However, when using the DIC system to compensate for these effects, the reference test and hybrid simulation correlate significantly better with a maximum deviation of 2.6% relative to the reference test cf. Figure 12B. The DIC compensator slowed the programme by 50 ms step^{-1}.

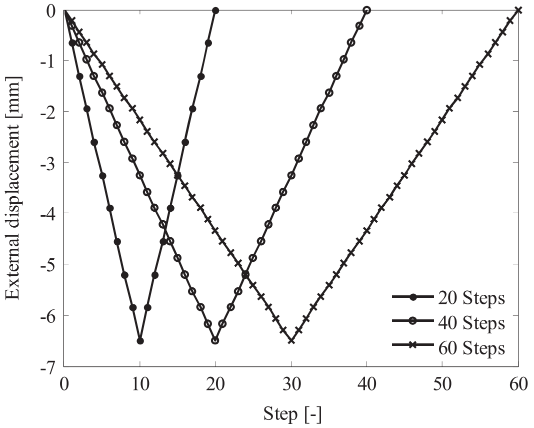

Figure 11: Ramped external displacement pattern for a single period

Table 4: Error for in-plane displacement between sides 1 and 2 and out-of-plane displacements at 5 kN

		Numerical substructure			Experimental substructure			Mean
		MP 4	MP 5	MP 6	MP 8	MP 10	MP 11	–
Reference test	Side 1 vertical [mm]	−2.96	−5.34	−6.29	−6.05	−5.60	−3.48	–
	Side 2 vertical [mm]	−2.94	−5.46	−6.36	−6.13	−5.67	−3.49	–
	Deviation vertical [mm]	0.01	0.12	0.07	0.08	0.07	0.01	0.060
	Side 1 horizontal [mm]	0.138	0.133	0.128	0.144	0.137	0.117	–
	Side 2 horizontal [mm]	0.124	0.157	0.133	0.146	0.118	0.126	–
	Deviation horizontal [mm]	0.014	0.024	0.005	0.002	0.019	0.009	0.012
	Out-of-plane displacement [mm]	0.05	0.04	0.04	0.04	0.03	0.02	–
Hybrid simulation	Side 1 vertical [mm]	–	–	–	−6.04	−5.64	−3.59	–
	Side 2 vertical [mm]	–	–	–	−6.25	−5.83	−3.76	–
	Deviation vertical [mm]	–	–	–	0.21	0.19	0.17	0.190
	Side 1 horizontal [mm]	–	–	–	0.080	0.100	0.100	–
	Side 2 horizontal [mm]	–	–	–	0.100	0.112	0.121	–
	Deviation horizontal [mm]	–	–	–	0.020	0.012	0.021	0.018
	Out-of-plane displacement [mm]	–	–	–	0.02	0.00	0.04	–

MP, measurement point.

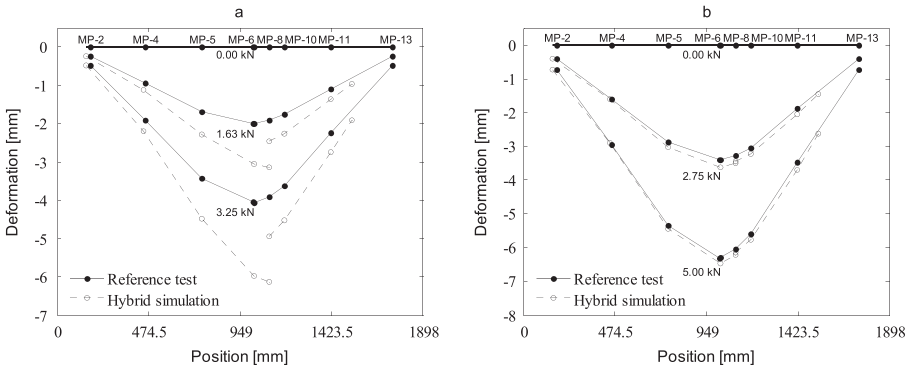

Figure 12: Displacement distribution of glass fibre reinforced polymer beam: (A) digital image correlation (DIC) compensation disabled and (B) DIC compensation enabled. MP, measurement point

The deviation between the numerical and experimental substructure is presented in Figure 13 including vertical, horizontal and rotational error at the shared boundary. For all three DOF, the effect of DIC compensation is significant.

Communication delay compensator

With 20 steps per loading period, compensation of the communication delay is performed through linear regression of the restoring force, Equations (15)–(17). Two different compensator schemes are implemented: ‘no comp’ where the restoring force to the current external displacement is set equal to the previous and ‘linear’ where the restoring force is extrapolated by least-square linear regression from the previous three or four MPs.

From Figure 14A, the displacement distribution of the hybrid simulation reveals a lack of bending stiffness with a maximum deviation of 9.3%, relative to the reference test. However, when a 4-point linear compensator is implemented, the reference test and hybrid simulation correlate with a maximum deviation of 4.6% relative to the reference test cf. Figure 14B.

The deviation between the compensated and given restoring force is presented in Figure 15 for vertical, horizontal and moment error. For all three DOF, the effect is significant within the first 11 steps. However, when the external displacement changes direction, instability is introduced by the compensator which will converge during a number of steps. Within the first half loading period, the averaging error in all three DOFs is presented for 20, 40 and 60 steps per period in Table 5.

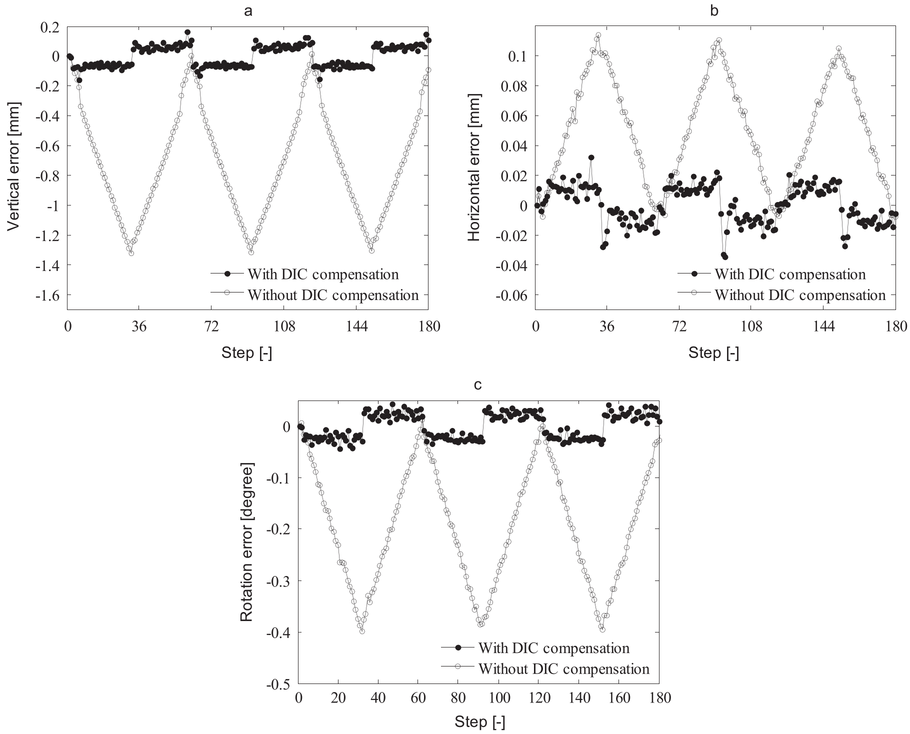

Figure 13: Deviation between cmd and feedback signal at shared boundary: (A) vertical, (B) horizontal and (C) rotation. DIC, digital image correlation

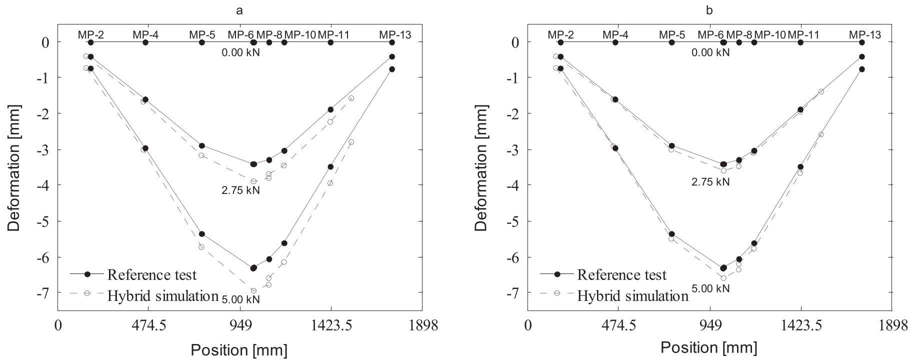

Figure 14: Displacement distribution with 20 sub-steps per period: (A) no compensator and (B) 4-point linear compensator. MP, measurement point

From Table 5, the deviation between the compensated and given restoring force decreases significantly when using a linear compensator within the first half loading period.

Combined effect of compensators

By the use of a 4-point linear compensator Equations (15)–(17), 60 steps per loading period and DIC compensation Equations (1)–(4), the hybrid simulation method is compared with the reference test including strain and displacement measurements.

In Figure 16, the displacement distribution in the reference test and hybrid simulation is shown, measured in the MPs stated in the top part of the graph. The maximum deviation between the reference test and hybrid simulation is 2.1% relative to the reference test.

The vertical and horizontal displacement and rotation of the shared boundary are measured through MP 7, MP 8 and MP 9 for both the reference test and hybrid simulation of the experimental and numerical substructure cf. Figure 17. A good correlation between the hybrid simulation and reference test is identified in terms of vertical and rotational stiffness of the shared boundary. In the horizontal direction, a deviation in stiffness is identified between the reference test and hybrid simulation. In Figure 17C, an offset between the reference test, numerical- and experimental substructure

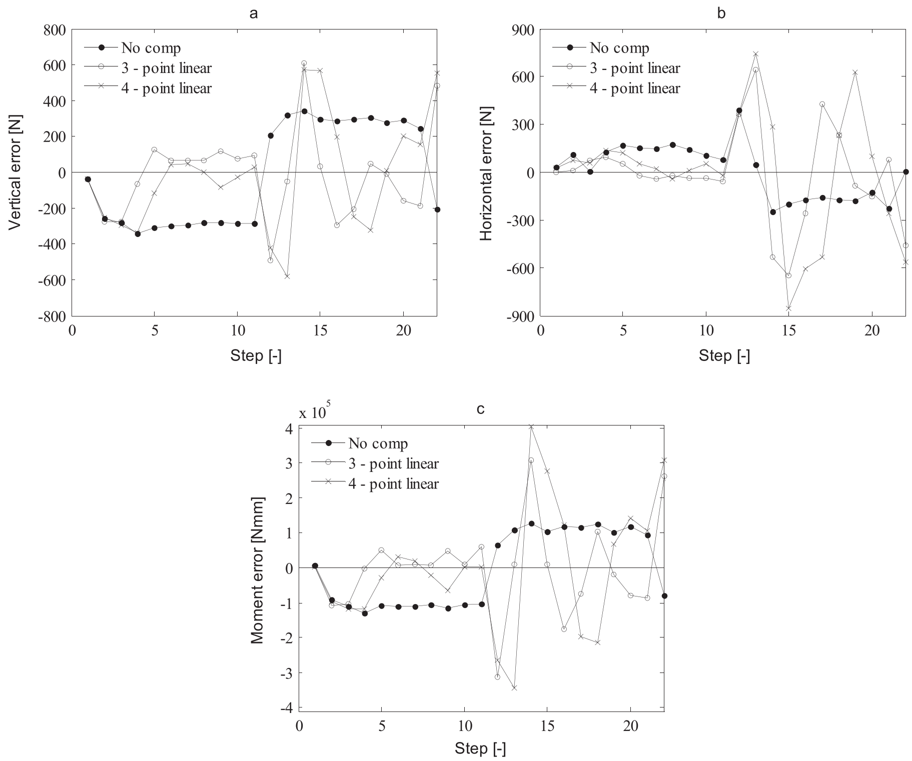

Figure 15: Deviation between predicted and given restoring force at 20 steps per period: (A) vertical, (B) horizontal and (C) moment

Table 5: Average vertical, horizontal and rotational error at first half loading period

Steps per period	Compensator type	Average vertical error [*N*]	Relative deviation [%]	Average horizontal error [*N*]	Relative deviation [%]	Average moment error [Nmm]	Relative deviation [%]
20	Non	−269	–	113	–	−98 900	–
	3-point linear	−41	15.4	22	19.5	−19 465	19.7
	4-point linear	−94	34.9	45	39.8	−35 563	35.9
40	Non	−141	–	66	–	−52 286	–
	3-point linear	−22	15.6	11	16.7	−8457	16.2
	4-point linear	−25	17.7	11	16.7	−9334	17.9
60	Non	−96	–	50	–	−35581	–
	3-point linear	−21	21.9	11	22.0	−7931	22.3
	4-point linear	−11	11.5	7	14.0	−4084	11.5

is identified. In the reference test, this offset is likely due to contact issues in the loading nose. Since the numerical and experimental substructure represents the command (cmd) and feedback signal, respectively, this offset may be due to compliance in the load train.

The strain distribution of the top and bottom flange is compared between the reference test and hybrid simulation through a number of strain gauges mounted on the experimental substructure; see Figure 5 and Figure 6.

For SG-3t, SG-4t and SG-5t represented in Figure 18B, some non-linear effects are observed due to the initiated slits in the top flange of the GFRP beam. The relative maximum deviation between the reference test and hybrid simulation is here found to be 47% for SG-3t, 17% for SG-4t and 6.2% for SG-5t, relative to the reference test.

All strain gauges in the bottom flange reveal a linear response. For SG-3b, SG-4b and SG-5b represented in Figure 5B, the maximum deviation between the reference

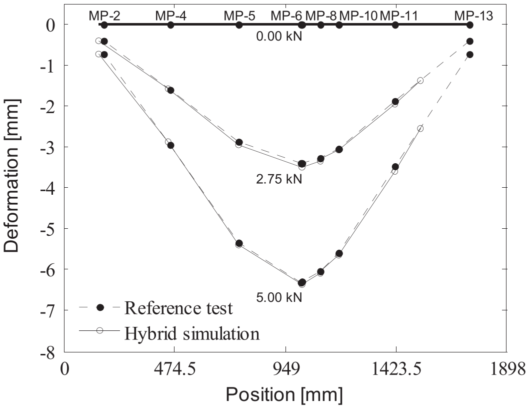

Figure 16: Displacement distribution of glass fibre reinforced polymer beam including test, hybrid simulation and finite element-model. MP, measurement point

test and hybrid simulation is found to be 2.3%, 0.7% and 2.4%, respectively, relative to the reference test.

Discussion

The overall response of the hybrid simulation was coinciding with the reference test within maximum 2.1%, when using a 4-point linear compensator and DIC compensation for displacement adjustment. This proved the hybrid simulation setup was capable of performing an accurate simulation of the compliance behaviour of the composite beam. Some discrepancies between the two were observed, and these will be discussed in the following. The main topics are as follows: discrepancies between the two sides of the beam, the strains in the top and bottom flanges and the effects of the compensator schemes.

A discrepancy between the deflections of the two sides of the beam was observed. For the reference test, the deviation was in average 60 μm and 12 μm for the vertical and horizontal displacements. For the hybrid simulation, the deviation was 190 μm and 18 μm for vertical and horizontal displacements, cf. Table 4. This indicates some out-of-plane effects in the test rig connecting the actuators to the specimen. One can argue whether to fix the actuators against out-of-plane movements to minimise these errors. However, all specimens have some out-of-plane imperfections that might introduce the observed out-of-plane displacements, and if the test rig is constraining this, it might initiate undesired damage to the specimen and load train instead of letting it distort freely.

The deviation in strains between the hybrid simulation and the reference test was maximum 47% – found on the top-flange, closest to the loading nose. This deviation is most likely caused by stress concentrations introduced by

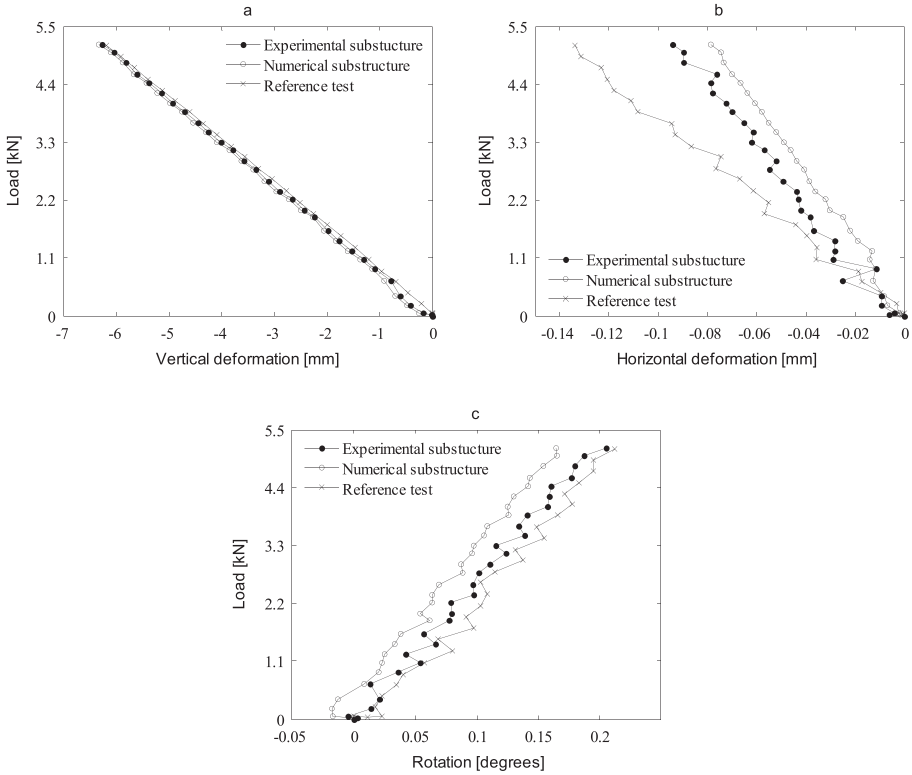

Figure 17: Displacement of the shared boundary: (A) vertical, (B) horizontal and (C) rotation

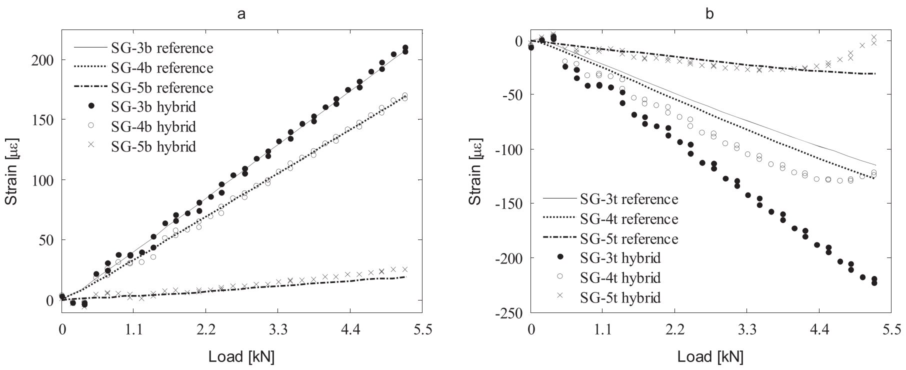

Figure 18: Strain gauge measurements at the experimental substructure: (A) bottom flange and (B) top flange. SG, strain gauge measurement

the point load applied in the reference test. The two remaining strain gauges at the top-flange indicated a non-linear strain induced by buckling (cf. Figure 18B) in the hybrid simulation, which was not the case in the reference test. It is not clear why buckling was introduced before in the hybrid simulation than in the reference test. However, buckling is induced by small imperfections in the geometry, layup, cutting of the slit etc., and these might vary greatly from specimen to specimen. However, the different buckling behaviour is not important in relation to the performance of the hybrid simulation, since this primarily depends on the ability of obtaining the correct overall response and transferring the DOF correctly in the shared boundary.

The emulated structure was designed to yield a non-linear response of the restoring force from the experimental substructure. Although non-linear strains were observed, cf. Figure 18, they were not large enough to yield a non-linear relation between the restoring force and the applied displacement. This implies that the compensators were only investigated in the linear regime. However, the *DIC compensator* is only dependent on the compliance of the load train and will therefore most likely be adequate for non-linear experimental substructure as well.

The DIC compensation technique showed a significant improvement of the beam's overall deflection, with a deviation between the reference test and hybrid simulation going from 33 to 2.6%, cf. Figure 12 while slowing the step speed by 50 ms. This is because the deformations and slack in the test fixture, see Figure 5, are not accounted for when disabling the DIC compensation. This also means that the error between the numerical and experimental substructure in the shared boundary could be decreased by 89% for rotations and 87% for vertical- and 69% for horizontal displacements, cf. Figure 13. This proved that using DIC in an outer control loop to operate the shared boundary is an efficient strategy.

The accuracy of the hybrid simulation was improved through compensation of communication delay. This was done by linear regression, using 3 and 4 previous data points. The 4-point compensator was capable of improving the overall deflection response of the beam from 9.3 to 4.6% cf. Figure 14. The accuracy of compensator was evaluated by comparing the predicted restoring force with the actual restoring force, cf. Figure 15 and Table 5. For both force and moment, the compensator improved the accuracy for the first half period of the loading sequence. But when the external displacement changes direction, the accuracy of the compensator diminished. The loss of accuracy is most likely caused by hysteresis effects in the specimen and test setup.

Conclusion

A static single-component hybrid simulation of a composite beam was performed, and the results were compared to the reference test. In these tests, high correspondence between the hybrid simulation and the reference test was observed, when comparing the overall displacement response along the shared boundary cf. Figure 16 and Figure 17. This verifies the hybrid simulation as a substructural testing technique for the given configuration. This also shows that comparing the hybrid simulation with a reference test is a powerful tool when evaluating hybrid simulation; however, in larger structures, this is not feasible.

In order to increase the accuracy of the physical specimen's stiffness response, communication delay was compensated through linear extrapolation of the previous restoring force as function of external displacement. This increased the accuracy by 2.1%. Furthermore, the deviation between the numerical- and experimental substructure was improved by adjusting the displacement through DIC compensation. This technique improved the accuracy of the vertical, horizontal displacement and rotation by 87, 69 and 89%, respectively. This DIC compensator also improved the accuracy of the overall displacement shape from 33 to 2.6%. This method was introduced because of the high compliance of the load train. The higher compliance and complexity in the load train are due to the test is a single component test that requires a more comprehensive test rig to apply the desired actions in the shared boundary. This is in general not the case in multi-component hybrid simulation where the shared boundary is simple with few DOF.

ACKNOWLEDGEMENTS

The authors would like to acknowledge the financial support from the Danish Centre for Composite Structures and Materials (DCCSM) funded by the Danish Council for Strategic Research within Sustainable Energy and Environment (grant 09-067212). Furthermore, the authors acknowledge Fiberline Composites, Barmstedt Allé 5, 5500 Middelfart, DK, for the donation of the GFRP test specimens.

REFERENCES

1. Jensen, F. M., Falzon, B. G., Ankersen, J., and Stang, H. (2006) Structural testing and numerical simulation of a 34m composite wind turbine blade. *Compos. Struct.* **76**, 52–61.
2. Jensen, F. M. (2008) Ultimate strength of a large wind turbine blade. Department of Civil Engineering, Technical University of Denmark, Kgs. Lyngby.
3. Brondsted, P., Lilholt, H., and Lystrup, A. (2005) Composite materials for wind power turbine blades. *Annu. Rev. Mater. Res.* **35**, 505–538.
4. Takanashi, K., and Nakaschiman, M. (1987) Japanese activities on ON-LINE testing. *J. Eng. Mech.* **113**, 1014–1032.
5. Chen, C., Ricles, J. M., Karavasilis, T. L., Chae, Y., and Sause, R. (2012) Evaluation of a real-time hybrid simulation system for performance evaluation of structures with rate dependent devices subjected to seismic loading. *Eng. Struct.* **35**, 71–82.
6. Bonelli, A., and Bursi, O. S. (2004) Generalized-alpha methods for seismic structural testing. *Earthquake Eng. Struct. Dyn.* **33**, 1067–1102.
7. Karavalis, T. L., Ricles, J. M., Sause, R., and Chen, C. (2011) Experimental evaluation of the seismic performance of steel MRFs with compressed elastomer dampers using large-scale real-time hybrid simulation. *Eng. Struct.* **33**, 1859–1869.
8. Ito, M., Murata, Y., Hoki, K., and Nakashima, M. (2011) Online hybrid test on buildings with stud-type damper made of slitted steel plates stiffened by wood panels. *Procedia Eng.* **14**, 567–571.
9. Jacobsen, A., Hitaka, T., and Nakashima, M. (2010) Online test of building frame with slit-wall dampers capable of condition assessment. *J. Constr. Steel Res.* **66**, 1320–1329.
10. Lin, Y. Z. and Christenson, R. E. (2009) Comparison of real-time hybrid testing with shake table test for an MR damper controlled structure. *American Control Conference*, pp. 5228-5233.
11. Carrion, J. E., Spencer Jr., B. F. and Phillips, B. M. (2009) Real-time hybrid testing of a semi-actively controlled structure with an MR damper. in *American Control Conference*, Hyatt Regency Riverfront, St. Louis, MO, USA.
12. Shao, X., Reinhorn, A. M., and Sivaselvan, M. V. (2011) Real-time hybrid simulation using shake tables and dynamic actuators. *J. Struct. Eng.* **137**, 748–760.
13. Chen, C., Ricles, J. M., Marullo, T. M., and Mercan, O. (2009) Real-time hybrid testing using unconditionally stable explicit CR integration algorithm. *Earthquake Eng. Struct. Dyn.* **38**, 23–44.
14. Waldbjørn, J., Høgh, J., Wittrup-Schmidt, J., Nielsen, M., Branner, K., Stang, H., and Berggreen, C. (2013) Strain and deformation control by fibre Bragg grating and digital image correlation. *Strain.* **50**, 262–273.
15. Fayolle, X., Galloch, S., and Hild, F. (2007) Controlling testing machines with digital image correlation. *Exp. Tech.* **31**, 57–63.
16. Waldbjørn, J., Høgh, J., Berggreen, C., Wittrup-Schmidt, J. and Branner, K. (2013) Hybrid testing of composite structures with single-axis control. in *The 19th International Conference on Composite Materials*, Montreal, Canada.
17. ASTM (2011) Standard test method for tensile properties of polymer matrix composite materials. West Conshohocken, Pennsylvania, United States of America: ASTM International.
18. ASTM (2014) Standard Test Method for Shear Properties of Composite Materials by the V-Notched Beam Method. ASTM International, West Conshohocken, Pennsylvania, United States of America.
19. ANSYS Inc. (2013) ANSYS Mechanical APDL Theory Reference. ANSYS Inc., Canonsburg, PA, USA.
20. Bitter, R., Mohiuddin, T., and Nawrocki, M. (2001) LabView Advanced Programming Techniques. CRC Press, Boca Rotan, Florida, USA.
21. N. Instruments (2009) »http://www.ni.com/pdf/manuals/373781e.pdf,« National Instruments, 8. [Online] accessed the November 12, 2014.
22. N. Instruments (2008) »http://www.ni.com/pdf/manuals/374188d.pdf,« National Instruments, 2. [Online] accessed the November 12, 2014.
23. Juan, E. C. and Billie, F. S. J. (2007) Model-based strategies for real-time hybrid testing. Urbana-Champaign: Illinois Digital Environment for Access to Learning and Scholarship - Dept. of Civil and Environmental Engineering.
24. Legendre, A.-M. (1805) New Methods for the Determination of the Orbits of Comets (in French). F. Didot, Paris.
25. Mahin, S. A., Shing, P.-S. B., Thewalt, C. R., and Hanson, R. D. (1989) Pseudodynamic test method. Current status and future directions. *J. Struct. Eng. N. Y.* **115**, 2113–2128.
26. Shing, P. B., Nakashima, M., and Bursi, O. S. (1996) Application of pseudodynamic test method to structural research. *Earthq. Spectra* **12**, 26–56.

Hybrid Simulation of a D-String Stiffened Wind Turbine Blade

Jacob H. Høgh[1], Selim Gunay[2] and Khalid Mosalam[2]
[1]*Mechanical Engineering, Technical University of Denmark*
[2]*Civil- and Environmental Engineering, University of California, Berkeley*

Abstract

Hybrid simulation has previously proven a valid tool for testing structures where a substructure behaves nonlinear while the response of the main structure is predictable. In this study, a hybrid simulation of a D-string stiffener retrofitted in a 34m glass fiber reinforced polymer wind turbine blade. The D-string stiffener is a polyethylene plaited rope that straps together two panels inside the wind turbine blade in order to minimize crack propagation. The D-string stiffener is known to have a non-linear response due to viscoelasticity, while the wind turbine blade is a glass fiber laminate structure with linear elastic properties under operational conditions. The hybrid simulation illustrated the effect of the D-string stiffener's ability to limit the stress in the trailing edge of the wind turbine blade by minimizing the mode I crack opening. This was measured by a decrease in the displacement of the panels connected to the joints by up to 75%. The hybrid simulation illustrated the stiffener's behavior under the wind turbine blade's operational conditions more accurately than standardized static or fatigue tests could have done. However, due to the simplifications of the finite element model in the given studies it cannot be finally concluded whether the positive effects of the D-string stiffener is present, until a hybrid simulation with a more accurate finite element model has been conducted.

Keywords: hybrid simulation, wind turbine, sub-structuring, retrofits, composites

Introduction

Hybrid simulation is a sub structural method where the main part of a structure is simulated numerically while a substructure is tested in a physical experiment [1]. The load is applied in an iterative process while transferring the actions between the numerical model and the experiment in order to include the stiffness of the entire structure [2]. The method is beneficial to use in structures where the behaviour of a large part of it is well known and therefore easily simulated while a smaller substructure has unknown structural behaviour. This has been the case for the previous applications such as building structures with earthquake dampers [3], [4], [5]. Much effort has been invested in developing hybrid simulation for dynamic applications, primarily focusing on development and implementation of time integration schemes [6], [7], [8], [9] and compensation for transfer system delay [10] [11]. Hybrid simulation has to the authors knowledge not been utilized for wind turbine blade testing. This might be due to the complexity of the shared boundary between the numerical model and the experiment [12]. In a wind turbine the structure is made up of composite and sandwich materials glued together to form the aerofoil and internal shear stiffeners of different designs. A partition between these panels would lead to a highly complex shared boundary with, in principal infinite degrees of freedom as opposed to typical single degree of freedom shared boundaries in classical hybrid simulation [13], [14]. However, several retrofitted elements on wind turbine blades have been suggested in order to prevent crack initiation and propagation [15], [16] or improve aerodynamic properties and control [17]. These retrofits is easier to test in a hybrid simulation since the main structure, i.e. the wind turbine blade, has linear elastic properties until fracture [18], [19], [20], while the behaviour of- and interaction with the retrofitted element is not. Hybrid simulation is therefore suggested as a beneficial method for testing for retrofits in wind turbine blades. Another benefit of using hybrid simulation for wind turbine blades is the complex loading consisting of gravity-, wind-, centripetal- [21], gyroscopic- and operational forces [22]. These loads can be simulated in a finite element model but have so far not been simulated in a laboratory primarily due to the sheer size of the wind turbine blade reaching size > 80m.

In this paper a hybrid simulation is performed on a 34m glass fibre composite wind turbine blade by SSP Technology A/S [23], [24], [15] retrofitted with a D-string stiffener consisting of a plaited polyethylene rope [16]. The wind turbine blade is modelled numerically while the D-string stiffener is tested in an experiment. The purpose of the D-string stiffener is to protect the wind turbine blade against crack initiation and propagation in glued connections in the wind turbine blade as a result of the gravity force. The test is performed as a pseudo-dynamic simulation due to the high relative stiffness of the D-string stiffener compared to the wind turbine blade. This result in loading frequencies near first natural frequency of the blade will be experienced as static loads on the D-string.

Hybrid Simulation Setup

The structure tested in the hybrid simulation is a 34m SSP glass fibre reinforced plastics (GFRP) wind turbine blade, cf. Fig. 1. The aerofoil of the structure is largely made up of GFRP composites, cf. Fig. 2, and in certain areas where the bending stiffness is critical, i.e. the shear walls and trailing edge panels, the aerofoil is made up as a sandwich structure with GFRP skins and PVC foam core [22], cf. sandwich effect [19]. In order to decrease opening of the sandwich panels connecting the trailing edges a D-string stiffener is connected to the two panels, cf. Fig. 1b). In real life usage the D-string stiffener is to be installed at multiple cross sections along the length of the wind turbine blade, however in order to test the concept the D-string stiffener is installed only at one location, i.e. 10.0m from the root of the blade, cf. Fig. 1b).

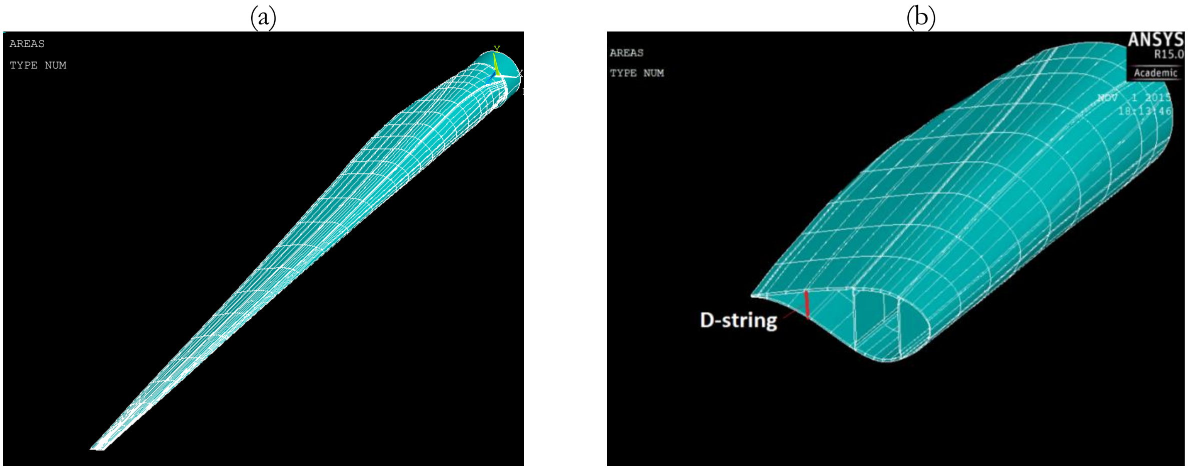

Fig. 1 The 34m SSP GFRP wind turbine blade a) the full structure b) the location of the D-string stiffener at 10.0 m from root

A hybrid simulation is performed with the entire wind turbine blade simulated in a finite element model while the D-string stiffener is tested experimentally. This is done in order to verify the hybrid simulation method for testing of retro-fitted components in wind turbine blades.

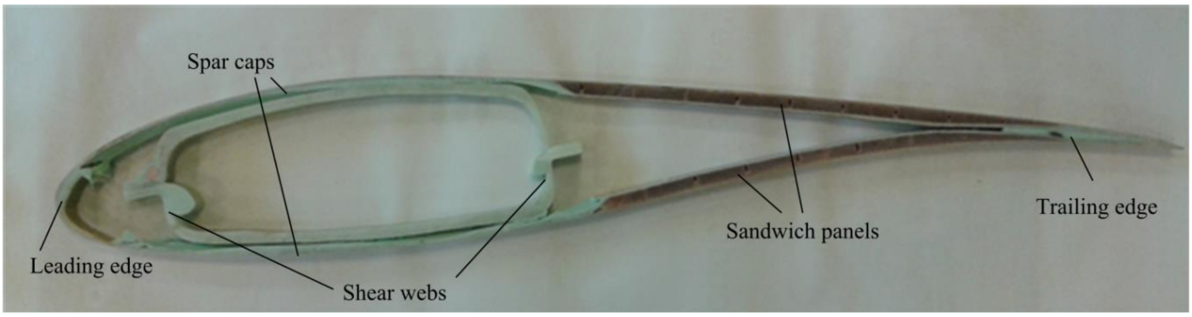

Fig. 2 the cross section of the wind turbine blade with explanatory legends

In real-life service the wind turbine blade is exposed to three forces: drag-, gravitational- and centripetal-. Previous studies performed by the company Bladena A/S have shown that the gravitational force is the primary force causing opening of the trailing edge which the D-string protects against. In order to limit computational resources the model is therefore run with only gravity forces acting on it. This is done by applying a gravitational acceleration to all nodes in the lengthwise (z-axis) and edgewise direction (x-axis) of the blade and gradually changing the amplitude of the acceleration between -1g to 1g. The acceleration is thereby out of phase with a lag of ¼ of a period. It is noted that this results in a constant magnitude of the acceleration vector of 1g.

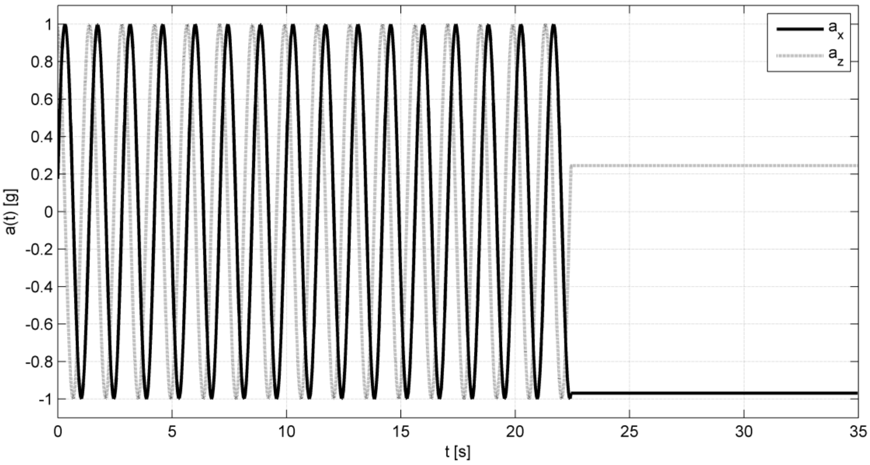

Fig. 3 The gravity acceleration of the wind turbine blade in the x- and z-direction

Numerical Substructure

The numerical sub-structure is run in the open source finite element code OpenSees [25] and in order to limit the analysis the full finite element model of the blade, cf. Fig. 1, is simplified at several points. The finite element model is reduced to a shell model of 92 nodes and 102 elements with six of freedom at each node. The shell element is a 4-node shell which uses a bilinear isoparametric formulation, cf. [26]. The blades geometry is defined in 11 cross sections with 8-9 nodes per section cf. Fig. 4.

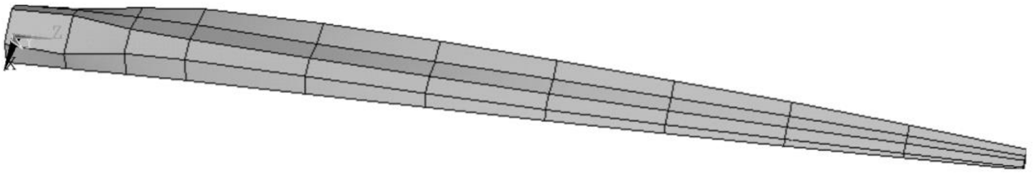

Fig. 4 Finite element model of the wind turbine blade used in the hybrid simulation

Due to the simplicity of the finite element model the several different glass fibre materials in the wind turbine blade cannot be modelled. Instead properties of a similar pultruded GFRP beam is used for the material, cf. [12], except here the Poisson's ratio are taken as the average of the two in-plane values found. The properties are listed with the 1, 2 and 3 directions, where 1 is the in-plane longitudinal direction of the blade, 2 is in-plane transverse direction and 3 is out-of-plane direction.

Table 1 Young's modulus, Poisson's ratio and shear stiffness in three directions and density of the GFRP material

E_1 [GPa]	E_2 [GPa]	E_3 [GPa]	ν_{12} [-]	ν_{23} [-]	ν_{13} [-]	G_{12} [GPa]	G_{23} [GPa]	G_{13} [GPa]	ϱ [kg/m^3]
28.36	9.96	9.96	0.155	0.155	0.155	3.235	3.235	3.235	2300

The dynamic properties of the wind turbine blade were determined in a modal analysis and the first 10 Eigen frequencies is listed, cf. Table 2.

Table 2 the first 10 natural frequencies

Mode	Frequency [Hz]
1	0.85
2	1.27
3	3.06
4	5.77
5	7.89
6	13.72
7	14.60
8	16.06
9	23.02
10	23.40

Experimental Substructure

The experimental substructure tested in the hybrid simulation is a D-string stiffener, which simply consists of an eight stranded, plaited polyethylene rope held together by a plastic connector, cf. Fig. 5a). From a non-destructive test the initial stiffness of the D-string was found to 1360.4N/mm. The natural frequencies of the string in the longitudinal direction is determined by eq. (1), cf. [27].

$$\omega_n = \frac{n\pi}{L}\sqrt{\left(\frac{P}{\mu}\right)} \; ; \; for\; n = 1,2,\ldots \tag{1}$$

Here ω_n is the natural frequency of the n'th mode, in radians per time unit, L the length of the string, P the tensional force on the string and μ the mass per length unit of the string. The first natural frequency is determined. The string 314.7mm of length and the mass per length is 10g/m and it was pre-tensioned to 400N to make sure it does not go slack during the hybrid simulation. This yields a first natural frequency of f_1 = 318Hz, $f_n = n \cdot f_1$.

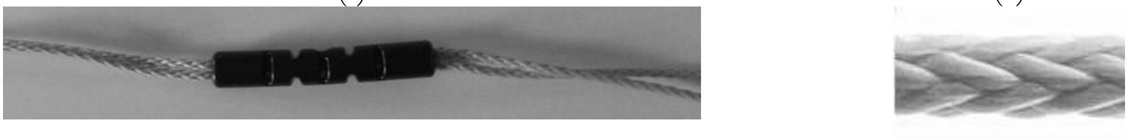
(a)

(b)

Fig. 5 the D-string stiffener retrofitted in the wind turbine blade a) the string and PVC connector b) the Marlow V12 – 2.5mm eight strand plaited [28] polyethylene string structure

It is known that the D-string has viscoelastic properties and a relaxation test is therefore performed for 30min starting at 440 N of loading. The force in the string as function of time is presented in Fig. 6. The data is filtered by a 1st order Savitzky-Golay filter. It is clearly seen that viscoelastic effects are pronoun in the D-strings. In the hybrid simulation it is chosen to pretension the load of the string for an hour until the load is stable at 400N.

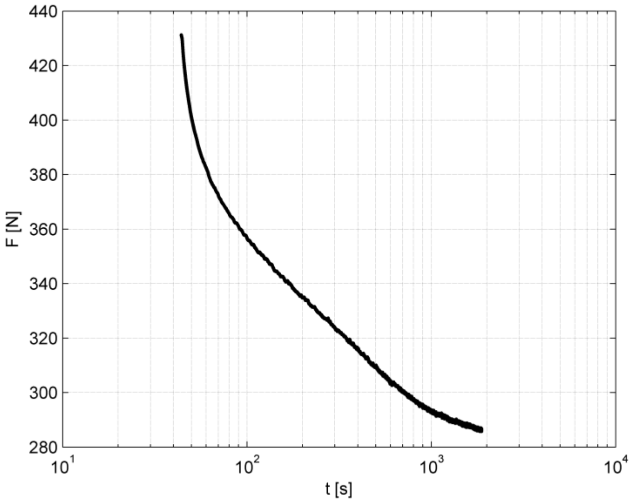

Fig. 6 relaxation plot, force vs time for the D-string stiffener for constant displacement

Experimental setup

The experiment is run in a MTS test machine with a 20kN (50 kips) actuator. The actuator has a stroke of 75mm (3") and is run by a MTS 406 analog PID controller. The load is measured by a 5kN (1.0kip) load cell from Transducer Techniques. The command and feedback signal to and from the controller is sent by a Pacific instrument model 6005 with a model 6035 input board and 6042 DSP output board, both with a 16 bit resolution for A/D and D/A conversion. The Pacific instruments setup has a 70ms time delay for every time step. The Pacific instrument is controlled by a PC that communicates with the hybrid simulation running in OpenSees on another PC. The Pacific instrument PC and the OpenSees PC communicates via a TCP/IP connection and the communication is performed by OpenFresco [29].

a) **b)**

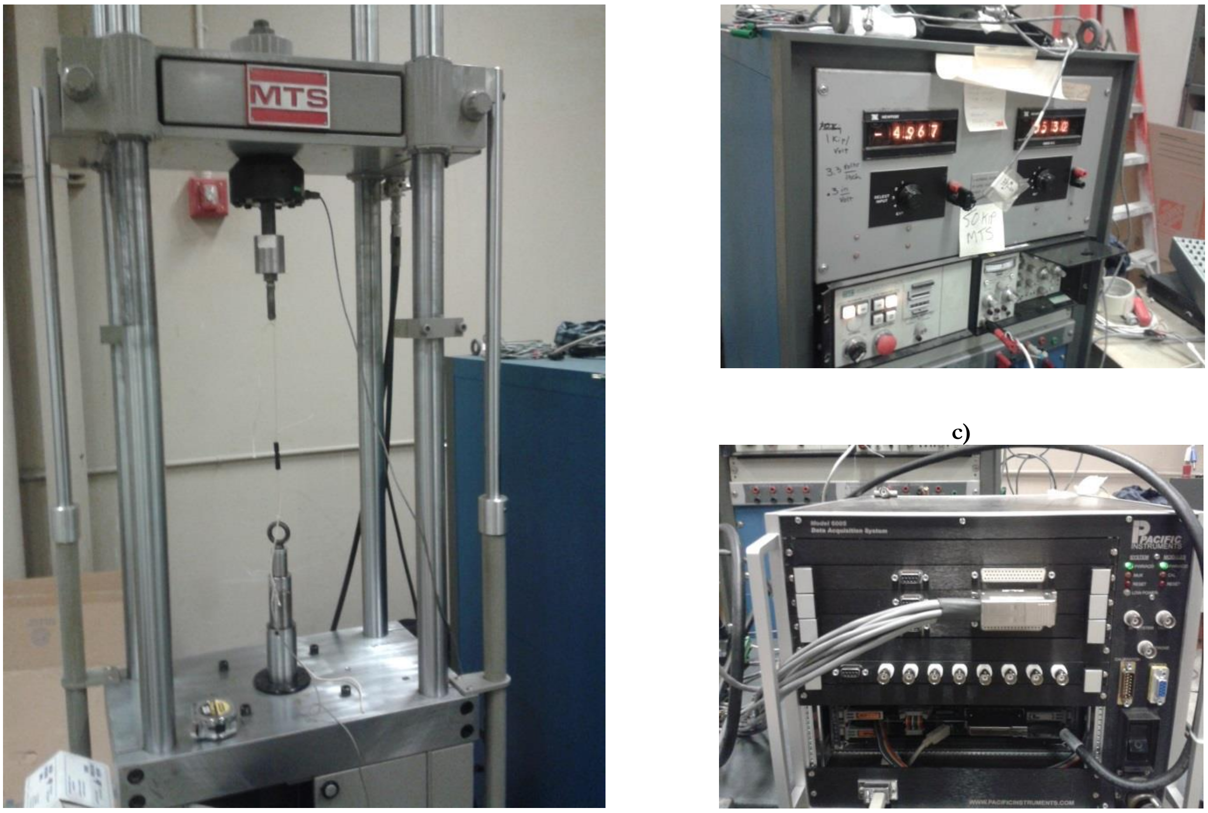

c)

Fig. 7 Test setup a) the D-string stiffener fixed in the MTS station by two eye bolts b) MTS controller c) Pacific instrument D/A and A/D module

The data communication during the hybrid simulation is presented in Fig. 8. First the external load is applied to the finite element model in Opensees and solved for the first time step and the displacement is determined. The communication program then transfers the command displacement to the A/D converter in the I/O instrument. The I/O instrument interpolates the displacement to obtain a command frequency of 1000Hz and converts the digital displacement to an analog command signal. The command signal is handled by the Controller which applies the displacements at a constant rate of 1.27mm/s and measures the restoring force from the specimen. The restoring force is then fed back through the A/D converter to the Compensator to compensate for the communication delay. Finally the restoring force is inserted into the equation of motion eq. (2) and used in the next iteration of the time integration. The process is repeated for each iteration.

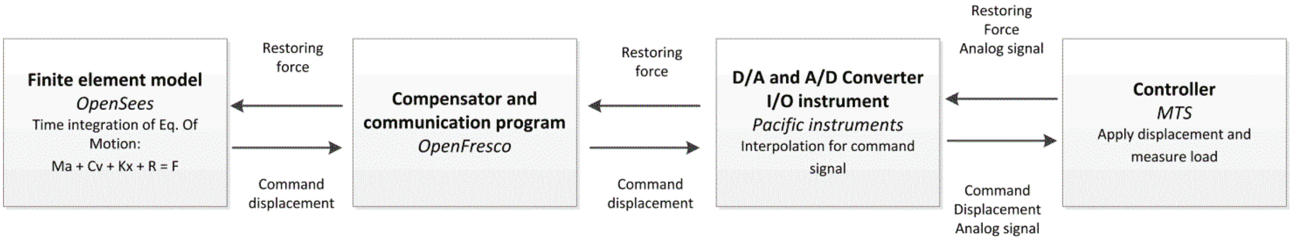
Finite element model
OpenSees
Time integration of Eq. Of Motion:
Ma + Cv + Kx + R = F
Restoring force
Command displacement
Compensator and communication program
OpenFresco
Restoring force
Command displacement
D/A and A/D Converter I/O instrument
Pacific instruments
Interpolation for command signal
Restoring Force Analog signal
Command Displacement Analog signal
Controller
MTS
Apply displacement and measure load

Fig. 8 Data communication in the pseudo-dynamic hybrid simulation

Pseudo-Dynamic Hybrid Simulation

The hybrid simulation method is appropriate for testing of the D-string's performance in the blade, due to the cost efficiency compare to full scale testing of an entire blade. Furthermore, the main blade structure performs linear elastic during loading and therefore reasonably accurate to simulate whereas the experimental substructure has viscoelastic effects, cf. Fig. 6. In this test it is chosen to perform pseudo-dynamic hybrid simulation i.e. where the numerical model is run as a transient analysis solving the equation of motion while the experiment is run at constant strain rate, thereby not including dynamic effects of damping and inertia forces. Since the blade is operated at loading frequencies close the natural frequencies of the blade the dynamic effects are important to implement in the finite element simulation. However, the natural frequencies are much higher for the D-string f1 = 318Hz cf. eq. (1) than the loading frequency of 0.713Hz and the test is therefore largely experienced by the D-string as static, which makes pseudo-dynamic simulation suitable.

The equation of motion eq. (2) of the system was solved by time integration by the implicit Newmark algorithm [30], here the Average Acceleration method [31] is chosen i.e. $\gamma = \frac{1}{2}$ and $\beta = \frac{1}{4}$.

$$\boldsymbol{M\ddot{u}} + \boldsymbol{C\dot{u}} + \boldsymbol{Ku} + \boldsymbol{R} = \boldsymbol{F} \tag{2}$$

Here **M, C** and **K** are the mass, damping and stiffness matrices for the finite element model, **F** the external load on the structure from the gravity, **R** is the restoring force from the experimental substructure and $\mathbf{u}$, $\dot{\mathbf{u}}$ and $\ddot{\mathbf{u}}$ the displacement, velocity and acceleration vectors of the finite element model, respectively, *i* denotes the iteration number. In order to limit the bandwidth of the system of equations, the reverse Cuthill-McKee scheme [32] was applied. The system of equations was solved using the multi-frontal LU factorization solver [33]. The boundary conditions of the numerical model was handled using the Transformation equation method [34].

Results

In order to evaluate the D-string's behaviour at the most critical loading, the hybrid simulation is run for a loading frequency of 0.713Hz which corresponds to 99% of first natural frequency. This is the frequency for which the opening of the trailing edge was largest. The opening of the trailing edge as function of time is plotted for a FEM with no D-string and for the hybrid simulation, cf. Fig. 9. The oscillations observed are a combination of several mode shapes. After the wind turbine blade is stopped spinning, i.e. 24s, only one mode shape of the oscillation are active.

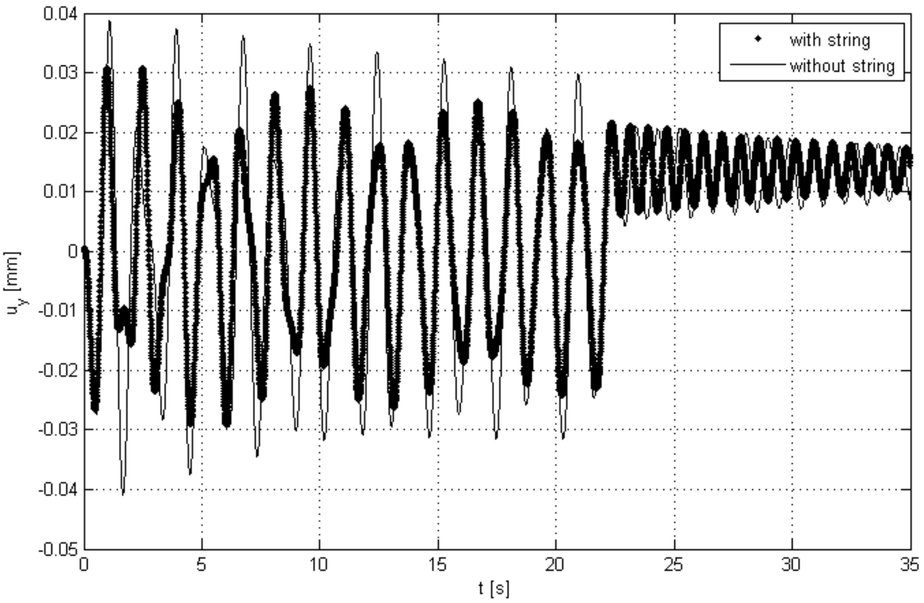

Fig. 9 a) opening of trailing edge without D-string stiffener and with

In Fig. 9 it is observed that higher modes are excited at the start of the loading due to the impact of the gravity force at step one, however these higher modes are damped out after approximately 15s. When comparing the opening with and without stiffener it is observed that the stiffener limits the displacements up to 75%. However after the higher modes have damped out the effect is closer to 33% decrease in displacements. The force applied the D-string stiffener is plotted as function of displacement in Fig. 10. This shows how the D-string limits the force acting on the trailing edge. It is noted that the force measured here is not equal to the force that would have been applied the trailing edge, since the shear webs, cf. Fig. 2, assists in carrying the loads in the absence of the D-string.

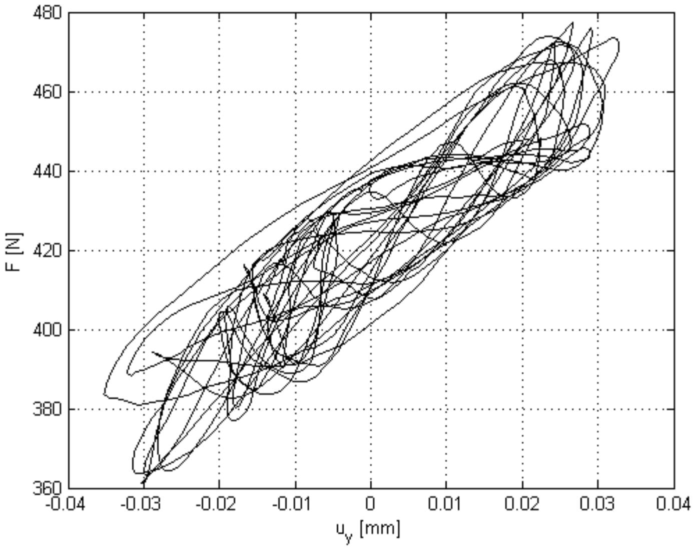

Fig. 10 Force in D-string stiffener as function of opening between the trailing edge panels

The displacement of the entire wind turbine blade during loading was subjected to Fast Fourier Transformation (FFT) to identify frequency of active modes. In the y-direction i.e. edgewise oscillations of the blade the dominant frequencies were: 0.0286Hz, 0.714Hz and 1.086Hz and for the x-direction i.e. flap-wise oscillations the dominant frequency was 0.70Hz. The frequency of 0.714Hz corresponds with the loading frequency of the blade. The oscillations of the wind turbine blade is illustrated in Fig. 11 in the edgewise direction for the wind turbine blade spinning i.e. oscillating loading t < 22s and for the wind turbine blade not moving t > 22s i.e. constant loading, cf. Fig. 3. The oscillations is presented from the hybrid simulation but it is noted that the D-string stiffener does not affect the global response of the wind turbine blade but only the local phenomenon of opening of the trailing edge panels.

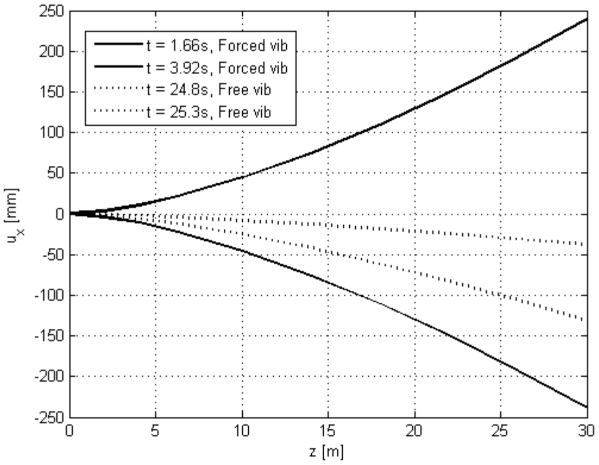

Fig. 11 Oscillations of the wind turbine blade in the x-direction (edgewise) for forced (wind turbine blade spinning) and free oscillations (constant loading i.e. wind turbine not moving)

Discussion

The results shows that a D-string stiffener retrofitted between the trailing edge panels reduced the opening between them in the hybrid simulation performed, cf. Fig. 9. The D-string stiffener thereby decreased the loading on the trailing edge, cf. Fig. 10, and possibly the risk of failure in the trailing edge. The test was run as pseudo-dynamic hybrid simulation meaning that the D-string was loaded at strain rates lower than the real life usage which results in lower restoring forces due to lower stiffness. The effect of the D-string is therefore conservative compared to real-life usage where the stiffness would be higher. However, even though the hybrid simulation showed positive effects of the D-string it cannot be finally concluded whether or not the D-string will decrease trailing edge failure when installed in a wind turbine blade in-situ. This is due to the simplifications of the wind turbine blade made in this study. The geometry, material properties, loading and mesh does not have the adequate level of detail necessary to simulate the behaviour of a wind turbine blade to conclude whether or not the D-string stiffener will decrease the opening between the sandwich panels in the trailing edge. Furthermore the model does not take into account the complex interaction between wind loading and deformation of the blade, cf. aeroelastic effects [35]. Furthermore, some studies conclude that failure in the trailing edge can be prevented by the D-string, and thereby indicating that the failure is caused by pure mode I opening [16]. However, it is not certain whether pure mode I is the root cause of failure/cracking in the trailing edge or whether it can be attributed to in-plane and/or out-of-plane shear, crack mode II and III, respectively, cf. fracture mechanics. Furthermore, relaxation effects in the D-string stiffener were observed in Fig. 6 and these might in the long term cause the D-string to loose tension. However, it was not possible to fit any know relaxation models for polymers, e.g. [36] to the measured relaxation data and the long term response of the D-string is therefore yet unknown.

Due to these assumptions and simplifications of the finite element model and the D-string stiffener the hybrid simulation is therefore primarily an initial study indicating positive effects from the D-string on the stress in the trailing edge. A more detailed finite element model must be included in the hybrid simulation before a final conclusion can be made about the D-string effects. The limited meshing and geometry building options in the open source finite element code OpenSees might not be adequate in order to build the advanced geometry of the wind turbine. Furthermore the OpenSees code cannot include aeroelastic effects. It might therefore be beneficial to switch to a more advanced finite element program for the time integration.

Conclusion

A pseudo dynamic hybrid simulation was performed on a glass fibre reinforced plastics wind turbine blade with a D-string stiffener retrofitted in order to prevent from opening of the trailing edge panels. The simulation was performed with the main objective of applying the hybrid simulation method to wind turbine blades with retrofitted elements and to give initial evaluation of such retrofitted elements. The test showed decrease of in opening of the trailing however it was also concluded that the finite element model needs more detail in order to accurately reflect the behaviour of a wind turbine blade and, likewise how the D-string stiffener would perform under such conditions.

Acknowledgement

The authors acknowledge the financial support from Danish Centre for Composite Structures and Materials (DCCSM) funded by the Danish Council for Strategic Research within Sustainable Energy and Environment (grant 09-067212) as well as the financial support from the Otto Mønsted fund, Copenhagen, Denmark. Furthermore the authors acknowledge the company Bladena A/S for providing D-string stiffeners and properties of the finite element model of the blade.

References

[1] V. Saouma and M. Sivaselvan, Hybrid Simulation - Theory, Implementation and Applications, London, UK: Taylor & Francis, 2008.

[2] P. A. Bonnet, The Development of Multi-axis Real-time Subrstructure Testing, Oxford: University of Oxford, 2006.

[3] A. Jacobsen, T. Hitaka and M. Nakashima, "Online test of building frame with slit-wall dampers capable of condition assement," *Journal of Constructional Steel Research,* vol. 66, no. 11, pp. 1320-1329, 2010.

[4] M. Nakashima and N. Masaoka, "Real-Time On-Line Test for MDOF Systems," *Earthquake Engineering and Structural Dynamics,* vol. 28, pp. 393-420, 1999.

[5] T. L. Karavalis, J. M. Ricles, R. Sause and C. Chen, "Experimental evaluation of the seismic performance of steel MRFs with compressed elastomer dampers using large-scale real-time hybrid simulation," *Engineering Structures,* vol. 33, pp. 1859-1869, 2011.

[6] B. Wu, G. Xu, Q. Wang and M. S. Williams, "Operator-splitting method for real-time substructure testing," *Earthquake Engineering and Structural Dynamics,* vol. 35, pp. 293-314, 2006.

[7] A. Bonelli and O. S. Bursi, "Generalized-alpha methods for seismic structural testing," *Earthquake Engineering and Structural Dynamics,* vol. 33, pp. 1067-1102, 2004.

[8] B. Wu, L. Deng and X. Yang, "Stability of central difference method for dynamic real-time substructure

testing," *Earthquake Engineering and Structural Dynamics,* vol. 38, pp. 1649-1663, 2009.

[9] O. S. Bursi, A. Gonzalez-Buelga, L. Vulcan, S. A. Neild and D. J. Wagg, "Novel coupling Rosenbrock-based algorithm for real-time dynamic substructure testing," *Eartquake Engineering and Structural Dynamics,* vol. 37, pp. 339-360, 2008.

[10] M. Ahmadizadeh, G. Mosqueda and A. M. Reinhorn, "Compensation of actuator delay and dynamics for real-time hybrid simulation," *Earthquake Engineering and Structural Dynamics,* vol. 37, pp. 21-42, 2008.

[11] P. A. Bonnet, M. S. Williams and A. Blakeborough, "Compensation of actuator dynamics in real-time hybrid tests," in *Proc. IMechE Vol. 220 Part I: J. Systems and Control Engineering*, 2006.

[12] J. Høgh, J. Waldbjørn, J. Wittrup-Schmidt, H. Stang and C. Berggreen, "Quasi-static single-component hybrid simulation of a composite structure with multi-axis control," *Strain,* vol. 51, pp. 459-473, 2015.

[13] K. Takanashi and M. Nakashima, "Japanese Activities on On-line Testing," *Journal of Engineering Mechanics,* vol. 113, no. 7, pp. 1014-1032, 1987.

[14] C. Chen, J. M. Ricles and T. L. Karavasilis, "Evaluation of a real-time hybrid simulation system for performance evaluation of structures with rate dependent devices subjected to seismic loading," *Engineering Structures,* vol. 35, pp. 71-82, 2012.

[15] M. F. Jensen, "Ultimate strength of a large wind turbine blade," Risø National Laboratory for Sustainable Energy & Department of Civil Engineering, Technical University of Denmark, Roskilde & Kgs. Lyngby, Denmark, 2008.

[16] Bladena A/S, "Bladena," Bladena, 1 12 2015. [Online]. Available: http://www.bladena.com/abe/Publications.aspx. [Accessed 1 12 2015].

[17] P. B. Andersen, L. Henriksen, M. Gaunaa, C. Bak and T. Buhl, "Deformable trailing edge flaps for modern megawatt wind turbine controllers using strain gauge sensors," *Wind Energy,* vol. 13, no. 2-3, pp. 193-206, 13.

[18] A. R. Bunsell and J. Renard, Fundamentals of fibre reinforced composite materials, Cornwall, UK: IOP Publishing Ltd, 2005.

[19] D. Zenkert, Sandwich Construction, Eastborne: CPI Antony Rowe, 1995.

[20] D. Zenkert and M. Battley, Foundations of Fibe Composites, Lyngby, Denmark: Technical University of Denmark, 2006.

[21] M. H. Hansen, "Aeroelastic Stability Analysis of Wind Turbines Using an Eigenvalue Approach," *Wind Energy,* vol. 7, pp. 133-143, 2004.

[22] P. J. Schubel and R. J. Crossley, "Wind Turbine Blade Design," *Energies,* vol. 5, pp. 3425-3449, 2012.

[23] L. C. Overgaard, E. Lund and O. T. Thomsen, "Structural collapse of a wind turbine blade. Part A: static test and equivalent single layered models," *Composites: Part A,* vol. 41, pp. 257-270, 2010.

[24] L. C. Overgaard and E. Lund, "Structural collapse of a wind turbine blade. Part B: Progressive interlaminar failure models," *Composites: Part A,* vol. 41, pp. 271-283, 2010.

[25] University of California, Berkeley, "OpenSees Wiki," University of California, Berkeley, 10 5 2012. [Online]. Available: http://opensees.berkeley.edu/wiki/index.php/Main_Page. [Accessed 30 1 2015].

[26] E. N. Dvorkin and K.-J. Bathe, "A continuum mechanics based four-node shell element for general non-linear analysis," *Engineering Computations,* vol. 1, pp. 77-88, 1984.

[27] B. C. (. Jensen, Teknisk Ståbi (In Danish), Copenhagen: Nyt Teknisk Forlag, 2007.

[28] R. Chattopadhyay, "Textile rope - A review," *Indian Journal of Fibre & Textile Research,* vol. 22, pp. 360-368, 1997.

[29] A. Schellenberg, S. A. Mahin and G. L. Fenves, "A software framework for hybrid simulation of large structural systems," in *Structural Engineering Research Frontiers*, 2007.

[30] N. M. Newmark, "Method for Computation for Structural Dynamics," *ASCE Journal of Engineering, Mechanical Division,* vol. 85, pp. 67-94, 1959.

[31] P. B. Shing, M. Nakashima and S. O. Bursi, "Application of Pseudodynamic Test Method to Structural Research," *Earthquake Spectra,* vol. 12, no. 1, 1996.

[32] E. Cuthill and J. McKee, "Reducing the bandwith of sparse symmetric matrices," in *ACM '69 Proceedings of the 1969 24th national conference*, New York, 1969.

[33] T. A. Davis and I. S. Duff, "An unsymmetric-pattern multifrontal method for sparse LU factorization," *SIAM Journal on Matrix Analysis and Applications,* vol. 18, no. 1, pp. 140-158, 1997.

[34] Q. Gu, M. Barbato and J. P. Conte, "Handling of Constraints in Finite Element Response Sensitivity Analysis," *Journal of Engineering Mechanics,* vol. 135, no. 12, pp. 1427-1438, 2009.

[35] F. Rasmussen, M. H. Hansen, K. Thomsen, T. J. Larsen, F. Bertagnolio, J. Johansen, H. A. Madsen, C. Bak and A. M. Hansen, "Present Status of Aeroelasticity of Wind Turbines," *Wind Energy,* vol. 6, pp. 213-228, 2003.

[36] A. S. Obukhov, "The Relationship Between Stress and Deformation of Polymers in the Linear Stress State," *Mekhanika Polimerov,* vol. 1, no. 5, pp. 25-29, 1965.

Compensation Methods in Real-Time Hybrid Simulation

Jacob Høgh[1], Jacob Waldbjørn[2], Sebastian Andersen[2] and Christian Berggreen[1]
[1]*Department of Mechanical Engineering, Technical University of Denmark*
[2]*Department of Civil Engineering, Technical University of Denmark*

Abstract

Hybrid simulation is a sub structural testing method where a structure's behaviour is obtained by combining a numerical simulation with a physical experiment. This paper presents compensation methods in real-time hybrid simulation in order to account for compliance and inertia forces of the load train in the physical experiment. The compensators are developed for hybrid simulation with a complex load train transferring several degrees of freedom in the shared boundary. The compensator accounting for the compliance of the load train utilizes digital image correlation in an outer control loop. The inertia compensator is applicable for test setups where the load train has considerable mass compared to the specimen. Both compensation methods proved valid for lower frequencies i.e. f < 1.48Hz, but due to communication lag and limitations in computational resources it was not possible to increase accuracy for loading frequencies higher than 2.96Hz hybrid simulation.

Keywords: compensation methods, digital image correlation, finite element model, hardware-in-the-loop, hybrid simulation, real-time

Introduction

Hybrid simulation is a testing method where the main part of a structure is simulated while a subsection is tested in an experiment. The actions in the shared boundary between the simulation and experiment are fed between the two in an iterative process to simulate the behaviour of the entire structure [1]. The experiment is in this way implemented as a subroutine in the numerical calculation. Hybrid simulation is a well proven simulation method for structures with an overall linear response while a subsection behaves non-linearly. Hybrid simulation was developed during the 1970s for modelling structural behaviour in earthquake engineering [2]. Much effort has been made in earthquake engineering, especially for testing of damping systems for buildings [3], [4] and [5] or other earthquake protection [6], [7] and [8]. However, hybrid simulation has been applied to many different fields of engineering e.g. automobile [9], motor [10], robotics [11], space [12], train [13] and wind turbines [14] etc.

Much effort has been invested in developing and implementing explicit time integration schemes, e.g. central difference, operator splitting [15], direct integration algorithm [16], as well as implicit schemes, e.g. unconditionally stable implicit scheme [17], generalized alpha methods [18] and others. Furthermore, compensation methods to accommodate for the delay in the transfer system has been developed and implemented in hybrid simulation, e.g. feed-forward phase lead compensator and restoring force compensator [19], the improved adaptive inverse technique [20], prediction by third order polynomial fitted to previous displacement values [21], a discrete third order inverted compensator [22].

Hybrid simulation is therefore a well proven sub-structural testing method. However, in all the mentioned studies the focus has been on a fairly simple connection between the numerical model and the physical experiment, the so called shared boundary. This limits hybrid simulation to testing of structures where the shared boundary is made up of a hinge or other simple fixtures so that the actions from the experiment are easily translated to the numerical model and vice versa, this being the case when testing e.g. earthquake damper [23]. In the study presented in this paper, the authors seek to broaden the application of hybrid simulation to structures with a more complex shared boundary between the numerical model and physical experiment. This being the case in structures where no clear mechanical connection is dividing the structure in the physical experiment and numerical model, formerly referred to as single component hybrid simulation [24]. In this type of testing the number of degrees of freedom in the shared boundary is in principal infinite and the transferring and monitoring of actions between numerical model and physical experiment therefore not trivial [25].

The main focus of this paper is to develop compensation methods for hybrid simulation of a structure with complex shared boundary. As mentioned before this setup requires a comprehensive load train and the compliance and inertia forces of this therefore becomes an issue during dynamic testing. The compliance problem is solved by measuring the displacements directly on the specimen and correcting the applied displacement in an outer control loop similar to the one developed in [26] except here, the displacements and rotations are measured by digital image correlation (DIC) and the trigonometric relation between the shared boundary and actuators different. The inertia force due to the mass of the load train is compensated for by measuring the accelerations, deriving the inertia forces and subtracting them from the restoring forces. The compensators are tested in a real-time hybrid simulation using the central difference method for time integration, a Lagrange polynomial [27] extrapolator for the command signal and an single order direct inverted compensator [28] to account for the transfer system delay. The hybrid simulation is conducted on a glass fibre reinforced polymer (GFRP) beam clamed in on end and free in the other.

Test setup

The full structure selected for the analysis was a GFRP (Glass Fibre Reinforced Polymer) composite box girder clamped at one end and loaded vertically by an actuator at the tip. Two holes were made in the sides of the structure of length 590mm and height 45mm in order to weaken the shear stiffness thereby yielding non-linear stress strain behaviour due to large strains. The dimensions of the beam are presented in Fig. 1.

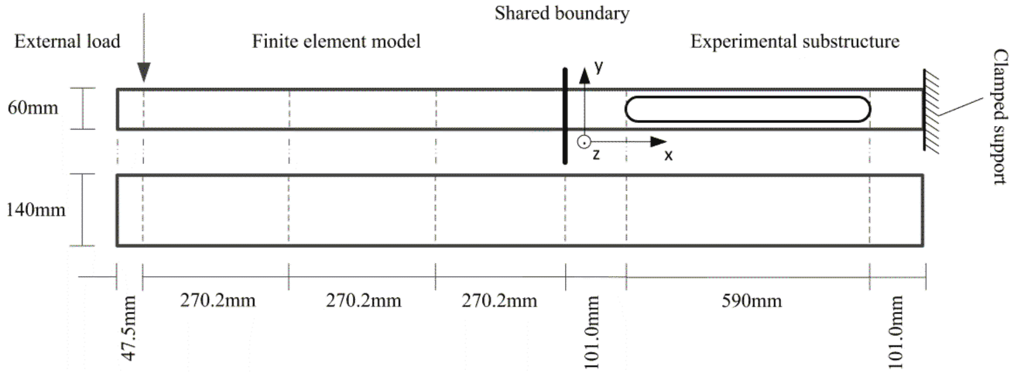

Fig. 1 The dimensions of the full structure that is separated in numerical model and Experimental subsection

In the hybrid simulation the experimental subsection consist of the beam from the clamped support and 792mm towards the tip, cf. Fig. 1. The remainder of the beam is modelled numerically and due to the lack of boundary conditions statically under determinate, however the model is restrained by the restoring forces from the experimental substructure iteratively fed into the finite element model. The experimental setup for the hybrid simulation is presented in Fig. 2 (a) and (b). The transition zone between the shared boundary and the load train of 108mm is selected in order to ensure that any stress concentrations from the load train, is not measured in the shared boundary by the DIC system.

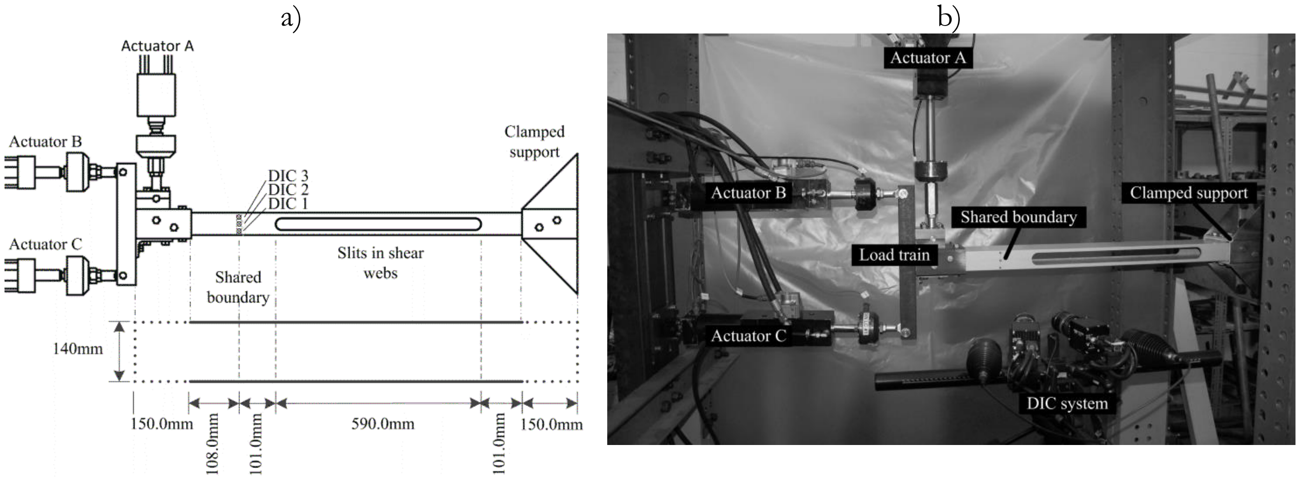
a)
b)
Actuator A
Actuator B
Actuator C
Clamped support
DIC 3
DIC 2
DIC 1
Slits in shear webs
Shared boundary
140mm
150.0mm
108.0mm
101.0mm
590.0mm
101.0mm
150.0mm
Actuator A
Actuator B
Clamped support
Shared boundary
Load train
Actuator C
DIC system

Fig. 2 a) Sketch of experimental subsection, with the three DIC measurement points at the shared boundary, and a 108mm transition zone between the experimental subsection and the load train b) picture of the experimental setup

Material properties

The material properties of the structure have been determined for another specimen from the same batch of the pultruded GFRP beam, cf. [25]. The stiffness was determined in accordance with D3039/D3039M – 08 [29] and D5379/D5379M – 12 [30]. The 1 direction is longitudinal of the beam, 2-direction is in-plane perpendicular.

Table 1 stiffness properties of the composite

E_1 [GPa]	E_2 [GPa]	ν_{12} [-]	ν_{21} [-]	G_{12} [GPa]	G_{21} [GPa]
28.36	9.96	0.23	0.08	3.41	3.06

The characteristic material strengths are specified in the Fiberline Composites A/S manual [31].

Table 2 characteristic strengths of pultruded glass fiber beam

Property	-	Unit
Tensile 0°	240	MPa
Tensile 90°	50	MPa
Compression 0°	240	MPa
Compression 90°	70	MPa
Shear	25	MPa
Mass	1825	kg/m^3

The dynamic properties of the structure are determined by a modal analysis of the reference structure. The natural frequencies were determined to: f_1 = 8.90Hz and f_2 = 52.59Hz, for the first and second vertical bending modes. The natural frequencies was later determined in a vibration test, where the full structure was stroke by a hammer and the accelerations was measured by an accelerometer connected to a vibration meter and logged by a A/D instrument. The frequencies was determined to f_1 = 7.40Hz and f_2 = 47.3Hz. The first natural frequency is used as a reference for the hybrid simulation hence the tests are performed with and external loading, cf. Fig. 1, with frequency at: 1%, 10%, 20%, 30% and 40% of the first natural frequency.

Test equipment

The hybrid simulation program is running on a LabVIEW compact Rio board NI9073, that send command signals a PID (Proportional-Integral-Derivative) controller by LabVIEW output module NI9263 16bit resolution and 100kHz signal generation frequency [32]. The signals from the controller and DIC system is input by a LabVIEW NI9205 module with 16bit of resolution and 250kHz acquisition frequency [33]. The PID controller is an MTS (Material Testing Systems, 14000 Technology Drive, Eden Prairie, MN USA 55344) TestStar II controller with three channels and 3.0kHz command signal generation. The hydraulic actuators are: one MTS ±25kN actuator with a ±25kN load cell and LVDT (Linear Variable Differential Transducer) with static and dynamic stroke of 182.9mm and 152.4mm, respectively, and two ±5kN actuators with ±5kN load cells and LVDTs with static and dynamic stroke of 114.3mm and 101.6mm, respectively.

The DIC (Digital Image Correlation) system used is ARAMIS 12M by GOM (Gesellschaft für Optische Messtechnik mbH, Mittelweg 7-8, 38106 Braunschweig, Germany). The DIC system is stereo system with two CCD (Charged-couple Device) chip 12 megapixel cameras: 4096pix x 3072pix, and 24mm focal length Titanar lenses. The system is setup 295mm from the specimen with 108mm between the cameras yielding a measuring volume of 200mm x 150mm, calibrated by a 175mm x 140mm calibration object. The DIC system runs the software PONTOS Live vs. 8 capable of performing point measurements, process and send data real-time, via Ethernet cable using UDP (User Datagram Protocol) and SCPI (Standard Commands for Programmable Instruments) protocol, cf. [34] and [35].

The vibration meter determining the Eigen frequencies of the specimen is a Vibration Meter Type 2511 [36] from Brüel & Kjær (Brüel og Kjær Sound & Vibration Measurement A/S, Skodsborgvej 307, 2850 Nærum, Denmark), measuring accelerations in the range: [0.3Hz ; 15kHz].

Finite Element Modelling

A finite element model to simulate the numerical substructure is organized. The model is made with plane Euler-Bernoulli elements containing two nodes with two transversal and one rotational degree of freedom in each node. Linear shape functions are used to model the horizontal element deformations and third order polynomials are used to model the transverse deformations and rotations. Full details about the element are given in [37]. The equations of motion in the numerical simulations are written on the form:

$$\boldsymbol{M}_n\ddot{\boldsymbol{x}} + \boldsymbol{C}_n\dot{\boldsymbol{x}} + \boldsymbol{Q}_n + \boldsymbol{R} = \boldsymbol{F} \tag{1}$$

Where $\mathbf{M}_n$ is the mass matrix, $\mathbf{C}_n$ the damping matrix, $\mathbf{Q}_n$ the internal restoring forces and $\mathbf{F}$ the external load. All of these refer to the numerical model, indicated by the subscript *n*. The vector $\mathbf{R}$ represents the inertia, damping and restoring forces of the physical substructure, measured by the actuators.

The numerical part is modelled with 20 beam elements and solved by use of the central difference method, which is an explicit time integration scheme, with a time step of $\Delta t = 10^{-2}$ s. However, in order to minimize the computational time, the equations of motion in eq. (1 are projected onto a reduced basis. In the present case is used a Taylor basis with one linear mode and one modal derivative, cf. [38] for details. However, as the Euler-Bernoulli element does not include shear flexibility, which has a significant influence on the response, the modes used in the Taylor basis introduce some discontinuities in, among other thing, the rotations at the common interface. The consequences of this are discussed in more detail in [38]. Furthermore a damping ratio of 20% is included in the first mode to remove the high frequency excitation of the modes.

Hybrid simulation setup – multi rate approach

A substructural test of the GFRP composite box girder is conducted using a multi-rate real-time hybrid simulation (mrRTHS) approach. Here the numerical and experimental substructure is operated at two different rates to optimize the available computational resources and enhance flexibility to the architecture of the hybrid simulation communication loop, [27], [39], [40]. The overall framework of the mrRTHS communication loop contains two loops named main- and outer-loop with an execution rate of $\triangle T = 0.020$ sec (50Hz) and $\delta t = 0.002$ sec (500Hz) respectively cf. Fig. 3.

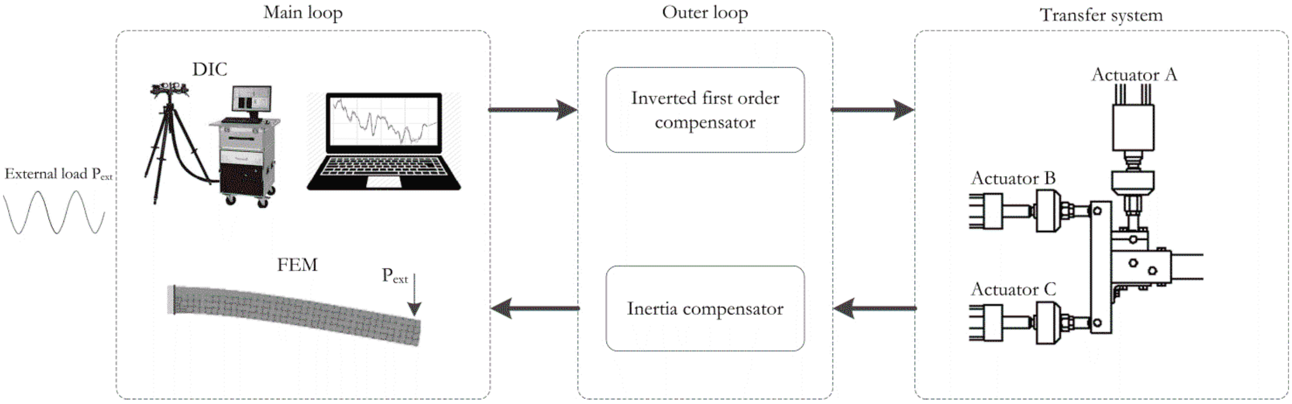

Fig. 3 simplified schematic block diagram representing the overall architecture of the mrRTHS communication loop

The strategy is handled through the real-time target (National Instruments cRIO – 9074) which is capable of providing deterministic and real-time control and monitoring capabilities [41]. Through the main loop the numerical model is discretized using plane Euler-Bernoulli elements (see chapter: “Finite Element Modelling”) to compute the next displacement signal based on the external load and last available restoring force received from the experimental substructure. Next the DIC Compensator (see chapter “Real-Time Digital Image Correlation Compensator”) is implemented to enhance the tracking performance between the shared boundary on the experimental substructure and displacement signal. By the current and three previous displacement data points a finer control signal is generated with the time step δt, using a third order polynomial algorithm [42]. The numerical substructure, DIC compensator and extrapolator are executed with a sampling rate of $\triangle T$ by the 400MHz on-board single core processor which is embedded in the real-time target. Through the outer loop the control signal is compensated to account for actuator dynamics using an inverted first order compensator [43] and transmitted to the transfer system by an analogue signal with the time step δt. Here the transfer system consists of a PID controller and three servo hydraulic actuators named: A, B and C cf. Fig. 3. The restoring force from the experimental substructure is acquired and in order to remove the dynamic effects of the load train from the restoring force the Inertia Compensator (see subchapter “Real-Time Inertia Force Compensator”) is implemented. The inverted first order compensator, communication interface between the real-time target and transfer system and Inertia Compensator is executed with an execution rate of δt by the Field Programmable Gate Array (FPGA) which – like the single core real-time processor - is embedded in the real-time target. Thus the main- and outer-loop is dedicated its own processor to allocate computationally independent and separate resources. The program was developed in [44].

Real-Time Digital Image Correlation Compensator

From previous research [25] it was documented that the compliance in the load train gave rise to a large error between the commanded displacement in the actuators and the displacements measured at the shared boundary directly on the specimen. A real-time digital image correlation compensator is therefore utilized in the hybrid simulation. The compensator is referred to as: *DIC Compensator.*

The displacement in the shared boundary is calculated by three measurement points, assuming linear cross sectional deformation. This allows for 1st order shear deformations of the cross section, cf. Timoshenko beam theory. The x- and y-displacement of the shared boundary is calculated as the average of the three points, while the rotation is calculated by the angle between the top and bottom point. The x, y and z- axis follows the coordinate system specified in Fig. 1. The u_x, u_y, u_z and φ_z are the displacements in the x-, y- and z-directions and rotation around the z-axis, respectively. The n denotes the DIC point number, cf. Fig. 2.

$$\boldsymbol{D} = [u_x\ u_y\ u_z\ \varphi_z] \tag{2}$$

$$u_x = \frac{\sum_1^N u_{x,n}}{N}, u_y = \frac{\sum_1^N u_{y,n}}{N}, u_z = \frac{\sum_1^N u_{z,n}}{N}, \qquad \text{for}\, n = 1,2,3 \tag{3}$$

$$\varphi_z = \text{Arctan}\left(\frac{u_{x,3} - u_{x,1}}{u_{y,1} - u_{y,3}}\right),\ \text{for} -\frac{\pi}{4} < \varphi_z < \frac{\pi}{4} \tag{4}$$

The DIC Compensator is applied in an outer control loop structure; cf. eq. (5) (the inner control loop being the PID loop for the LVDT and servo valve). The displacement commanded to the hybrid simulation program for the n'th iteration is named $\mathbf{D}_c(n)$. This is determined by the desired displacement with zero error, $\mathbf{D}_{c0}(n)$ added the error from the previous iteration $\mathbf{e}(n-1)$ multiplied by a proportional gain $\mathbf{K}_{DIC}$. The error in the previous iteration $e(n-1)$ is determined by the previous command signal $\mathbf{D}_c(n-1)$ and the feedback displacement measured with the DIC system $\mathbf{D}_{DIC}(n-1)$. It is noted that the displacement is a vector of horizontal and vertical displacements and rotations around the z-axis, $\mathbf{D} = [x\ y\ \varphi_z]$. The displacements and rotations are transformed into displacements in the actuators by a trigonometric relation [25].

$$\boldsymbol{D}_c(n) = \boldsymbol{K}_{DIC}\boldsymbol{e}(n-1) + \boldsymbol{D}_{c0}(n) \tag{5}$$

$$\boldsymbol{e}(n-1) = \boldsymbol{D}_c(n-1) - \boldsymbol{D}_{DIC}(n-1) \tag{6}$$

A similar approach has previously been applied hybrid simulation [26] using LVDTs to measure six degrees of freedom (three displacements and three rotations) instead of DIC. The accuracy of the DIC system is evaluated by the standard deviation of the noise of the measured displacements and rotation; cf. Table 3. The error was measured in a noise test with zero displacement applied the specimen.

Table 3 standard deviation (SD) of error of displacements and rotation

SD u_x [µm]	SD u_y [µm]	SD φ_z [°]	SD u_z [µm]
0.419	4.157	1.108e-3	0.777

The communication delay between the DIC system and the hybrid simulation program is 160ms from the data is measured by the cameras until the data is processed and arrives in the hybrid program. The specimen is loaded by a sinusoidal displacement and it is desirable to compensate for a difference between the command and feedback signal as close to the current value as possible, since the error between command and feedback might be must different at the peaks of the since wave than at the zero point. In Table 4 the percentage of the loading period is plotted for five frequencies for the delay of 160ms.

Table 4 the 160ms delay's portion of the sine period for 5 frequencies

Frequency [Hz]	Period [ms]	Delay relative to period [%]

0.074	13513	1.2
0.74	1351	11.8
1.48	676	23.7
2.22	450	25.6
2.96	338	47.3

Real-Time Inertia Force Compensator

In order to compensate for the inertia force from the mass of the load train an inertia force compensator is developed. In the remaining paper the compensator is referred to as; *Inertia Compensator*. The compensator calculates the inertia force of the load train by the mass and the acceleration derived from the double differentiated command signal. This force is subtracted the force measured in the load cells thereby obtaining the restoring force from the specimen.

$$F(t) = m\frac{d^2x}{dt^2} \tag{7}$$

The differentiation is performed by finite differencing.

$$F(t) = m\frac{d^2x}{dt^2} \cong m\frac{\Delta^2 x}{\Delta t^2} = m\frac{x_2 - 2x_1 + x_0}{\Delta t^2} \tag{8}$$

The mass of the load train was determined, by a oscillation test, where the load train oscillates vertically at 2.96Hz with 9.25mm amplitude, to m = 25.68kg, without any specimen installed. The vibration test also shows whether the load train runs smoothly. The force as function of acceleration is plotted in Fig. 4. Ideally the trend should be linear; however a shift in the force is observed when the oscillations change direction. This shift is most likely caused by Coulomb damping due to friction in the swivels and hinges connecting the actuators to the load train and supports.

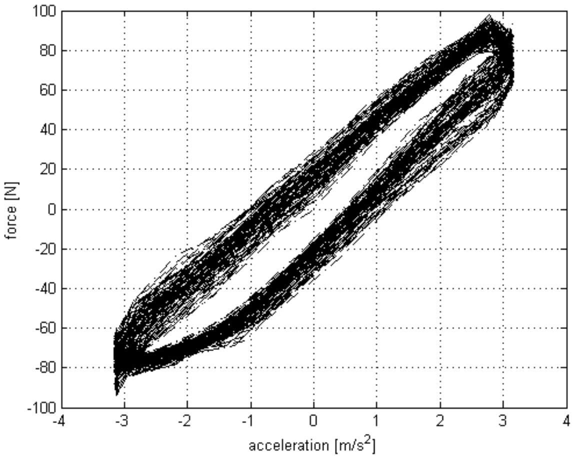

Fig. 4 Oscillations of the load train at 2.96Hz frequency and 9.25mm amplitude

In order to demonstrate the necessity of the Inertia Compensator the inertia force is calculated for the frequencies and amplitude used in the hybrid simulation. This is done by double differentiating the sinusoidal displacement function and finding the max acceleration and multiplying by the mass.

$$x(t) = A\sin(2\pi f t) \Longrightarrow \tag{9}$$

$$F_{max}(t) = -4A\pi^2 m f^2 \tag{10}$$

The inertia force of the load train is compared to the section forces at the shared boundaries, i.e. if the inertia force of the load train is comparable to the restoring force of the specimen the inertia force required. The vertical restoring force from the specimen is determined by the external load applied the structure in the reference test. The forces are plotted in Fig. 5. It is observed that the inertia force is increasing for higher frequencies while the section force is decreasing towards the natural frequency of the composite beam. Fig. 5 shows the necessity for Inertia Compensation for tests at higher frequencies e.g. f > 0.5Hz.

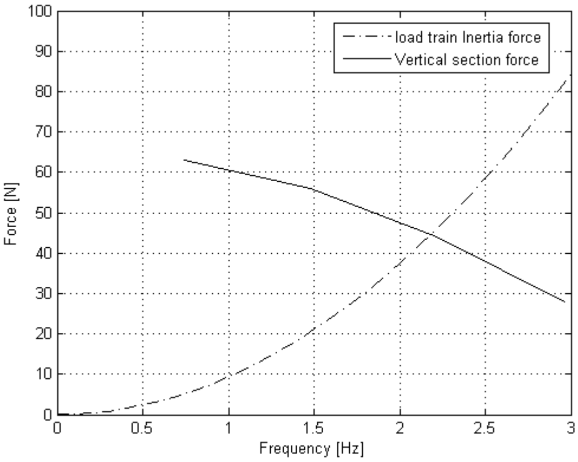

Fig. 5 inertia force of a load train evaluated for the frequencies and amplitudes used in the hybrid simulation

Results

No compensation

In order to evaluate the need for compensators in the hybrid simulation a hybrid simulation was run at different frequencies without DIC or Inertia Compensation. In Fig. 6 the x-, y- displacements and rotation around the z-axis in the shared boundary are plotted for a loading frequency of 0.074Hz. The standard deviation of the error between the command signal and feedback for all 5 frequencies are listed in Table 5. For evaluation of error the maximum amplitude of each DOF is listed in the table.

(a) (b)

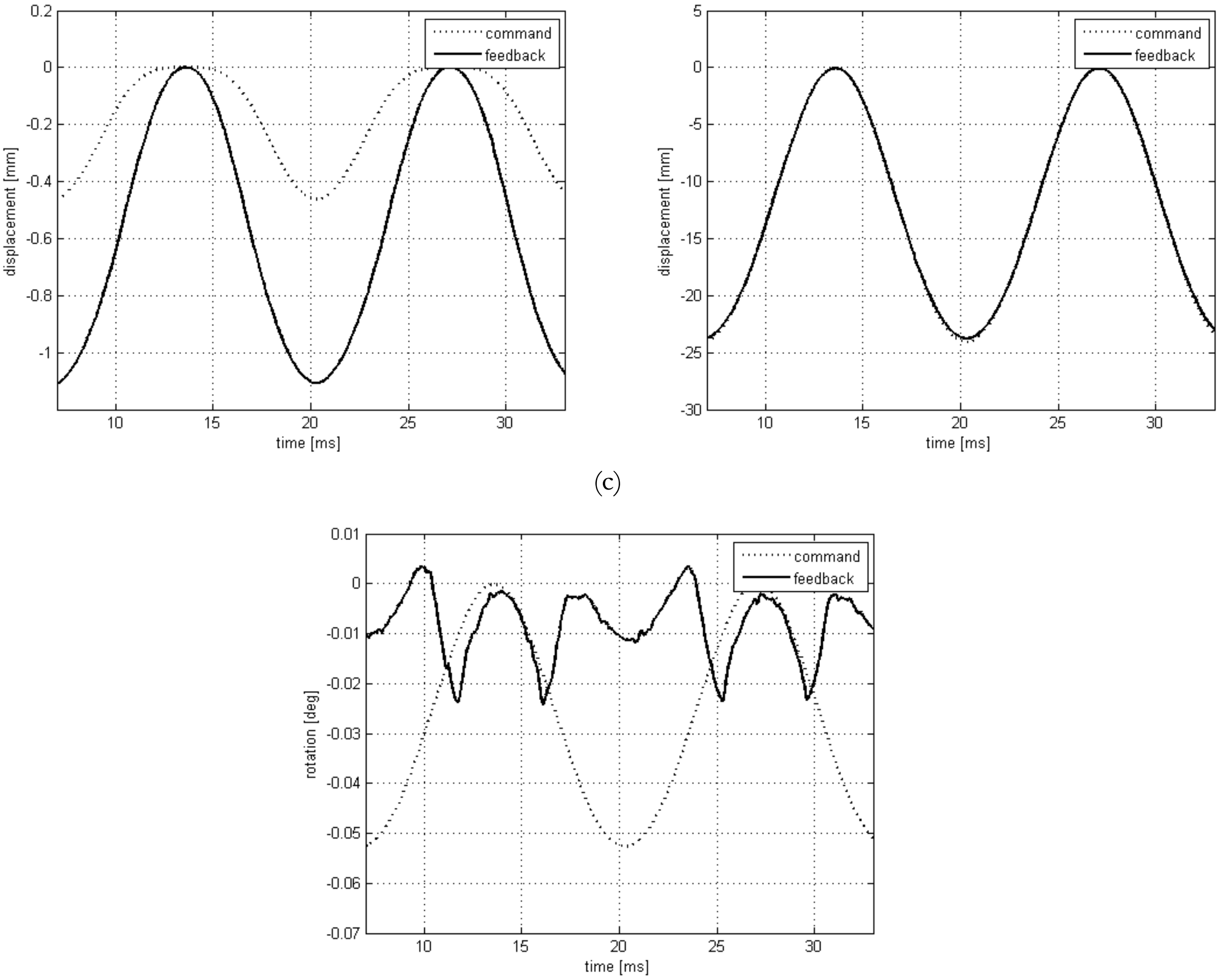

(c)

Fig. 6 Displacement of the shared boundary for a loading frequency of 0.074Hz, command and feedback for the three DOFs a) u_x, b) u_y c) φ_z

The results show poor correspondence between the command and feedback for the displacements and rotations except for y-displacements. However, for higher frequencies the y-displacement error also becomes considerably, e.g. at f = 2.96Hz the error is 24.5% of the amplitude.

Table 5 standard deviation (SD) of error between command and feedback and amplitude of command for comparison, no compensation

Frequency [Hz]	SD u_x [mm]	SD u_y [mm]	SD φ_z [deg]
0.074	0.2368	0.9339	0.0204
0.74	0.2313	1.4847	0.0203
1.48	0.2139	1.7797	0.0207
2.22	0.2175	4.7717	0.0234
2.96	0.1965	5.8946	0.0249
Amplitude of command signal	0.4626	24.0869	0.0526

DIC Compensator

In order to accommodate for the compliance of the test rig a DIC Compensator is applied. The DIC system measures the deformations in the shared boundary in three points and then calculates the overall x and y displacements and the rotation around the z axis. The command and DIC feedback signal is plotted in Fig. 7 In these tests the gain was set to K_{DIC} = [0.0075 ; 0.10] before the loop became unstable.

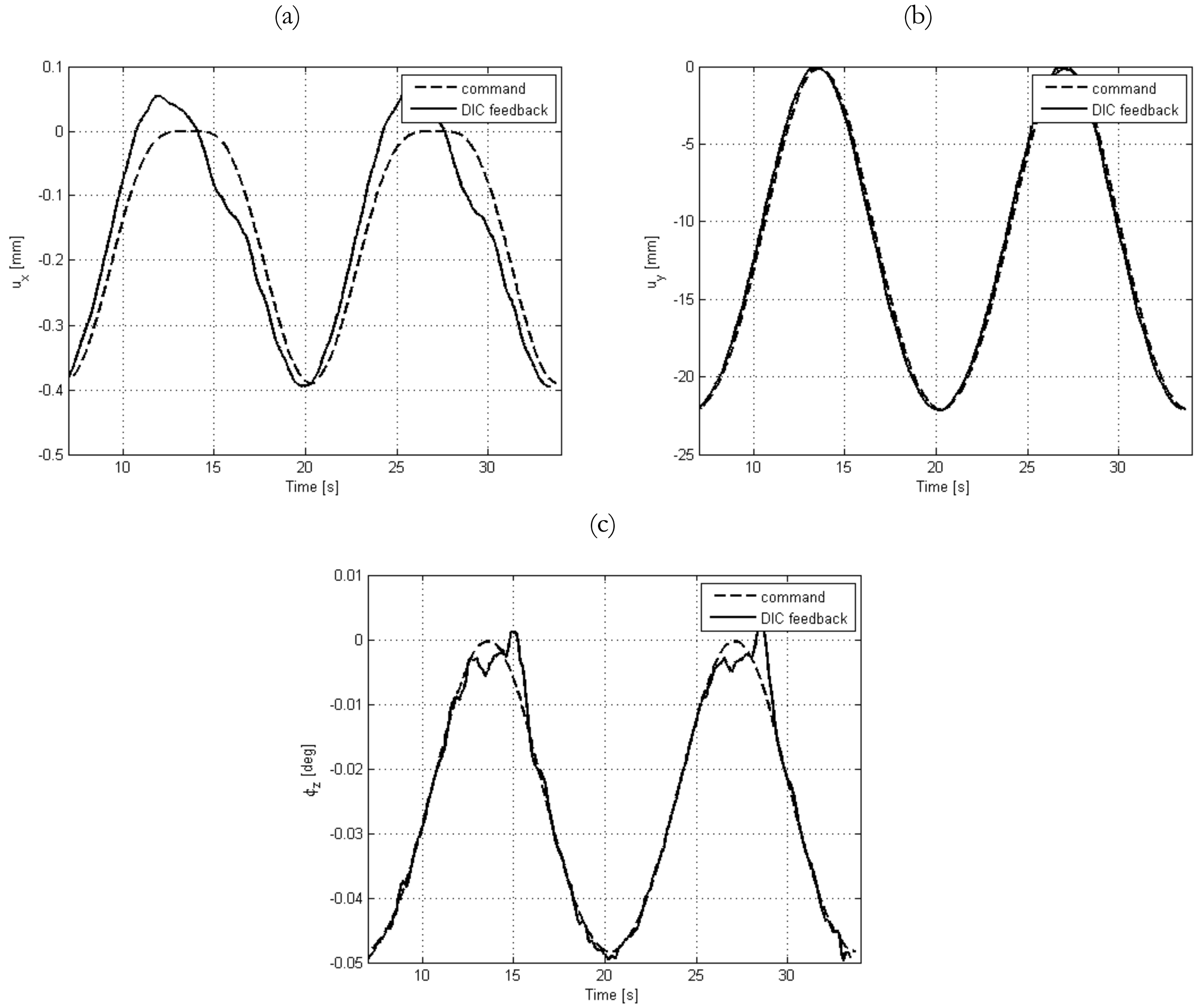

Fig. 7 Displacement of the shared boundary for a loading frequency of 0.074Hz, command and feedback for the three DOFs a) displacement u_x, b) displacement u_y c) rotation φ_z

Table 6 standard deviation of error between command and feedback, DIC compensation

Frequency [Hz]	SD u_x [mm]	SD u_y [mm]	SD φ_z [deg]
0.074	0.0403	0.5383	0.0038
0.74	0.2238	0.4940	0.0099
1.48	0.1899	1.3850	0.0130
2.22	0.1616	3.8033	0.0166
2.96	0.1680	5.7519	0.0203
Amplitude of command signal	0.4626	24.0869	0.0526

In Table 6 the standard deviation of the error between the command signal and feedback DIC measurements are presented for the five loading frequencies. In order to evaluate the error the amplitude of displacements are written for each DOF. It is observed that for 0.074Hz the error for all DOFs are less than 9% while for 2.96Hz the error is higher than 23%. The improvement by DIC compensation is evaluated by comparing the command versus feedback error when not using DIC compensation to the same error when using DIC compensation. The improvement in percent is plotted in Fig. 8. It is observed that the DIC Compensator improves the correlation between command and feedback signal for all frequencies for the displacements and rotation in the shared boundary. The improvement is decreasing for higher loading frequencies.

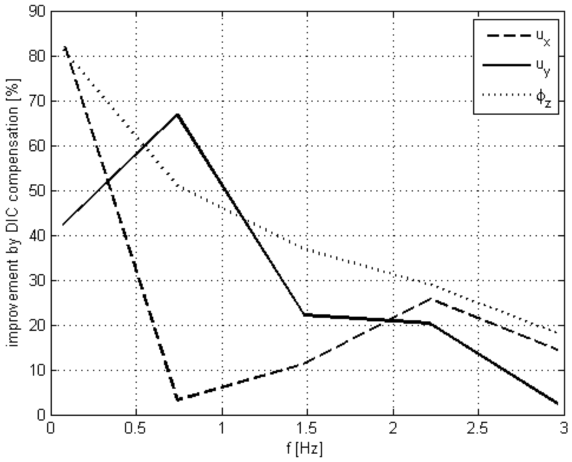

Fig. 8 Improvement by DIC compensation in terms of standard deviation of error between the command and feedback

Inertia compensator

The inertia force is calculated by the acceleration which is determined by double differentiation of the displacement command signal, cf. eq. (8). In Fig. 9 the restoring force from the specimen is plotted with and without the Inertia Compensator for four frequencies; 0.74Hz, 1.48Hz, 2.22Hz and 2.96Hz.

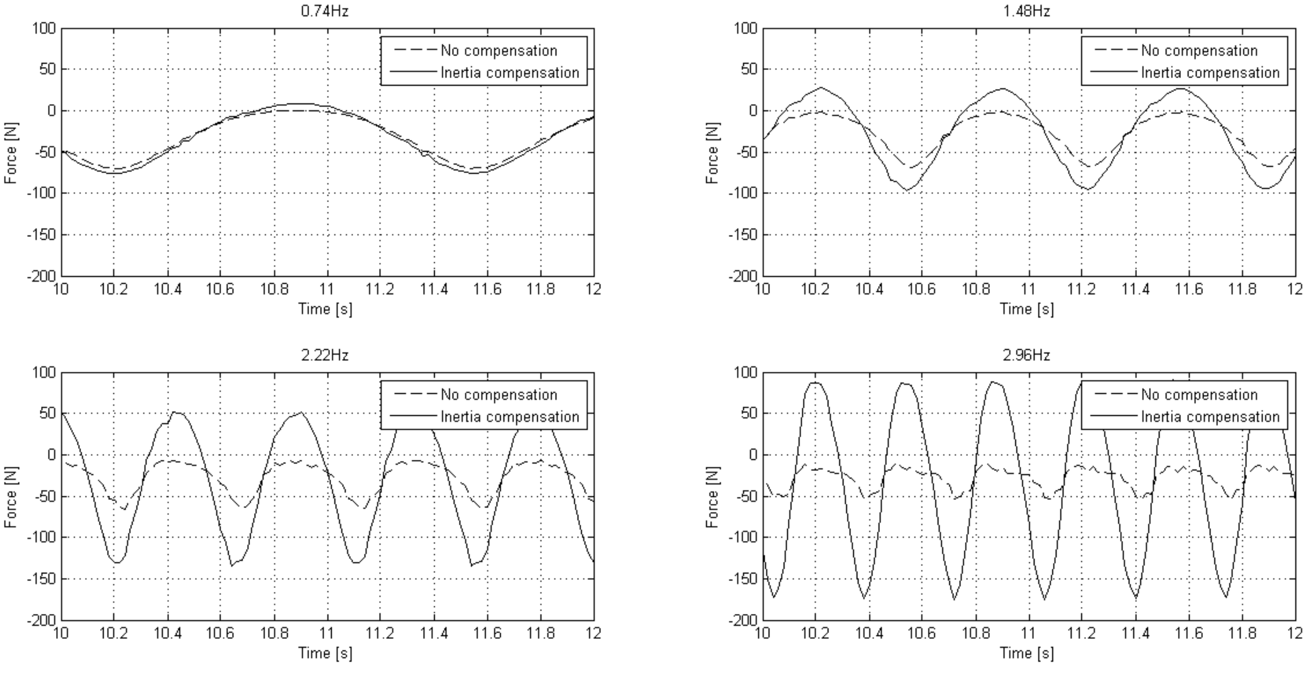

Fig. 9 The restoring force in the hybrid simulation with and without Inertia Compensation for four loading frequencies

It is observed that the inertia force of the load train is insignificant in the slow tests i.e. 0.074Hz and 0.74Hz, while at the highest frequency of 2.96Hz the force measured in the load cell is only 19.2% of the force acting on the specimen, cf. Table 7. The remaining force acting on the specimen is from the inertia force of the load train. The inertia force of the load train must therefore be included in the hybrid simulation for higher loading frequencies.

Table 7 comparison of force with and without compensation

Frequency [Hz]	Force Amplitude No Inertia Compensation [N]	Force Amplitude Inertia Compensation [N]	Uncompensated force as ratio of compensated force [%]
0.074	40.1	40.9	98.1
0.74	42.3	49.0	86.4
1.48	41.0	69.3	59.1
2.22	39.5	107.1	36.9
2.96	28.8	150.1	19.2

Due to compliance of the load train the displacement of the shared boundary was not as commanded by the hybrid testing program, cf. Table 6. This gave rise to an error in the inertia force, since this was calculated on the basis of the command signal. A hybrid simulation was therefore performed with both the Inertia Compensator and DIC Compensator utilized.

Combined Effect of Inertia- and DIC Compensator

Both compensators are applied the hybrid simulation for the five tested frequencies. The command and feedback signal is plotted in Fig. 10 for the shared boundary between the finite element model and the experimental subsection for the loading frequency of 0.074Hz. For the remaining four frequencies the standard deviation of the error between command and displacement is listed in Table 8.

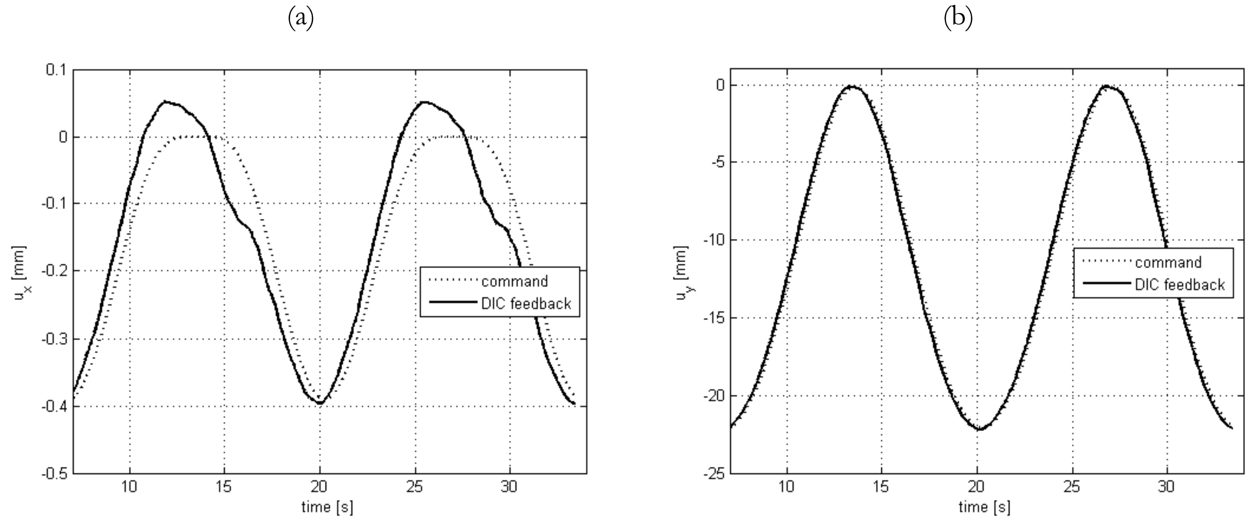
(a)

(b)

(c)

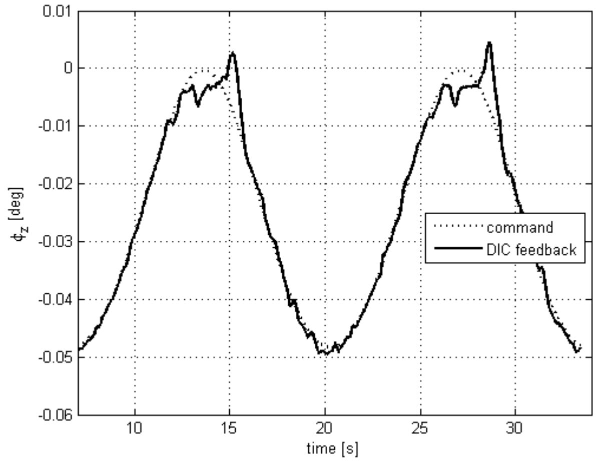

Fig. 10 command vs feedback displacements and rotation of the shared boundary for the three DOFs a) u_x, b) u_y c) φ_z

Table 8 standard deviation of error between command and feedback, inertia and DIC compensation

Frequency [Hz]	SD u_x [mm]	SD u_y [mm]	SD φ_z [deg]
0.074	0.0488	0.1118	0.0033
0.74	0.2239	0.6244	0.0100
1.48	0.1921	1.4533	0.0132
2.22	0.1642	4.0538	0.0173
2.96	0.1979	6.8682	0.0221
Amplitude of command signal	0.4626	24.0869	0.0526

When comparing the standard deviation of error with and without the Inertia Compensator and DIC Compensator, it is seen that using the Inertia Compensator together with DIC compensation increases the error slightly. This is most likely caused by the increasing noise in the test the double differentiation used in the inertia Compensator induces, cf. eq. (8). In Fig. 10 some oscillations of the rotation is observed which is due to the P-gain of the DIC Compensator, cf. eq. (5) and (6), is close to going instable.

Total errors: Communications lag from DIC, noise in measurements from DIC system cf. Table 3, high frequency vibrations in the specimen, noise due to finite differencing of the displacement signal, cf. eq. (8).

Discussion

Digital image correlation compensator

The DIC Compensator shows good correlation between command and feedback for lower frequencies i.e. $f < 1.48$ Hz for displacements and rotation, cf. Fig. 8. However, at higher frequencies the improvement goes towards zero compared to no compensation, cf. Fig. 8. When observing the command vs feedback for the different frequencies it is seen that the lag between command and feedback becomes a bigger problem for higher frequencies, cf. Table 4. The problem occurs when attempting to compensate the command signal at the top of a peak with an error missing at the bottom of the valley of the sine wave. This problem could be solved by decreasing the communication delay between the DIC system and the hybrid simulation program. Alternatively, extrapolation methods could be applied the DIC Compensator to predict the error instead of using it directly. However, for the given tests this was not possible due to limited computational capacities of the hardware.

Another issue with the DIC Compensator was the P-gain approach applied to compensating the command signal, cf. eq. (5) and (6). Desirably the gain K_{DIC} should be set to approximately 1.0, however that caused the actuators to change position too violently which yielded noise in the restoring forces, which then led to instability of the hybrid simulation. Therefore the gain was set in the range of K_{DIC} = [0.0075 ; 0.10], due to these fairly low gains, together with the communication lag, the program was simply not able to reach the desired amplitudes at higher frequencies i.e. $f > 1.48$Hz.

Inertia Compensator

The results shows that the Inertia Compensator is crucial for running real time hybrid simulation with a load train with high mass compared to the specimen. The inertia force compensator shows that at higher frequencies > 1.48Hz the compensator must be included since the inertia force accounts > 40% of the force measured in the actuator.

The accuracy of the Inertia Compensator as it is designed depends on the accuracy of the feedback vs command signal, since the compensator uses commanded displacements to calculate inertia force of the load train. In the tests conducted it was possible to get a high degree of correlation between the command and feedback displacement for lower loading frequencies < 1.48Hz. In order to improve the accuracy of the inertia force it could be calculated by the feedback displacement instead of the command. However, this will result in a high degree of noise in the inertia force since it is calculated on the basis on double differentiated feedback displacements, which will always be noisier than a command signal. To get rid of the noise one could filter the displacements but that takes computational resources from running the hybrid simulation. In the tests conducted here this was not possible due to the capacity of the hardware and the degree of accuracy of the finite element model. The tests therefore shows that the best approach is to optimize the correlation between command and feedback displacement e.g. by DIC compensation or others and thereafter use the command signal to calculate the accelerations and thereby the inertia forces. In this way the Inertia Compensator is as accurate as possible while releasing as much computational resources for other tasks in the hybrid loop i.e. increase accuracy of the FEM model, time integration scheme etc.

It is noted that the Inertia Compensator is only applied vertical restoring force and not the horizontal force or moment. This is due to the horizontal inertia force and moment is insignificant to the loads applied the specimen due to the very small displacements and rotations even for large amplitude tests i.e. $y > 20$mm, $x < 1$mm, $\varphi_z < 0.1°$, at least for frequencies in the given range [0 ; 2.96Hz]. Furthermore the stiffness of the specimen in the longitudinal direction is much higher than in the vertical direction and eventual inertia forces from the load train has therefore much lower effects on the specimen.

Combined effect of Digital Image Correlation and Inertia Compensator

In order to achieve compensate for both compliance and inertia force of the load train both compensators was applied simultaneously, cf. Fig. 10. The DIC Compensator should ideally be able to increase the accuracy of the inertia Compensator since an error in the inertia compensator was the feedback displacement not following the command at higher frequencies i.e. 1.48Hz, cf. Table 5. The DIC Compensator should be able to solve this problem. The DIC Compensator did indeed improve the accuracy of the feedback signal for lower frequencies, however for higher frequencies little improvement was observed; cf. Table 6, due to the communication lag.

The main improvements to be made to the hybrid simulation setup presented, is to decrease communication lag between DIC system and hybrid simulation program by e.g. using another DIC system with less communication lag. Another improvement would be to increase the computational resources of the hybrid simulation program by utilizing other computational hardware. In this way high pass filtering could be applied to the load and DIC displacement feedback signals. The P-gain, cf. eq. (5) and (6), of the DIC Compensator could thereby be increased without causing instability of the program, and lower errors between command and feedback be obtained. This would also improve the inertia compensator that uses the command signal.

Conclusion

This study shows the necessity for compensation methods in real time hybrid simulation in the case of high compliance and mass of the load train compared to the specimen tested. Two compensation methods are applied: DIC compensation, to account for compliance of the load train and Inertia Compensation to account for the mass of the load train. The DIC Compensator proved valid for all tested frequencies with higher improvement for lower frequencies. For higher frequencies i.e. f > 1.48Hz, the compensator is converging towards zero improvements, cf. Fig. 8. This is assumed to be due to the communication lag between the DIC system and hybrid program. The Inertia Compensator proved valid, however for higher frequencies i.e. f > 1.48Hz the error between the command and feedback displacements led to a too high error in the inertia compensator. The two compensators were implemented in the hybrid simulation program simultaneously in order to accommodate for the compliance of the load train and thereby also improve the accuracy of the inertia force in the inertia compensator. The combined effect of the compensators improved the accuracy of the hybrid simulation for low frequencies e.g. f < 1.48Hz. However, for higher frequencies the compensators need improvements before fully valid. The main improvements suggested are: minimizing the communication delay to the DIC system, filtering the noise from the Inertia Compensator and increasing the amount of computational resources in the CPU running the simulation. The latter would allow for smaller time steps and higher degree of filtering of the measurements before used in the compensators.

Acknowledgement

The authors acknowledge the funding by the Danish Centre for Composite Structures and Materials for Wind Turbine Blades (DCCSM), which is funded by the Danish Council for Strategic Research within Sustainable Energy and Environment (grant 09-067212). Furthermore the authors acknowledge Fiberline Composites A/S for providing the GFRP beams tested in the hybrid simulation.

References

[1] M. Nakashima, J. McCormick and T. Wang, "Chapter 1 Hybrid simulation: A historical perspective," in *Hybrid Simulation - Theory, Implementation and Applications*, London, UK, Taylor & Francis, 2008, pp. 3-14.

[2] K. Takanashi and M. Nakashima, "Japanese Activities on On-Line Testing," *Journal of Engineering Mechanics,* vol. 113, no. 7, pp. 1014-1032, 1987.

[3] Y. Chae, J. M. Ricles and R. Sause, "Large-scale rths of a three-story steel frame building with mr dampers," *Earthquake Engineering and Structural Dynamics,* vol. 43, no. 13, pp. 1915-1933, 2014.

[4] T. L. Karavalis, J. M. Ricles, R. Sause and C. Chen, "Experimental evaluation of the seismic performance of steel MRFs with compressed elastomer dampers using large-scale real-time hybrid simulation," *Engineering Structures,* vol. 33, pp. 1859-1869, 2011.

[5] J. E. Carrion, B. F. Spencer Jr. and B. M. Phillips, "Real-time hybrid testing of a semi-actively controlled structure with an MR-damper," in *American Control Conference*, St. Louis, MO, USA, 2009.

[6] M. Ito, Y. Murata, K. Hoki and M. Nakashima, "Online hybrid test on buildings with stud-type damper made of slitted steel plates stiffened by wood panels," in *12th East Asia-Pacific Conference on Structural*

Engineering and Construction, EASEC12, 2011.

[7] A. Jacobsen, T. Hitaka and M. Nakashima, “Online test of building frame with slit-wall dampers capable of condition assement,” *Journal of Constructional Steel Research,* vol. 66, no. 11, pp. 1320-1329, 2010.

[8] S. Plude, R. Christenson, Z. Jiang and S. J. Kim, “Real-time hybrid simulation of a complex bridge model with mr dampers using the convolution integral method,” *Smart Materials and Structures,* vol. 22, no. 10, 2013.

[9] K.-C. Lee, J.-W. Jeon, D.-H. Hwang, S.-H. Lee and Y.-J. Kim, “Development of Antilock Braking Controller Using Hardware In-the-Loop Simulatin and Field Test,” in *The 30th Annual Conference of the IEEE Industrial Electronics Society*, Busan, Korea, 2004.

[10] C. Dufour, T. Ishikawa, S. Abourida and J. Bélanger, “Modern Hardware-In-the-Loop Simulation Technology for Fuel Cell Hybrid Electric Vehicles,” in *2007 Vehicle Power and Propulsion Conference*, 2008.

[11] K. Osaki, A. Konno and M. Uchiyama, “Delay Time Compensation for a Hybrid Simulator,” *Advanced Robotics,* vol. 24, pp. 1081-1098, 2010.

[12] H. Yan, Z. Ye, D. Cong, J. Han and H. Li, “Space docking hybrid simulation prototype experiment system,” *Chinese Journal of Mechanical Engineering,* vol. 43, no. 9, pp. 51-56, 2007.

[13] A. Facchinetti and S. Bruni, “Hardware-in-the-loop hybrid simulation of pantograph-catenary interaction,” *Journal of Sound and Vibration,* Vols. 2783-2797, p. 331, 2012.

[14] W. Song and W. Su, “A wind turbine hybrid simulation framework considering aeroelastic effects,” in *Proceedings of the SPIE*, 2015.

[15] B. Wu, G. Xu, Q. Wang and M. Williams, “Operator-splitting method for real-time substructure testing,” *Earthquake Engineering and Structureal Dynamics,* vol. 35, no. 3, pp. 293-314, 2005.

[16] C. Cheng and J. M. Ricles, “Development of Direct Integration Algorithms for Structural Dynamics Using Discrete Control Theory,” *Journal of Engineering Mechanics,* vol. 134, no. 8, pp. 676-683, 2008.

[17] P.-S. B. Shing, M. T. Vannan and E. W. Carter, “Implicit time integration for pseudodynamic tests,” *Earthquake Engineering and Structural Dynamics,* vol. 20, pp. 551-576, 1991.

[18] J. Chung and G. M. Hulbert, “A Time Integration Algorithm for Structural Dynamics with Improved Numerical Dissipation: The Generalized-alpha Method,” *Journal of Applied Mechanics,* vol. 60, pp. 371-375, 1993.

[19] P.-C. Chen and K.-C. Tsai, “Dual compensation strategy for real-time hybrid testing,” *Earthquake Engineering and Structural Dynamics,* vol. 42, no. 1, pp. 1-23, 2013.

[20] C. Chen, J. M. Ricles and T. Guo, “Improved Adaptive Inverse Compensation Technique for Real-Time Hybrid Simulatino,” *Journal of Engineering Mechanics,* vol. 138, no. 12, pp. 1432-1446, 2012.

[21] T. Horuichi, M. Inoue, T. Konno and Y. Namita, “Real-time hybrid experimental system with actuator delay compensation and its application to a piping system with energy absorber,” *Earthquake Engineering and Structural Dynamics,* vol. 28, no. 10, pp. 1121-1141, 1999.

[22] B. M. Phillips and B. F. Spencer, “Model-based servo-hydraulic control for real-time hybrid simulatino,” Newmark Structural Engineering Laboratory, Urbana-Champaign, Illinois, USA, 2011.

[23] C. Chen, J. M. Ricles and T. L. Karavasilis, “Evaluation of a real-time hybrid simulation system for performance evaluation of structures with rate dependent devices subjected to seismic loading,” *Engineering Structures,* vol. 35, pp. 71-82, 2012.

[24] J. Waldbjørn, J. Høgh, C. Berggreen, J. Wittrup-Schmidt and K. Branner, “Hybrid Testing of Composite Structures with Single-axis Control,” in *The 19th International Conference on Composite Materials*, Montreal, Canada, 2013.

[25] J. Høgh, J. Waldbjørn, J. Wittrup-Schmidt, H. Stang and C. Berggreen, "Quasi-static single-component hybrid simulation of a composite structure with multi-axis control," *Strain,* vol. 51, pp. 459-473, 2015.

[26] B. F. Spencer, C.-M. Chang, T. M. Frankie and D. A. Kuchima, "Multiple Degrees of Freedom Positioning Correction for Hybrid Simulation," *Journal of Earthquake Engineering,* vol. 19, no. 2, pp. 277-296, 2015.

[27] P. A. Bonnet, The Development of Multi-axis Real-time Subrstructure Testing, Oxford: University of Oxford, 2006.

[28] G. Ellis, Control System Design Guide - A Practical Guide, San Diego, California, USA: Elsevier Academic Press, 1990.

[29] ASTM, Standard Test Method for Tensile Properties of Polymer Matrix Composite Materials, West Conshohocken, Pennsylvania, United States of America: ASTM International, 2011.

[30] ASTM, Standard Test Method for Shear Properties of Composite Materialsby the V-Notched Beam Method, West Conshohocken, Pennsylvania, United States of America: ASTM International, 2014.

[31] F. C. A/S, Konstruktionshåndbog, Kolding, Denmark: Fiberline Composites A/S, 2003.

[32] National Instruments, "National Instruments, NI 9263," National Instruments, 1 December 2015. [Online]. Available: http://sine.ni.com/nips/cds/view/p/lang/da/nid/208806. [Accessed 1 December 2015].

[33] National Instruments, "National Instruments, NI 9205," National Instruments, 1 December 2015. [Online]. Available: http://sine.ni.com/nips/cds/view/p/lang/da/nid/208800. [Accessed 1 December 2015].

[34] S. Consortium, Volume 1: Syntax and Style, USA: SCPI Consortium, 1999.

[35] GOM, "PONTOS Live streaming with SCPI protocol," GOM, 7 August 2015. [Online]. Available: https://support.gom.com/display/KNOWLEDGE/PONTOS+Live+streaming+with+SCPI+protocol. [Accessed 7 August 2015].

[36] Brüel & Kjær, Vibration Meter Type 2511, Brüel & Kjær, 1978.

[37] S. Andersen, "Reduction Method for Kinematic Nonlinear Real-time Simulation," *Journal for Numerical Methods in Engineering (in review).*

[38] J. Waldbjørn, J. Høgh and S. Andersen, "Multi-Rate Hybrid Simulation with Multi-axial Control," *To be submitted.*

[39] M. Nakashima og N. Masaoka, »Real time on-line test for MDOF systems,« *Earthquake Engineering and Structural Dynamics,* årg. 28, nr. 4, pp. 393-420, 1999.

[40] J. P. Waldbjoern, S. Andersem, J. H. Hoegh, J. W. Schmidt, C. Berggreen and H. Stang, "Single-component Multi-rate Real Time Hybrid Simulation pilot test on a composite structure," *To be published.*

[41] NI, »http://www.ni.com/pdf/manuals/375874b.pdf,« National Instruments, - 6 2014. [Online]. [Senest hentet eller vist den 21 11 2014].

[42] A. Maghareh, J. P. Waldbjoern, S. J. Dyke and A. Prakash, "Adaptive multi-rate interface: development and experimental verification of an interface for multi-rate real-time hybrid simulation," *Earthquake Engineering and Structural Dynamics,* Accepted for publication (2015).

[43] J. P. Waldbjoern, A. Maghareh, G. Ou, S. J. Dyke and H. Stang, "Multi-rate Real Time Hybrid Simulation operated on a flexible LabVIEW real-time platform," *Smart Structures and Systems,* Submitted for peer review (2015).

[44] J. P. Waldbjørn, S. Andersen, J. H. Høgh, J. Wittrup-Schmidt, C. Berggreen and H. Stang, "Single-component Multi-rate Real Time Hybrid Simulation pilot test on a composite structure," *To be submitted,* 2016.

[45] GOM, PONTOS Live V8 Manual, Braunschweig, Germany: GOM, 2015.

[46] P.-S. B. Shing and T. Manivannan, “On the Accuracy of an Implicit Algorithm for Pseudodynamic Tests,” *Earthquake Engineering and Structural Dynamics,* vol. 19, pp. 631-651, 1990.

[47] A. Bonelli and O. S. Bursi, “Generalized-alpha methods for seismic structural testing,” *Earthquake Engineering and Structural Dynamics,* vol. 33, pp. 1067-1102, 2004.

[48] T. Horiuchi and M. Nakagawa, “Development of a real-time hybrid experimental system with actuator delay compensation,” in *Eleventh World Conference on Earthquake Engineering*, 1996.

[49] P. A. Bonnet, »The development of multi-axis real-time substructure testing,« University of Oxford, Oxford, United Kingdom, 2006.

DTU Mechanical Engineering
Section of Solid Mechanics
Technical University of Denmark

Nils Koppels Allé, Bld. 404
DK- 2800 Kgs. Lyngby
Denmark
Phone (+45) 4525 4250
Fax (+45) 4593 1475
www.mek.dtu.dk
ISBN: 978-87-7475-478-7

DCAMM
Danish Center for Applied Mathematics and Mechanics

Nils Koppels Allé, Bld. 404
DK-2800 Kgs. Lyngby
Denmark
Phone (+45) 4525 4250
Fax (+45) 4593 1475
www.dcamm.dk
ISSN: 0903-1685